Development of the INO-ICAL detector and its physics potential

By

Sumanta Pal
PHYS01200804031
Bhabha Atomic Research Centre, Mumbai - 400 085

A thesis submitted to the
Board of Studies in Physical Sciences

In partial fulfillment of requirements
For the Degree of
DOCTOR OF PHILOSOPHY
of
HOMI BHABHA NATIONAL INSTITUTE

December, 2014

Homi Bhabha National Institute

Recommendations of the Viva Voce Board

As members of the Viva Voce Board, we certify that we have read the dissertation prepared by Sumanta Pal entitled "Development of the INO-ICAL detector and its physics potential" and recommend that it may be accepted as fulfilling the dissertation requirement for the Degree of Doctor of philosophy.

Date:

Chairman - Prof. S. Kailas

Date:

Guide / Convener - Prof. D. Indumathi

Date:

Co-guide - Prof. N. K. Mondal

Date:

Member - Prof. V. M. Datar

Final approval and acceptance of this dissertation is contingent upon the candidate's submission of the final copies of the dissertation to HBNI.

I hereby certify that I have read this dissertation prepared under my direction and recommend that it may be accepted as fulfilling the dissertation requirement.

Date:

Place:

Guide - Prof. D. Indumathi

Co-guide - Prof. N. K. Mondal

STATEMENT BY AUTHOR

This dissertation has been submitted in partial fulfillment of requirements for an advanced degree at Homi Bhabha National Institute (HBNI) and is deposited in the Library to be made available to borrowers under rules of the HBNI.

Brief quotations from this dissertation are allowable without special permission, provided that accurate acknowledgement of source is made. Requests for permission for extended quotation from or reproduction of this manuscript in whole or in part may be granted by the Competent Authority of HBNI when in his or her judgement the proposed use of the material is in the interests of scholarship. In all other instances, however, permission must be obtained from the author.

Sumanta Pal

Date:

Place:

Declaration

I, hereby declare that the investigation presented in the thesis has been carried out by me. The work is original and has not been submitted earlier as a whole or in part for a degree/diploma at this or any other Institution/University.

Sumanta Pal

Date:

Place:

List of publications arising from the thesis

Journal

1. “Measurement of integrated flux of cosmic muons at sea level using the INO-ICAL prototype detector”, **S. Pal**, B. S. Acharya, G. Majumder, N .K. Mondal, D. Samuel and B. Satyanarayana, Journal of Cosmology and Astroparticle Physics, JCAP07, **2012** 033.
2. “Study of the directionality of cosmic muons using the INO-ICAL prototype detector”, **S. Pal**, G. Majumder, N .K. Mondal, D. Samuel and B. Satyanarayana, Nuclear Instrumentation and Methods in Physics Research Section A: Accelerators, Spectrometers, Detectors and Associated Equipment, 735, **2014**, 88–93.
3. “Preliminary results on optimisation of gas flow rate for ICAL RPCs”, **B. Satyanarayana**, **S. Pal**, M. R. Bhuyan, S. D. Kalmani, N. K. Mondal and R. R. Shinde, Nuclear Instrumentation and Methods in Physics Research Section A: Accelerators, Spectrometers, Detectors and Associated Equipment, 736, **2014**, 135–142.

Conferences

1. “Measurement of integrated flux of cosmic muons at sea level using the India-based Neutrino Observatory prototype detector”, **S. Pal**, G. Majumder, N .K. Mondal, D. Samuel and B. Satyanarayana, Proceedings of Science, PoS (RPC2012), **2012**, 021.

2. “Angular distribution of cosmic muons using INOICAL prototype detector at TIFR”, **S. Pal**, G. Majumder, N .K. Mondal, D. Samuel and B. Satyanarayana, PRAMANA - journal of physics, November, **2012**, Volume 79, Issue 5, pp 1267-1270.

3. “Velocity measurement of cosmic muons using the India-based Neutrino Observatory prototype detector”, **S. Pal**, G. Majumder, N .K. Mondal, D. Samuel and B. Satyanarayana, Nuclear Instrumentation and Methods in Physics Research Section A: Accelerators, Spectrometers, Detectors and Associated Equipment, 661, **2012**, S77.

Others

1. “Cosmic ray test of INO RPC stack”, M. Bhuyan, V. M. Datar, S. D. Kalmani, S. M. Lahamge, N. K. Mondal, P. Nagaraj, S. Pal, L. V. Reddy, A. Redij, D. Samuel, M. N. Saraf, B. Satyanarayana†, R. R. Shinde, P. Verma, Nuclear Instrumentation and Methods in Physics Research Section A: Accelerators, Spectrometers, Detectors and Associated Equipment, 661, **2012**, S68.

2. “VME-based data acquisation system for the India-based Neutrino Observatory prototype detector”, M. Bhuyan, V. B. Chandratre, S. Dasgupta, V. M. Datar, S. D. Kalmani, S. M. Lahamge, N. K. Mondal, P. Nagaraj, S. Pal, S. K. Rao, A. Redij, D. Samuel†, M. N. Saraf, B. Satyanarayana, R. R. Shinde, S. S. Upadhya, Nuclear Instrumentation and Methods in Physics Research Section A: Accelerators, Spectrometers, Detectors and Associated Equipment, 661, **2012**, S73.

To be submitted

1. “Simulation study of tau induced hadron events in the ICAL detector”, D. Indumathi and S. Pal.

Sumanta Pal

Dedicated to

My Parents

...

ACKNOWLEDGEMENTS

I express my sincere gratitude to my supervisors Prof. Naba K Mondal and Prof. D. Indumathi for their constant support and guidance throughout the course of this work. I am largely indebted to Dr. B. Satyanarayana and Prof. Gobinda Majumder not only for their immense effort during the work but also for their mental support throughout I joined as a graduate trainee in INO. I must admire the help I got from Deepak Samuel and Saikat Biswas. I am also grateful to Prof. B.S. Acharya, Prof. R.G. Pillay, Prof. V. Nanal, Prof. A. Dighe, Prof. S Raychaudhuri, and Prof. S Banerjee at TIFR, Prof. V. Datar and Prof. S. Kailas at BARC, Prof. M.V.N. Murthy and Prof. N. Sinha at IMSc, Dr. S. Chattopadhyay and Prof. Y.P. Viyogi at VECC, Prof. S. Bhattacharya, Prof. S. Mukhopadhyay and Prof. S. Saha at SINP, Prof. S. Umashankar at IITB for many useful discussions and suggestions during this work. I am thankful to all my colleagues at TIFR, Mr. S. Kalmani, Mr. N. Panyam, Mr. P. Verma, Mr. S. Joshi, specially Mr. R. Shinde, Mr. M.N. Saraf, Mr. M. Bhuyan, Ms. A. Redij, Mrs. D. Koli, Mrs. N. Srivastava, Mrs. S. Rao, Mr. Pavan Kumar, Mr. V. Asgolkar, Mr. S. Chavan, Mr. G. Ghodke and Mr. Mohamad A. Rahman and also to Ms. Nilima Mandal and Ganesh Das at VECC for their assistance in different arenas of my work. I am thankful to administration staffs at TIFR and also at IMSc. I thank my friends and colleagues Vivek, Anushree, Sudeshna, MoonMoon, Meghna, Lakshmi, Kolahal, Atreyee, Sanmay, Nilay and also Zeen, Swastik, Sudipta at IMSc for many useful discussions and support not only in academics but also outside the laboratory life. Last but not the least, I owe to my parents for their affection and moral support.

Synopsis

0.1 Proposed contents of the thesis

This thesis reports the work on the “Development of the INO-ICAL detector and its physics potential”. The thesis is proposed to comprise nine chapters. Brief history about particle and neutrino physics, and also about the particle detectors are summarised in Chapter 1. The physics potential of the Iron-CALorimeter (ICAL), proposed to be built by the India-based Neutrino Observatory (INO) collaboration, is then summarised in this chapter. The scope of the present thesis is afterwards discussed in this chapter. A prototype stack of 12 layers of glass RPCs (Resistive Plate Chamber) was built to study detector properties and also to track cosmic muons. Detector set up and relevant details about the Data Acquisition (DAQ) system is given in Chapter 2. Analysis of muon trajectories is illustrated in Chapter 3. A Monte-Carlo analysis of the data is also discussed in this chapter. A brief summary on the muon flux measurements is given in Chapter 4 and the obtained result is compared with the other data. Muon directionality study along with a Monte-Carlo analysis is illustrated in Chapter 5. As part of the physics simulation study at INO-ICAL detector, a phenomenological study is done about the tau neutrino response to the ICAL detector. In Chapter 6, atmospheric neutrino fluxes and brief summary about the neutrino oscillations are presented. Tau neutrinos are not there in the atmosphere, and only produced by the oscillation effect. Interactions of tau neutrinos to the ICAL detector produce tau leptons. This neutrino-nucleon cross sections is discussed in Chapter 7 along with the relevant tau kinematics. Number of tau events expected in the full ICAL detector for a 5 years run time is estimated and discussed in Chapter 8. A Monte-Carlo generator is developed to generate tau events in the ICAL detector with an objective to build a faster computing code considering only the major physics inputs. This method is illustrated in Chapter 9. Afterwards identification of tau events in the ICAL detector over the normal neutral current events are summarised in this chapter.

0.2 Introduction

A world wide endeavour has been initiated to study precisely various neutrino parameters. With the similar objective, India has also planned to build an underground laboratory mainly for neutrino physics experiments. A multi-institutional collaboration has been formed with the objective of creating India-based Neutrino Observatory (INO).

The proposed detector by the INO collaboration is a magnetised Iron CALorimeter (ICAL) with Resistive Plate Chambers (RPCs) as its active detector elements. The ICAL detector is tuned to detect mainly muons coming from atmospheric neutrinos. ICAL will have a good tracking, momentum and time resolutions along with the charge identification capability. With these capabilities, ICAL will look for precision measurements of neutrino oscillation parameters and determine the neutrino mass ordering. The performance of the detector as per the expectation and in parallel confident understanding of various signals in the detector through physics simulation studies play a key role in achieving the physics goal.

Successful completion of designing, building and characterising large size RPCs have been done and reported in Ref. [118]. To continue this development, detailed study of muon tracking efficiencies by RPCs, detailed study of time resolutions of the RPCs along with a scheme for time calibration for each RPC was taken up and is reported in the first part of the thesis. These calibrations are then used to study the cosmic muon flux on the Earth's surface and their directionality in the prototype RPC stack at TIFR, Mumbai. Such cosmic muons form major background to the study of atmospheric neutrinos which is the main focus of ICAL.

Atmospheric neutrinos contain only muon-type $(\nu_\mu,\ \bar{\nu}_\mu)$ and electron-type $(\nu_e,\ \bar{\nu}_e)$ neutrinos. At sufficiently long distances, oscillations of muon-type neutrinos to tau-type neutrinos $(\nu_\tau \text{ or } \bar{\nu}_\tau)$ are dominant due to the large relevant mixing angle, θ_{23}. The recent confirmation of large value of θ_{13} also enhances oscillations of electron-type neutrinos to tau-type neutrinos. Hence tau neutrinos (and anti-neutrinos) are expected to be copiously produced when atmospheric neutrinos pass through the Earth and reach the detector. These tau neutrinos $(\nu_\tau/\bar{\nu}_\tau)$ will undergo charged-current (CC) interactions, while interacting with the target material of the ICAL detector, to produce charged tau leptons ($\tau^\mp$) in the detector. These tau leptons $(\tau^\mp)$ can decay into muons ($\mu^\mp$), and thus contaminate the direct muon signal arising from direct CC interactions of muon neutrinos with the detector. Moreover, decays of taus to electrons and hadrons contaminate as well neutral current (NC) sample of atmosphere neutrinos. In the precision study of neutrino oscillation parameters, effects of any contaminated signal to the main signal can crucially alter the result. In view of that, a detailed study of tau decays to hadrons are reported in the second part of the thesis.

First, detector R&D related work is discussed in section 0.3 and then simulation study of tau induced hadrons in the ICAL detector is reported in section 0.4.

0.3 The performance of the RPC prototype stack at TIFR

0.3.1 Experimental set up

A successful R&D for the glass RPCs was carried out at TIFR. Different sizes of RPCs – 30×30 cm^2, 1×1 m^2 and 2×2 m^2, were developed and assembled in-house with the help of local infrastructure. These chambers operate in avalanche mode using a gas mixture of R134a, Isobutane and SF_6 in proportion 95.15%, 4.51% and 0.34% respectively. At present two muon telescopes – a 12 layers stack of 1×1 m^2 RPCs and a 4 layers stack of 2×2 m^2 RPCs, are working in parallel at TIFR INO laboratory. The first part of the thesis is based on the performance of the 1×1 m^2 RPCs stack.

The RPC layers in this stack are labelled serially from 0 (bottom) to 11 (top). Each RPC has two readout planes, labelled as X and Y, located on either side of it. Each plane has 32 strips with strips in the X plane orthogonal to strips in the Y plane. The width of the strips is 2.8 cm and the gap between adjacent strips is 0.2 cm. The layers are stacked on top of each other, separated by a distance of 16 cm, thus resulting in a total stack height of 176 cm. Thanks to the good mechanical accuracy and by using alignment corrections derived by muon tracks, an overall position accuracy better than 1 mm is obtained. The RPCs have tracking efficiencies at the central region of $(95 \pm 2)\%$ at an applied voltage of 9.9 kV (± 4.95 kV). The time resolution of these chambers is (1.2 ± 0.2) ns.

The strip hit information and the timing signal of cosmic muons together constitute the event data. The event data is recorded by the VME-based DAQ system on receiving a trigger signal and the noise rate data is recorded on periodic basis. The trigger for the data is usually generated by the coincidence of time signals of four layers. Muon flux analysis and directionality study of muons are done taking the 2^{nd}, 4^{th}, 7^{th} and 9^{th} layer in the trigger. Average rate of this particular trigger criterion is about 22 Hz and is mainly due to cosmic muons.

0.3.2 Muon track reconstruction

Here the trigger is formed in situ. Noise in the trigger layers may give fake trigger. So, a careful selection of the data has to be done to distinguish muon response from the noise. Here noise refers to mainly correlated electronic noise. At most three consecutive strip hits in a layer are considered as muon signal. On an average the frequency of hit multiplicities due to muons is 48%, 34% and 16% for single, double and triple occurrence respectively, with an average strip multiplicity of 1.6. Each strip count is also monitored for a fixed period of time; this gives noise/strip rate data. This noise rate data basically gives an idea about the health of the detector over a long period of time. On an average, noise rate has been observed to be 50 Hz. A strip has been marked noisy if its rate is more than 100 Hz. These noisy strips are neglected for any analysis. Event tracks due to any soft particles (pion/electron) are limited to at most two or three layers and those tracks are neglected in this analysis. A linear fit is performed to these selected tracks separately for X and Y-view. Residuals (R = hit−fit) are calculated and if $\mid \Delta R \mid$ is more than one strip pitch, then that hit is neglected and another fit is made for the same event with remaining hits. But in order to align all detector positions and to have better estimate of all tracking efficiencies, this fitting process is repeated iteratively where residuals are corrected and updated in each iteration. As muon trigger is in situ here, layers in between bottom and top trigger layers have less statistics at their edges due to solid angular coverage. To avoid this systematic effect, separate trigger criterion is considered. Layers 0, 1, 3 and 4 are included in the trigger definition to estimate tracking efficiencies for layers 6 to 11. Similarly, layers 7, 8, 10 and 11 are included in the trigger definition to estimate tracking efficiencies for layers 0 to 5. After this particular choice, different layers show inefficiencies at different points which are purely related to the particular detector (Figure 3.10) and these inefficiencies are taken into account in the analysis of data. The fit parameters of the last iteration are considered for the analysis on the basis of good reduced χ^2. Position resolutions (σ_{pos}) equal to 0.193, 0.194 and 0.293 (in strip units) are considered respectively for single, double and triple hit multiplicities in the χ^2 definition. Tracks to be used in the analysis were required to have hits in both X and Y views and at least two degrees of freedom (ndf = N$-2 > 2$, N being the number of layers used in the fit). We also require a good fit by asking χ^2/ndf< 2 in both views. These selected events are used to study the muon flux on the Earth's surface.

0.3.3 Monte-Carlo simulation of the muon tracks

Muon data are also verified through a Monte-Carlo simulation including all observed systematics from the data. First the impact point on the 9th layer, the trigger layer, (x_9, y_9) are generated using a uniform distribution. The direction of the track is then fixed by the simulated zenith angle (θ_s) and azimuthal angle (ϕ_s) and the hit points for intermediate layers are obtained. The θ_s angle is generated uniformly over the solid angle and ϕ_s angle uniformly over the $0-2\pi$ range. Hits are then digitised and a strip number is assigned from 0 to 31. A further level of smearing to these hit positions is done to simulate the strip multiplicity effect. In a real scenario, up to three consecutive strip hits are considered as a muon signal from the RPC. Averaging of the strip number for multiplicity greater than one creates uncertainty in the actual hit information. This effect is generated here using the measured multiplicity distributions of detector layers. Finally a hit in a layer is accepted according to the 2-D efficiency map obtained from the data. These accepted hits in various layers are then fitted to a straight line in the same way like the experimental data, as discussed before and the angular distribution for θ_s is obtained. This study is important to understand the detector differential aperture or the solid angular acceptance considering all the observed systematics.

0.3.4 Muon flux measurement

The general distribution of the measured muon flux is of the form $I(\theta) = I_0 \cos^n \theta$ (cm^{-2}s^{-1}sr^{-1}), where I_0 is defined as the vertical muon flux and

$I(\theta)$, in general, is the flux at an angle θ. The observed data can be parametrised by the following equation:

$$\int_{\theta}^{\theta+d\theta} N_{obs}(\theta)\, d\theta = \int_{\theta}^{\theta+d\theta} I_0 \cos^n \theta\, \omega(\theta)\, d\theta \tag{0.3.1}$$

where, N_{obs} is the observed number of events per second in a θ bin and $\omega(\theta)$ is the solid angular acceptance or differential aperture (cm^{2}sr) of the prototype stack. In absence of $I(\theta)$ term, eq. 0.3.1 simply gives the differential aperture of the detector which is basically the θ_s distribution obtained from the Monte-Carlo simulation under the proper normalisation. The experimentally observed θ distribution of events and the $\omega(\theta_s)$ distribution for the detector solid angular acceptance are used to estimate statistically the best fit value for I_0 and n using the χ^2 minimisation process. The χ^2 is defined as,

$$\chi^2 = \sum_{\theta=0}^{\theta_{max}} \frac{(N_{obs}(\theta) - I_0 \cos^n \theta\, \omega(\theta))^2}{N_{obs}(\theta)} \tag{0.3.2}$$

The best fit value of n (shown by eq. 0.3.3 in our case) gives the actual shape for the cosmic muon angular distribution.

$$n = 2.150 \pm 0.011 \tag{0.3.3}$$

To determine the I_0, the θ_s has to be regenerated following the shape of the observed muon flux distribution ($\frac{dN}{d\theta_s} \propto \cos^{2.15}\theta_s$). After proper normalisation due to the inefficiency of RPCs, total time of data recording and solid angular acceptance criteria, it turns out that

$$I_0 = (6.217 \pm 0.005) \times 10^{-3} \quad \mathrm{cm^{-2}s^{-1}sr^{-1}}. \tag{0.3.4}$$

The obtained muon flux distribution and the fitted result is shown in Figure 3.19.

The muon flux has been measured by various groups [127–136] over the last decade. The present result is compared with Refs. [127, 129, 131]. The geomagnetic cut off rigidity, P_c, for the present site is slightly higher (∼(14 −27)%) than in Refs. [127] and [131]. If only the P_c is considered then muon flux may appear to be little smaller than the other two places. The lower momentum cut off is similar for all four places. The present result shows ∼(14– 15)% less muon flux in the vertical direction than mentioned in Refs. [127] and [131]. The lower momentum cut off varies rapidly for low energy particles. For the present detector set-up lower momentum cut off is also checked for most inclined particles and they do not differ significantly from the vertical direction.

0.3.5 Measurement of the time delay contribution of individual RPCs

The flow of signals from the RPCs to the electronic modules in the VME crate is shown in Figure 2.2. Pre-amplifiers are required as RPCs are operated in avalanche mode. Analog signals are then converted to logic signals and processed further by Analog Front End (AFE) and Digital Front End (DFE) boards. The Control and Data Router (CDR) routes the control and data signals (Event Data/Noise Rate Data) while the Trigger and Timing Router (TTR) routes timing signals to the back-end VME based DAQ system. While noise rates are recorded by the VME-Scalar, a multi-hit TDC is used to record the arrival timing of the signal with respect to trigger signal. Each stage of the electronic circuitry introduces its own delay which should be corrected in order to obtain the actual signal time. The first stage delay can be easily measured by knowing the muon hit position on the strip; whereas, a systematic effort is required to measure delays from stages 2 to 6. For preliminary studies, the calibrations were done using a pulse generator wherein a signal is simultaneously sent to two AFEs of two different layers, among which one is the reference and the other layer is to be calibrated. With this method the time delay of stages 3 to 6 is measured while the delays of the readout strips and pre-amplifiers are not taken into account. But, using this method to calibrate the entire detector is cumbersome and time consuming. The results obtained using this method nonetheless give an idea of the order of magnitude of the delays.

In view of the shortcomings seen in the method using the pulse generator, an alternative method is adopted using muon tracks as a source for timing calibration. The total time delay has been divided into two parts; the first comes from stage 1 (Figure 2.2), which is due to the time delay in the RPC strips and the other part includes the time delays due to all electronics from stages 2 to 6. The raw TDC timing is first corrected for the time delay due to RPC strips and then used to determine the time delays from the stages 2 to 6 using this formula:

$$t_i = \delta + \frac{1}{c} l_i \tag{0.3.5}$$

where, t_i is the relative time of i^{th} layer with respect to the lowest layer with a valid hit and l_i is the corresponding cosmic muon track length. Layers having a single strip hit are considered in time delay measurements to avoid uncertainty in timing due to time ORing among all the strips in a layer. To avoid a bias in the determination of the time delays, the calibrating layer is excluded from the fitting and its time residual (Δt), is obtained. Like muon track fitting, time residuals are also corrected and updated in each iteration and the results from the last iteration is considered for the analysis. No appreciable change is observed in the mean and RMS of the time residual distributions after 4–5 iterations. The strip wise residual distributions are later fitted with a Gaussian distribution and the mean value is considered as the time delay for a corresponding strip of a layer. RMS values of these distributions are later on used as time resolutions for every strip instead of having a fixed time resolution for all layers. Any noisy channel[1] is neglected in this time delay calculation as well as for the directionality study. The observed time offsets of individual strips are corrected to the muon timings to study muons directionality.

0.3.6 The measurement of directionality

Selected events after the above-mentioned cosmic muon track fit (section 0.3.2) are used for the directionality study. Moreover, a strip hit multiplicity of at most 2 consecutive strips per layer are considered in this analysis in order to accumulate sufficient statistics. Due to ORing of time signals in a layer, the earliest strip signal defines the timing. For

---

[1] strip rate either greater than 100 Hz or RMS of Δt distribution more than 2 ns.

this reason, the strip having smaller time offset is chosen for the strip time offset correction in case of double hit multiplicity. By doing so we implicitly assume that the true timing for both strips is the same. Following this procedure, three consecutive strip hits could also be considered but this was chosen not to be appropriate since the timing uncertainty would have increased. Arrival times of muon tracks in each layer after the correction for the known delays are linearly fitted. X and Y-view time data are fitted separately. After time fitting, events are selected having at least two degrees of freedom ($\mathrm{ndf}_t = \mathrm{N_t} - 2 > 2$, N_t being the number of layers used in the time fit) and by asking $\chi_t^2/\mathrm{ndf}_t < 2$. An overlay plot of the time slope multiplied by $(-c)$ is shown in Figure 5.5 with different quality criteria on N_t. As the minimum acceptable N_t is increased we observe a decrease in the RMS as reported in Table 5.1. In this study, only the X-view timing data is shown and later on compared with a MC analysis. Y-view timing data is not simulated assuming its behaviour is the same as that of the X-view. The present study though performed at the Earth's surface is actually needed at the underground to monitor the muon background.

0.3.7 Monte-Carlo simulation of timing data

Muon tracks are first simulated as discussed in section 0.3.3. Accepted events after track fit are used for time analysis. Timing for layers are generated assuming propagation with the speed of light and assigning the zero of time when the track crosses the lowest layer with valid hit for the directionality measurement. Time residual in different layers are expected to be uncorrelated, but in real data a correlation of residuals among different layers is observed. To take care of this correlation we introduce a (12×12) covariance matrix of all layers. This covariance matrix is used to smear the muon timing in all layers. If any strip (X or Y-view) is rejected in track fit that particular layer timing is neglected for further analysis. The different strip multiplicity criterion in the directionality study (maximum two consecutive strip hits instead of three are allowed) introduces an extra inefficiency. So, in addition to efficiency in position a 2-D time efficiency map is also used to select a particular strip for timing measurement. Finally, timing of selected simulated events are fitted with a straight line and the slope of the time fit multiplied by $(-c)$ is obtained. The distribution of the number of selected layers used in the time slope fit and the reduced χ^2 distribution for time fitting are well reproduced in MC in comparison to the data. There is good agreement between the time slope distributions of the data and MC (Figure 5.10) though tails in the data are a little larger than in the MC. A comparison of the results between data and MC with statistical errors is shown in Table 5.1 which reflects a reasonable agreement between data and MC. The mis-identification of muon direction (MisId) in MC is marginally lower than the data as tails in the time slope distribution is not reproduced well enough in the MC. However, this is the first such cosmic ray analysis with the RPC stack and the data is continually being acquired. While the MC is sufficient for background calculations at present, the results of this analysis are now being incorporated into the MC in order to further fine-tune it and improve its agreement with data.

0.4 Simulation study of tau induced hadron events in the ICAL detector

Oscillations of atmospheric neutrinos to tau-type neutrinos and its CC interactions with the iron target of the detector produce tau leptons in the detector. Decay of tau leptons to electrons or muons has 17% branching fraction, whereas its hadronic decay has 66% branching fraction. These muons or electrons contribution from tau decays are peaked at lower energy with respect to the input energy (E_τ) of the tau leptons and hence, these are indistinguishable from the main signal but their effect has to be accounted for in the oscillation analysis. In the case of τ decay to hadrons, these add to NC events in the detector. Moreover, the threshold for the tau production itself is about 3.5 GeV. These two facts cause the hadrons from taus to be shifted to the higher energy side, whereas hadrons coming from normal NC events are peaked at less than a GeV. This special feature thus allows these tau induced hadrons to be identified over the NC background in the detector, which is the prime focus in this study. First, the total number of tau events in the ICAL detector with a 5 years exposure is estimated by taking inputs from neutrino fluxes, its oscillation and neutrino-nucleon interactions. Possible experimental signature of these tau events in the ICAL detector is reported later.

0.4.1 Atmospheric neutrino flux

The atmospheric neutrino flux is taken from Ref. [137–140]. The neutrino flux at SuperK is considered so far for various physics analysis by the INO collaboration. Preliminary flux data at INO site is also available [137]; the differences are mostly in the low energy region due to latitude effects and are negligible for tau analysis. Beyond 3 GeV there is no appreciable change between two fluxes. The input consists of ν_μ, ν_e, $\bar{\nu}_\mu$ and $\bar{\nu}_e$ spectra distributed over E_ν, $\cos\theta$, and ϕ, where θ is the zenith angle, ϕ is the azimuthal angle and E_ν is the energy of the incoming neutrino. The energy range for E_ν is from 0.1 GeV to 10 TeV as given in the Honda flux [137]. In this particular study, we have included contributions from E_ν in the range of 3 GeV to 100 GeV (considering energy threshold for the tau production), where flux is falling at the rate of $E_\nu^{-2.7}$. The neutrino fluxes are symmetric about $\cos\theta$ for $E_\nu > 3.2$ GeV between the up- and down-directions where $\cos\theta = -1$ refers to the up-going neutrinos.

0.4.2 Neutrino Oscillations

A detailed discussion on neutrino oscillation probability and its sensitivity to neutrino oscillation parameters for a detector with charge identification capability has been presented in Ref. [145]. To be brief, 3-flavour neutrino oscillation model is considered here with current best fit oscillation parameters [146] (Table 6.1). The matter density profile of the Earth is considered as given by the Preliminary Reference Earth Model (PREM) [144]. The entire numerical calculation for the oscillation is performed by evolving the flavour eigenstates through Earth's matter. The matter density jumps at inner-outer core and core-mantle transitions and this affects oscillation probability as well.

0.4.3 Neutrino-nucleon cross sections for CC processes

The CC interactions of tau-type neutrinos with the detector target are given by eq. 0.4.1.

$$\begin{aligned} \nu_\tau \ + \ n \rightarrow \tau^- \ + \ p, \\ \bar{\nu}_\tau \ + \ p \rightarrow \tau^+ \ + \ n\,. \end{aligned} \tag{0.4.1}$$

Since the energies of interest are from a few GeV to 100 GeV, the CC interactions includes quasi-elastic (QE), resonance (Res) and deep inelastic (DIS) processes. In the resonance case, only Δ resonance production has been considered. We consider here double differential cross-sections for tau production which is written in the form,

$$\begin{aligned} \frac{d\sigma}{dE_\tau d\cos\theta_\tau} = & \frac{G_F^2\kappa^2}{2\pi}\frac{p_\tau}{m_N}\Bigg[\left(2W_1 + \frac{m_\tau^2}{m_N^2}W_4\right)(E_\tau - p_\tau\cos\theta_\tau) + W_2(E_\tau + p_\tau\cos\theta_\tau) \\ & \pm\frac{W_3}{m_N}\left(E_\nu E_\tau + p_\tau^2 - (E_\nu + E_\tau)p_\tau\cos\theta_\tau\right) - \frac{m_\tau^2}{m_N}W_5\Bigg], \end{aligned} \tag{0.4.2}$$

where G_F is the Fermi constant, $\kappa = m_W^2/(Q^2 + m_W^2)$ is the propagator factor with the W-boson mass (m_W), p_τ is the magnitude of the 3-momentum of the charged lepton and the W_i are structure functions corresponding to the general decomposition of the hadronic tensor for QE, Res and DIS processes. The detailed expressions for W_i are taken from Ref. [156] where specific structure functions are listed for QE, Res and DIS leading order processes. We define 4-momenta in the laboratory frame for the process, $\nu_\tau(k) + N(p) \rightarrow \tau^-(k') + X(p')$, as k for incoming neutrino, p for target nucleon, k' for outgoing τ and p' for the net hadrons. We also define some Lorentz invariant variables

$$\begin{aligned} Q^2 &= -q^2\,, \quad q^\mu = k^\mu - k'^\mu, \\ W_X^2 &= (p+q)^2. \end{aligned} \tag{0.4.3}$$

Q^2 is the magnitude of the momentum transfer and W_X is the hadronic invariant mass. The separation between Res and DIS is arbitrary and determined by a cut, chosen to be $W_X \geqslant 1.4$ GeV. The resonance region is chosen as $(m_N + m_\pi) < W_X < 1.4$ where, m_π is the pion mass. For tau interactions we use the CTEQ6 LO set of parton distribution functions (leading order in the α_S) through the LHAPDF (version 5.8.7) interface.

The tau production is very much in the forward direction with respect to the incoming neutrinos and available phase space is also restricted by the kinematics. The cross sections are computed in the frame where incident neutrino direction defines the z-axis and then the results are boosted into the lab frame. The integrated cross-sections is dominated by the DIS process and contribution from anti-neutrinos to the total cross-sections is almost half compared to the neutrinos.

0.4.4 Distribution of τ events

The expected number of tau-leptons in the ICAL detector (50 kton) in 5 years exposure are obtained by integrating[2] eq. 8.0.5. Total 117 τ^- and 45 τ^+ are estimated in the upward-going direction $(-1 \leqslant \cos\theta \leqslant 0)$, whereas in the downward-going direction, oscillation effect is almost absent and so there are no tau events. The distribution of tau-lepton events, as obtained for the ICAL, is given in Table 8.3.

$$\begin{aligned} N_\tau = N_T \times T \times \int_{E_\nu,\,\cos\theta_\nu,\,\phi_\nu} & dE_\nu\, d\cos\theta_\nu\, d\phi_\nu \\ & \left(\frac{d\Phi_{\nu_\mu}}{dE_{\nu_\mu} d\cos\theta_{\nu_\mu}\, d\phi_{\nu_\mu}} P_{\mu\tau} + \frac{d\Phi_{\nu_e}}{dE_{\nu_e} d\cos\theta_{\nu_e}\, d\phi_{\nu_e}} P_{e\tau} \right) \\ & \times \int_{E_\tau^{min}}^{E_\tau^{max}} dE_\tau \int_{\cos\theta_{\tau\nu},\,\phi_{\tau\nu}} d\cos\theta_{\tau\nu}\, d\phi_{\tau\nu} \frac{d\sigma_{\nu\tau}}{dE_\tau\, d\cos\theta_{\tau\nu}\, d\phi_{\tau\nu}} \end{aligned} \tag{0.4.4}$$

---

[2] kVegas Monte-Carlo multidimensional integrator is used through the ROOT interface.

where, Φ is the neutrino flux, $P_{\alpha\tau}$ is the oscillation probability from flavour $\alpha\,(e,\mu)$ to τ, N_T is the total number of target nuclei (50 kton iron) and T is the exposure time (5 years).

0.4.5 Possible experimental signatures of tau events in the ICAL detector

Direct detection of tau-leptons in the ICAL detector is not possible due to thick iron absorbers. Lifetime of tau-leptons is about 0.3 ps in its rest frame and hence, it decays very fast to other lighter leptons ($e\,\mathrm{or}\,\mu$) or hadrons. The hadrons produced in tau production and decay, which is expected to be identifiable over the NC hadrons background, is an indirect signature of tau events in this kind of a detector. Relevant discussion on tau decays, necessary normalisation between the present cross-sections and cross-sections from the neutrino generator, NUANCE, and final simulated results are presented in the following sections.

0.4.6 Tau decays

In the leptonic decay of taus the the most probable energy of these leptons is peaked at the lower region of energy with respect to the input tau energy (E_τ), so these leptons cannot be identified separately from direct muons coming from ν_μ CC interactions with the iron target. But their contribution as a background has to be accounted for in the oscillation analysis. This is beyond the scope of the present study. Instead, we focus on indirect tau observation through modification of the NC rate through its decay into hadrons. Now, $d\Gamma_{\tau\rightarrow\sum h}/dE_h$ for tau decays to hadrons are not trivial to calculate from kinematics as there are many branching modes. TAUOLA package through NUANCE interface is used to get branching ratio for tau decay to hadrons. Fixed energy ν_τs are considered to be interacted with iron target to produce taus. Now, all type of decay modes are obtained where we choose only those decays where in the final state, no lepton (i.e., $e\,\mathrm{or}\,\mu$) is present. And doing so, all possible decay modes of tau to hadrons are separated. In these decays ($\tau \rightarrow \nu_\tau \sum h$), hadrons carry major fraction of tau energy compared to the final state ν_τ. An example plot is shown in Figure 8.4, where initially 16 GeV ν_τ was chosen which gives τ and then their decay to hadrons are selected to plot tau energy (E_τ), output ν_τ energy and net energy of hadrons. This figure clearly shows mean energy of hadrons is almost half of the initial decaying tau energy. As direct tau is not available to start with in TAUOLA, different set of energies for ν_τ are chosen with a large sample. Taus are selected with energies in 1 GeV bins around 4, 5, 6, 7, 8, 9 and 10 GeV. Energy of hadrons (E_h) are calculated as $E_h = E_\tau - E_{\nu_\tau}$. Scaling behaviour clearly indicates that the distribution is independent of E_τ within statistical fluctuations and only depends on the ratio E_h/E_τ.

0.4.7 Normalisation due to cross-sections

Our code so far does not include the NC cross sections; hence NC events from NUANCE are considered in this study. Apart from QE and DIS, more number of processes are included in the resonance scattering inside NUANCE, whereas only the Δ resonance is considered in the present analysis. This change in the cross-sections will not make much difference as the main contribution arises from DIS events. Still, an overall normalisation is adopted to scale the total number of events. Using same cross-section code, total number of $\mu^\pm$ are estimated (as in the case for taus). Afterwards, CC events due to ν_μ (and anti-particle) interaction with the iron target which gives μ^- (and anti-particle) are looked for. With respect to these total number of muons, an overall normalisation is obtained as NUANCE/present code of about 1.16. So, total number of hadron events from the NC event sample from NUANCE are then scaled while comparing with the hadron events arising from tau interactions in our calculation.

0.4.8 Tau event generation through Monte-Carlo method

A Monte-Carlo based event generator is used to generate the kinematics of each of the tau events. This kinematics reflects the $(E_\nu, cos\theta, \phi)$ dependence of the neutrino fluxes and the $(E_\nu, E_\tau, cos\theta_\tau, \phi_\tau)$ dependence of the neutrino cross sections. The code is very fast compared to the NUANCE generator since only the kinematics of the leptons is generated, not that of the hadrons.

0.4.9 Comparison of hadron events: tau induced hadrons and NC background

The NC process for neutrino interactions is $\nu_l + N \rightarrow \nu_l + X$, where $l : e, \mu, \tau$, N is the nucleon and X is the hadrons in the final state. In this kind of a process, hits due to hadrons and from recoiled nucleons cannot be distinguished in the detector and together is defined as net hadrons hits. The net hadron energy is thus formally defined within the Monte Carlo code as $E_h^{NC} = E_\nu^{input} - E_\nu^{final}$. In case of tau induced hadrons, there are two sources of hadrons. One source is, $\nu_\tau + N \rightarrow \tau^- + X$, where $E_{h1} = E_\nu - E_\tau$. Another source is when tau decays to hadrons, $\tau^- \rightarrow \nu_\tau + \sum h$, where $E_{h2} = E_\tau - E_\nu$ or vector addition of all momenta of hadrons in the final state. Total of E_{h1} and E_{h2} is defined as total hadron energy (E_h) in tau events. In this study, all the particle production is strongly forward boosted. Tau leptons produced from neutrinos are very much in the forward direction (within 5° with respect to the incident neutrino) and in this process the angle between incident neutrino with the net hadron momentum vector is also peaked around 5°.The angle between tau-leptons and the net momentum vector of decayed hadrons is also peaked around 3°.So, events are very much in the forward directions with respect to the initial neutrino direction; in other words, the up-going tau neutrinos give rise to visible signals in the detector that also correspond to "up-going" events. In the case of NC events, the up-going and down-coming samples are separated. In each case, an angle cut near horizontal direction (5° in either direction from horizon) is applied to filter out those events which may be identified with wrong direction due to large angle scattering. Tau induced hadrons events, as obtained, are plotted with hadron events from NC event sample in the same hadron energy bin in Figure 9.3.

The significance of the tau contribution can be determined through a χ^2 analysis. When the "data" consisting of NC (up and down) and tau induced signal together are fitted to NC alone, the $\Delta\chi^2$ obtained is 59.6 so the indirect observation of tau through this channel is at more than 7σ confidence level. Hence our simulations indicate that there is an excellent possibility to detect τ events from oscillations of atmospheric neutrinos in the ICAL detector by studying the modifications of the NC signals. A more detailed analysis is required in order to obtain constraints on the neutrino oscillation parameters themselves from this channel. This is a future possible direction of study.

0.5 Summary and future outlook

Analysis of cosmic ray muon data from the RPC prototype detector stack provides understanding of detector tracking efficiencies and position resolutions. This study is now carried out regularly to monitor the detector performance towards better understanding of muon flux monitoring over long period. It is proposed to stagger the RPCs in the prototype stack to confirm that the observed RPC inefficiencies are not due to solid angular acceptance issues. Simulation studies of the gas flow inside the RPCs are underway to confirm that the gas flow is uniform over the entire active volume of the RPC. Results of these studies will also be fed back into the Monte Carlo code and will be fine tuned.

Time resolution of the RPCs are studied in this analysis. The observed value is well within the requirements of the ICAL detector. Measurement of time delays of the RPC signal paths has been done and the method established can be used for the main ICAL detector as well. The background muon rates in the underground are very low compared to those at the surface. The planned readout electronics for ICAL detector is different from that being used with the RPC prototype detector stack and in principle, time calibration can be performed at the surface for each RPC detector of the ICAL. Directionality study of cosmic ray muons will be useful in the main ICAL detector to monitor the underground muon background. This is because muons are expected to reach the detector from other side of the earth, as high energy muons can penetrate only few km of rock overburden to reach the detector. A negligible fraction of muons may be observed in the upward going direction which are mainly produced by some neutrino induced processes.

Simulations study of tau events in the ICAL detector provides promising results indicating that indirect observation of tau events through its hadronic decay channel is possible at more than 7σ significance over the neutral current background. In fact, proper inclusion of the tau-induced hadron events is very important for studying other exotic possibilities such as the presence of sterile neutrinos, which also affects the NC signal. The question of whether this channel is sufficiently sensitive to help determine the oscillation parameters themselves through the tau contribution is still an open one and is currently being pursued. In fact, many more extensions and refinements of this study are possible and will be part of future work in this direction.

List of Figures

List of Tables

Abbreviation Notation and Nomenclature

INO	India-based Neutrino Observatory
ICAL	Iron Calorimeter
RPC	Resistive Plate Chamber
KGF	Kolar Gold Fields
CERN	European Organization for Nuclear Research (Geneva)
LHC	Large Hadron Collider
e^-	Electron
e^+	Positron
μ	Muon
p	Proton
n	Neutron
π	Pion
$W^\pm$	Vector boson
ν_e	Electron neutrino
ν_μ	Muon neutrino
ν_τ	Tau neutrino
$\overline{\nu}_e$	Electron anti-neutrino
$\overline{\nu}_\mu$	Muon anti-neutrino
ν_1, ν_2, ν_3	Neutrino mass eigenstates
$\theta_{12}, \theta_{13}, \theta_{23}$	Neutrino mixing angles
δ_{ij}^2	Neutrino mass squared differences
δ_{atm}	Mass squared difference measured by atmospheric neutrino experiment
δ_{sol}	Mass squared difference measured by solar neutrino experiment
L	Distance travelled by the neutrino
E	Energy of the neutrino
CC	Charged-Current (interaction)
CP	Charge conjugation and Parity (symmetry)
CPT	Charge conjugation, Parity and Time reversal (symmetry)
GZK	Greisen-Zatsepin-Kuzmin (limit)
GWth	Giga Watt thermal
eV	Electron Volt
α	Townsend coefficient
β	Attachment coefficient
FWHM	Full Width at Half Maximum
HV	High Voltage
PVC	Poly Vinyl Chloride
ABS	Acrylonitrile Butadiene Styrene
DAQ	Data Acquisition
NIM	Nuclear Instrumentation Module
CAMAC	Computer Automated Measurement and Control
VME	Versa Module Europa
TTL	Transistor Transistor Logic
ECL	Emitter Coupled Logic

Part I

Detector R&D

1 Introduction

1.1 A summary of neutrino experiments over the decade : from its proposal to the present date

The neutrino is one of the most pervasive forms of matter in the universe, yet it is also one of the most elusive. It is the most abundant particles in the universe after photon, the quanta of light.

Charles Drummond Ellis (along with James Chadwick and colleagues) established clearly during 1920 – 1927 that the beta decay spectrum is really continuous, ending all controversies. In late 1930 (4^{th} December, 1930 a physics conference at Tubingen), Wolfgang Pauli endeavoured to save the time-honoured law of energy conservation by proposing, what he himself considered a “desperate remedy”, that a new subatomic particle which shares the available energy with the electron in the nuclear β decay [1, 2]. To produce the observed β decay energy spectrum of the electron, this new particle “neutrino”, could have a mass no larger than that of the electron, it had to have no electric charge and it had to be a fermion like electrons.

In June 1931, Pauli reported his idea about neutrino for the first time at a meeting of the American Physical Society in Pasadena. Initially, Pauli named it as "neutron". J. Chadwick then discovered neutron in 1932 as we know today [3]. E. Fermi renamed the Pauli's particle as "neutrino" and formulated a theoretical model in 1934 [4, 5] to explain continuous β decay spectrum, now known as Fermi theory, in analogy with quantum electrodynamics (QED). The Fermi theory was then extended by G. Gamow and E. Teller in 1936 [6] to incorporate the observed change of one unit of the nuclear spin in some β decays, but still parity was conserved. While people were looking for the exact coupling in the weak interactions, its horizon was further extended by the discovery of the muon, μ, in 1937, by Street and Stevenson [7] and, Neddermeyer and Anderson [8]. B. Pontecorvo in 1947 proposed the universality of the Fermi interactions of electrons and muons after the observation of muon decay [9]. This is thought of as the origin of the concept now known as "generation or family". H. Bethe and R. Peierls predicted the strength of the weak interactions and claimed in 1934 that neutrino might never be observed [10]. Urged, in particular by B. Pontecorvo in the early 1950s, two physicists at the Los Alamos National Laboratory in New Mexico, Clyde Cowan and Fred Reines, searched for a way to measure inverse β decay, in which an anti-neutrino can produce a positron. The name of their project was "Project Poltergeist". They used reactor anti-neutrinos, 10 ton of equipment, including 1400 litres of liquid scintillators. They detected neutrino signal electronically first time in the history of mankind. In the summer of 1956, "Poltergeist" triumphantly recorded gamma ray bursts separated by 5.5 μs and on 14th June, Cowan and Reines sent Pauli a telegram to say that the neutrino had finally been found [11–13]. K^+ decay into two different modes with opposite parity, known as $\theta - \tau$ puzzle was giving hints about the parity violation in the weak interactions. T. D. Lee and C. N. Yang who first noted in 1956 [14] that evidence for parity conservation in weak interactions was lacking, not just in K decays but in all observed weak interactions in the past. Parity violation was first observed in the β decay of polarised ^{60}Co, known as Wu's experiment [15] and then subsequently in $\pi^+ \rightarrow \mu^+ + \nu_\mu$ and $\mu^+ \rightarrow e^+ + \nu_e + \bar{\nu}_\mu$ decays. The $V - A$ form of the weak Lagrangian was then formulated in 1958 by Feynman and Gell-Mann [16], Sudarshan and Marshak [17] and Sakurai [18]. The two component theory of a massless neutrino was proposed by Landau [19], Lee and Yang [20] and A. Salam [21]. In this theory, neutrinos are left-handed and anti-neutrinos are right-handed, leading automatically to the $V - A$ couplings. In 1958, Goldhaber, Grodzins and Sunyar [22] measured the left handedness or helicity of a neutrino which is also in agreement with the two-component theory of a massless neutrino. Lepton number was introduced in 1953 by Konopinski and Mahmoud [23] to explain certain missing decay modes. R. Davis's attempts to observe $\bar{\nu}_e + ^{37}Cl \rightarrow ^{37}Ar + e^-$ turned out to produce only some limits on the cross-section for the process, because the process violates the lepton number. This effort, however, led by Davis to the history-making Homestake solar neutrino experiment when he replaced $\bar{\nu}_e$ by ν_e from the Sun. While people were looking for many interactions to confirm lepton number conservation, Pontecorvo suggested [24], if it is shown that ν_μ produced in $\pi^+ \rightarrow \mu^+ + \nu_\mu$ can not induce e^-, then ν_μ and ν_e are indeed different particles. Later on, L. M. Lederman, M. Schwartz, J. Steinberger et al., [25] succeeded in 1962 at BNL to discover ν_μ, and this experiment is marked as the first serious accelerator neutrino experiment. Today's Standard Model (SM), which is actually the Glashow-Weinberg-Salam model, was formulated in 1967 [26–28]. This model predicted the existence of weak neutral currents and the Z boson. The Higgs mechanism, which was postulated in 1964 by P. W. Higgs [29], F. Englert and R. Brout [30], and G. S. Guralnik, C. R. Hagen and T. W. B. Kibble [31], allows the original massless gauge bosons that appear in the local gauge group model to acquire longitudinal degrees of freedom, finally making them massive as demanded in Nature. The renormalizability of the model was proved by G. 't Hooft and M. J. G. Veltman in 1971 [32]. The success of the SM was affirmed in 1973 by the discovery of neutral-current neutrino interactions in the Gargamelle experiment at CERN (1973) [33] and was subsequently confirmed at Fermilab [34]. The charm quark was discovered in 1974 in the form of the J/ψ particle $(c\bar{c})$ at BNL (J) [35] and SLAC (ψ) [36]. Subsequent discovery of $W^{\pm}$ [37] and Z [38] at CERN firmly established the SM as the model for leptonic, hadronic, weak and electromagnetic (electroweak) interactions. Charm quark discovery also proved the GIM mechanism [39]. The third lepton, τ, was discovered by M. Perl and colleagues at SLAC in Stanford, California, in 1975 [40]. After several years, analysis of tau decay modes leads to the conclusion that tau is accompanied by its own neutrino nu-tau (ν_τ) which is neither ν_e nor ν_μ. The DONUT collaboration [41] working at Fermilab announced in 2000 that tau particle were observed produced by tau neutrinos, making the first direct observation of the tau neutrino. The b and t quarks were discovered at Fermilab, respectively, in 1977 [42] and 1995 [43], completing all the building blocks of the SM with three generations. The Higgs particle is also recently discovered in LHC by the CMS and ATLAS collaboration [44, 45]. The number of generations was fixed at three in 1989 by the impressive measurements by LEP experiments at CERN of the invisible width of the Z boson [46]. Discovery of the CP symmetry violation in K^0-decay by Christenson et al. [47], in 1964 was accommodated in the SM through the mixing of three generations quarks by M. Kobayashi and T. Masakawa [48] in 1973, extending the theory of two-generation mixing developed by N. Cabibbo [49] in 1963.

No experiments that have been performed so far have detected conclusive deviations from the SM, except neutrino oscillation experiments, which have shown that neutrinos have tiny masses and they mix to each other. Now, the SM neither allow neutrino mass nor their mixing. In that sense, the SM is an effective theory of the yet unknown theory beyond the SM. Thus, the neutrino is playing the role of a messenger of the new physics beyond the SM.

The concept of neutrino oscillations was first proposed in 1957 by Pontecorvo [50], motivated by the $K^0 \leftrightarrows \bar{K}^0$ oscillation phenomena [51] (1955) in which the strangeness quantum number is oscillating. The possible oscillations that he could find at that time were $\nu \leftrightarrows \bar{\nu}$ for Majorana neutrinos. More realistic idea of oscillations came later in 1967 by Maki, Masami, Nakagawa and Sakata [52] assuming ν_e and ν_μ are mixed states of two mass eigenstates. Later on, this idea was broadened by Gribov and Pontecorvo in 1969 [53]. The theory of neutrino oscillations was finally developed in 1975–76 by Eliezer and Swift [54], Fritzsch and Minkowski [55], Bilenky and Pontecorvo [56, 57]. Designs for a new generation neutrino detectors were discussed at Hawaii workshop in 1976, subsequently leading to IMB, HPW and Kamioka detectors. The IMB, the first massive underground nucleon decay search instrument and neutrino detector [58] was built in $2000'$ deep Morton Salt mine near Cleveland, Ohio. The Kamioka experiment was built in a zinc mine in Japan. The "atmospheric neutrino anomaly" was observed by IMB and Kamiokande in 1985 [58]. Kamiokande group made first directional counting observation of solar neutrinos and confirms deficit in 1986. In 1987, the Kamiokande and IMB experiments detected burst of neutrinos from Supernova 1987A [58], heralding the birth of neutrino astronomy, and setting many limits on neutrino properties, such as mass.

The atmospheric neutrinos have provided us with the first model independent indication of oscillations of ν_μs through the Super-Kamiokande experiment [59] in 1998. In 2000, SuperK announced that the oscillating partner to the muon neutrino is not a sterile neutrino, but the tau neutrino [60]. Soudan 2 [61–64] (April 1989 to June 2001) and MACRO [65–68] experiments (1995 – 2001) provide precise information on the values of the atmospheric neutrino oscillation parameters, which are in good agreement with the independent results of the first accelerator long-baseline K2K [69–72] experiment (2001 – 2005).

Solar neutrino problem was first observed in Homestake experiment [73] and then confirmed by the observations of the Kamiokande, GALLEX/GNO (in Russia), SAGE (in Italy) in 1991-2, Super-Kamiokande and SNO experiments in 2001-2. In particular, the results of the SNO experiment [74] have been instrumental in solving the solar neutrino puzzle in 2002. The reactor long-baseline KamLAND experiment [75, 76]

(2002) has also confirmed the values of the oscillation parameters obtained from a global analysis of the data of all solar neutrino experiments.

First observation of ν_τ appearance in OPERA experiment [77] at Gran Sasso was in 2010. T2K [78] and MINOS [79] experiment have seen the appearance of electron neutrinos in a muon neutrino beam in 2011. The results of the atmospheric, solar, KamLAND and K2K neutrino experiments are nicely explained by neutrino oscillations in the framework of the simplest model of three-neutrino mixing, in which the three flavour neutrinos ν_e, ν_μ, ν_τ are unitary linear combinations of three massive neutrinos ν_1, ν_2, ν_3 with masses m_1, m_2, m_3. Daya-Bay [80], RENO [81] and Double Chooz [82] recently in 2012 measured one of the neutrino parameters, the mixing angle θ_{13} by more than 5σ confidence level. Till now, we have knowledge about mass square difference, various mixing angles etc., with lots of open questions as well.

1.2 Neutrino oscillation global picture

An up-to-date global analysis of solar, atmospheric, reactor and accelerator neutrino data in the framework of three-neutrino oscillations are presented in [146]. Neutrino oscillations are briefly discussed in Chapter 6. The fundamental neutrino parameters are the mixing angles θ_{ij}, CP-phase δ, and the mass-squared differences $\delta_{ij} \equiv m_i^2 - m_j^2$. Given the observed hierarchy between the solar and atmospheric mass-squared splittings there are two possible non-equivalent orderings for the mass eigenvalues, which are conventionally chosen as

$$\delta_{21} \ll (\delta_{32} \simeq \delta_{31} > 0) \;\; \text{Normal ordering}, \tag{1.2.1}$$

$$\delta_{21} \ll -(\delta_{31} \simeq \delta_{32} < 0) \;\; \text{Inverted ordering}\,, \tag{1.2.2}$$

and schematically shown in Figure 1.1.

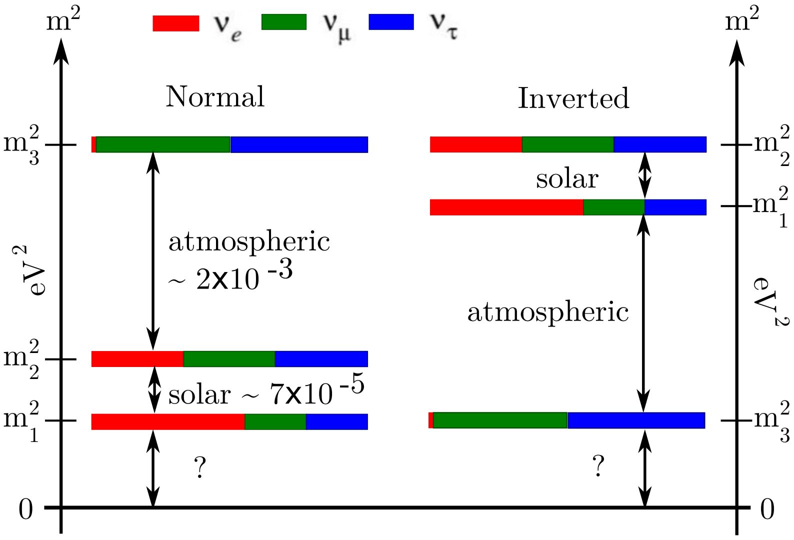

Figure 1.1. Neutrino mass hierarchy schematic diagram.

In this convention the angles θ_{ij} can be taken without loss of generality to lie in the first quadrant, $\theta_{ij} \in [0, \pi/2]$, and the CP-phase $\delta_{\text{CP}} \in [0, 2\pi]$. δ_{21}, $|\delta_{31}|$, θ_{12} and θ_{23} are relatively well determined in this context, whereas an upper bound was derived for the mixing angle θ_{13} till 2012 and barely nothing is known on the CP phase δ_{CP} and on the sign of δ_{31}. This situation is changed considerably with the data from the reactor experiments Daya Bay [80], Reno [81] and Double Chooz [82]. In addition, the increased statistics of long-baseline experiments, T2K [83] and MINOS [84], have provided a clear determination of the last unknown mixing angle θ_{13}. Authors in ref. [146] have considered the results from Super-Kamiokande atmospheric neutrino data from phases SK1–4 [85].

In the long baseline accelerator experiments (LBL), they have combined the energy distribution of ν_μ disappearance events from K2K [86] with what obtained by MINOS in both $\nu_\mu\,(\bar{\nu}_\mu)$ disappearance and $\nu_e\,(\bar{\nu}_e)$ appearance with $10.8\,(3.36) \times 10^{20}$ protons on target (pot) [84, 87], and T2K ν_e appearance and ν_μ disappearance data with phases 1–3, 3.01×10^{20} pot and phases 1–2, 1.43×10^{20} pot [88] respectively.

For oscillation signals at reactor experiments data have been considered from CHOOZ [89] (energy spectrum data) and Palo Verde [90] (total rate) together with the recent spectrum from Double Chooz with 227.9 days live time [91], and the total event rates in the near and far detectors in Daya Bay with 126 live days of data and Reno with 229 days of data-taking. Observed energy spectrum in KamLAND data sets DS-1 and DS-2 [92] with a total exposure of 3.49×10^{32} target-proton-year (2135 days).

In the analysis of solar neutrino experiments the total rates from the radiochemical experiments Chlorine [73], Gallex/GNO [93] and SAGE [94] have been considered. Data from the electron scattering (ES) Super-Kamiokande phase I (SK1) energy-zenith spectrum [95], data points from the three phases of SNO [96–98] including the results on the low energy threshold analysis of the combined SNO phases I-III [99], and the main set of the 740.7 days of Borexino data [100] as well as their high-energy spectrum from 246 live days [101].

Conclusion on oscillation parameters are listed here (ref. [146]):

1. The present global analysis disfavours $\theta_{13} = 0$ with a $\Delta\chi^2 \approx 100$. This is mostly driven by the new reactor data from Daya Bay, Reno and Double Chooz.

2. An uncertainty on θ_{13} at the level of 1σ remains due to a tension between predicted reactor neutrino fluxes and data from reactor experiments with baselines less than 100 m.

3. Non-maximal θ_{23} is favoured at the level of $\sim 2\sigma(\sim 1.5\sigma)$ for Normal (Inverted) ordering for either choice of the reactor fluxes.

4. The statistical significance of the preference of the fit for the first octant of θ_{23} is $\leqslant 1.5\sigma(\leqslant 0.9\sigma)$ for Normal (Inverted) ordering for either choice of the reactor fluxes.

5. When the normalisation of reactor fluxes is left free and data from short-baseline (less than 100 m) reactor experiments are included, the absolute best-fit occurs for Normal ordering but the statistical significance of the preference Normal versus Inverted is $\leqslant 0.7\sigma$.

6. The best fit occurs for Inverted ordering when reactor short-baseline data are not included and reactor fluxes as predicted in [102] are assumed but the statistical significance of the preference Inverted versus Normal is $\leqslant 0.75\sigma$.

7. The statistical significance of the effects associated with δ_{CP} is $\leqslant 1.5\sigma$ $(\leqslant 1.75\sigma)$ for Normal (Inverted) ordering.

The best fit values of the neutrino oscillation parameters are given in ref. [146] and a consolidated form what actually used in our analysis is given in Table 6.1 in Chapter 6.

1.3 Potentiality of the INO-ICAL detector

In this era of neutrino physics, plans have been made world-wide for new neutrino detectors, neutrino factories and long-baseline neutrino experiments. The Indian initiative in cosmic ray and neutrino physics experiments goes back several decades. The first atmospheric neutrino induced muon events were reported at the Kolar Gold Fields (KGF) underground laboratory nearly forty five years ago [103]. Another group in 1965 also observed atmospheric neutrinos in the East Rand Proprietary Gold Mine in South Africa [104]. In fact, the resurrection of Indian experimental neutrino physics programme was made possible by the experience gained in KGF experiment. A multi-institutional Neutrino Collaboration has been formed with the objective of creating India-based Neutrino Observatory (INO). The observatory will have a large underground cavern, with an all round rock cover of 1 km, to house the ICAL detector and a smaller one for experiments with more compact detectors. The access will be through a tunnel. The location of the underground cavern is at Bodi West Hill, in Pottipuram village in the Theni district of Tamilnadu, India. Relevant geographical detail about the INO cavern is given in Table 1.1. Actual land survey gives peak height above the INO cavern as 1587.6 m, whereas SOI (Survey of India) map gives

Table 1.1. Geographic details of the INO cavern.

Cavern latitude range	$9^\circ 57' 30''$ N $-$ $10^\circ 0' 0''$ N
Cavern longitude range	$77^\circ 15'$ E $-$ $77^\circ 30'$ E,
Detector origin (longitude, latitude, altitude)	$77^\circ 22' 30''$ E, $9^\circ 58' 45''$ N, 280.77 m
Axis of the cavern (w.r.t. N-S)	$23^\circ 28' 26''$
Cavern dimension (L × B × H)	132 m × 26 m × 32.5 m

as 1589 m and Google map gives as 1566 m. Floor level of the cavern is at 271.77 m above the mean sea level (a m.s.l). The origin of the ICAL detector is at 280.77 m and below the mountain at 1560 m elevation. Vertical rock cover at the origin of the detector is therefore 1279.23 m. The entire cavern is located between contours of 1579 m and 1560 m altitude of the Bodi West Hill.

Google map precision is a little different than actual topographical map given by Geological Survey of India (GSI). The error in reading the height/elevation from Google map is ±3 m. The error in fixing the exact latitude and longitude are $\pm 2''$. The digital map is considered around and up to 10 km ($\sim 1'5'' \equiv 2$ km, Table 1.1) from the peak on either sides (N-S and E-W). A contour plot of the altitude of the geographical location of the INO cavern is shown in Figure 1.2. Other technical details about the INO project can be found in ref. [105].

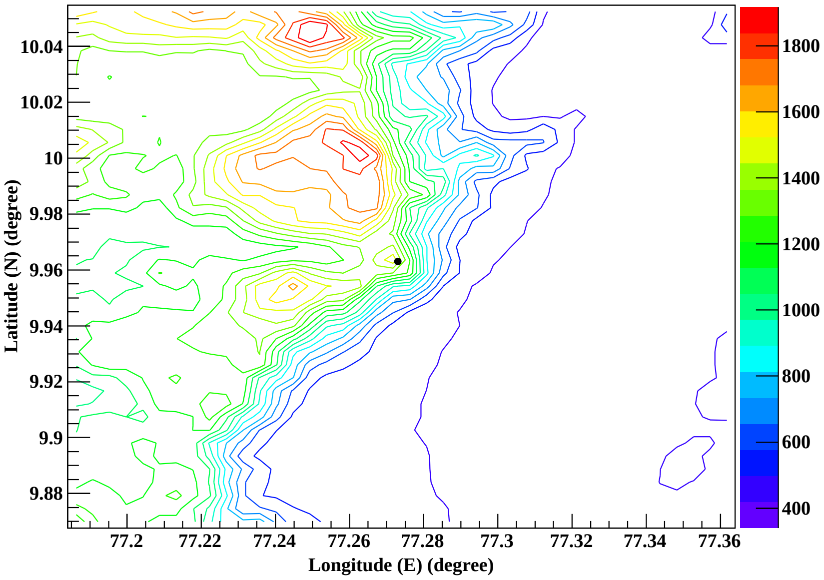

Figure 1.2. Contour plot of the hill altitude around the INO cavern. Altitude is shown in metre above the sea level. The centre of the INO cavern is also shown (black dot) in the figure.

The INO collaboration has proposed to build a massive magnetised

Iron CALorimeter (ICAL) detector inside the INO cavern. The ICAL is contemplated as both a detector for atmospheric neutrinos and as well as a future end-detector for a neutrino factory beam. In both cases, the primary detection mechanism is via detection of muons produced in charged current neutrino interactions. The detector will comprise of layers of iron sheets interleaved with the planar active detector elements, which are Resistive Plate Chambers (RPCs). The detector will be magnetised to a field of about 1.3 T, which allows for charge discrimination of muons. The atmospheric neutrino physics program possible with ICAL is substantial. It is possible to observe a clear signal of oscillation by observing one full oscillation period so that the precision of the parameters, δ_{32} and θ_{23}, can be improved to 10%. We can also use atmospheric neutrinos to probe CPT invariance which is one of the fundamental paradigms of quantum field theories, of which the Standard Model is one. Apart from their charge discrimination capability, iron calorimeters have a large range in sensitivity to L/E variations compared to water Cerenkov detectors and can substantiate the evidence of neutrino mass and oscillation already observed by Super-Kamiokande experiment, via the observation of dips and peaks in the event rate versus L/E. When used as an end-detector for a high γ Beta Beam or a neutrino factory, the ICAL-CERN distance matches the magic baseline, so that results are insensitive to the CP phase $\delta_{\rm CP}$. The major physics goal of the ICAL detector are summarised below:

- To re-confirm the occurrence of oscillation in atmospheric muon neutrinos and significantly improve measurement of the oscillation parameters, through the explicit observation of the first oscillation swing in ν_μ disappearance as a function of L/E. A broad range in both path length L and energy, E, and indeed in their ratio, L/E, possible with atmospheric neutrinos, offers the opportunity to probe a large range of δ_{32}.

- To observe matter dependent effects, using the ability of the magnetised ICAL detector to distinguish neutrino and anti-neutrino initiated processes by detecting the charge of the produced muons. Determining the sign of δ_{32} and the magnitude of θ_{13}, using the matter effect. Non-zero value of θ_{13} has tremendous implications for observing Earth matter-dependent oscillation effects as well as CP violation in the leptonic sector.
- A new way of distinguishing whether the muon neutrino deficit observed by previous experiments is due to oscillations of muon neutrinos to tau neutrinos or to sterile ones. A sterile neutrino does not have a charged lepton partner and immune to the weak interactions, unlike the other three known active neutrinos (ν_e, ν_μ, and ν_τ).
- Probing CPT violation in the neutrino sector using atmospheric neutrinos and putting bounds on them. The atmospheric neutrino data involve both the particle and the antiparticle channels and are therefore suitable for studying CPT violation. As the atmospheric neutrino experiments are probing mass squared differences and not the absolute neutrino mass, these will be the quantities which might be restricted by the data. The interest in CPT violation arises due to a recently suggested scheme which is capable of solving all neutrino anomalies without the use of a light sterile neutrino [106].

- Constraining the long range leptonic forces. These are a special class of long range forces which distinguish between leptonic flavours and have far reaching implications for the neutrino oscillations. In turn we may use them as a probe of such forces.

- To study multi-TeV cosmic ray muons through pair-meter technique. The technique [107] is used to measure the energy and frequency of electron-positron pair cascades produced by the passage of a high energy muon in dense matter. Such studies in the high energy (TeV–PeV) region can throw light on possible extensions of the Standard Model.

1.4 Detector requirements for the ICAL detector

The primary focus of ICAL at INO is to study interactions involving atmospheric muon neutrinos and anti-neutrinos. This requires the construction of a detector that is sensitive to the energy, direction and sign of the electric charge of muons, produced by charged-current (CC) interactions of neutrinos (ν_μ & $\bar{\nu}_\mu$) with the detector material. This detector (perhaps upgraded in terms of fiducial volume) will also be a suitable choice as a far-end detector of a long-base-line experiment. Based on the physics goals of the ICAL detector, the following criteria was used for selecting an appropriate design for the detector system.

- A reasonable target mass to achieve a statistically significant number of neutrino interactions in a reasonable time-frame for the confirmation of atmospheric neutrino oscillation.

- For the precise measurement of the oscillation pattern in the L/E spectrum of atmospheric muon neutrinos, the energy E and direction θ of the incoming neutrino have to be accurately measured in each event. Now, direct reconstruction of neutrino is not possible, but precise measurement of muon and hadron energy able us to reconstruct the neutrino energy. The direction of the neutrino can be estimated from the direction of muon produced and also taking care of the net hadrons direction. Therefore, the energy and angular resolution of the detector should be good enough so that L/E can be measured with an accuracy better than half of the modulation period.

- In order to estimate the distance traversed by the neutrino, it is necessary to establish the flight direction (up vs. down) of the muon produced by the neutrino with high efficiency. Different techniques like increase of curvature in a magnetic field, multiple scattering along the track or the measurement of timing in successive detector layers can be used to achieve this. Of these the time-of-flight technique is the most effective and allows excellent up-down discrimination for a detector with a time resolution (σ) of 1 ns or better.

- Identification of the electric charge of muons so as to distinguish between neutrino and anti-neutrino interactions. Charge determination is necessary to achieve most of the physics goals mentioned above.

- Compactness, ease of construction and modularity which allows the possibility of phasing.

The basic detector specification is listed in Table 1.2. A schematic of the ICAL detector is shown in Figure 1.3.

Table 1.2. Salient parameters of the ICAL detector structure.

Modules	3
Module dimension	16 m×16 m×14.5 m
Detector dimension	48 m×16 m×14.5 m
Iron layers	151
Iron Plate thickness	56 mm
RPC layers	150
Gap for RPC units	40 mm
RPC dimension	1800 mm×1910 mm×20 mm
RPC units/ layer/ module	64
RPC units/ module	9600
Total RPC units	28800
Total readout channels	3686400
Magnetic field	1.3 T
Rock overburden	> 1 km

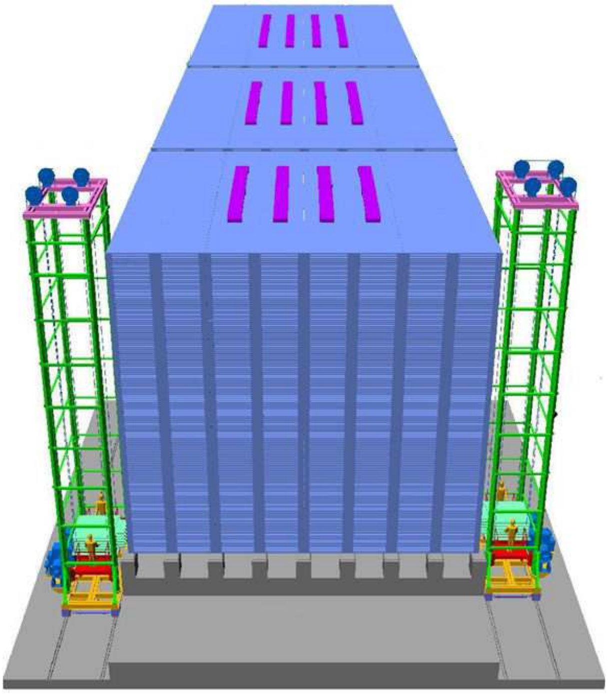

Figure 1.3. Schematic view of the proposed ICAL detector (3 modules) at INO. RPC detector handling trolleys are shown on either side. The top view of the magnet coil (purple colour) is also shown here.

1.5 Brief history of gaseous particle detectors

The discovery of X-rays and radioactivity in the 1890s can be announced the birth of particle detectors. H. Becquerels photosensitive paper, which was blackened by the radiation released by uranium salt was possibly the first documented particle detector. Rutherford and Marsden also used scintillating signals while discovered the atomic structure. During that period, visual screening of the events was performed by an experimentalist seating in front of the detector. Later on, various gaseous detectors were invented where track reconstruction of the particles can be done later. Among these the cloud chambers, the emulsion-, bubble-, spark-, and streamer chambers are notable. Basic working principle in these detectors is the ionisation of the active gaseous medium by the moving charged particles. In these detectors particle tracks are photographed and later on analysed. Discovery of Compton scattering, positron, nuclear disintegration of cosmic rays etc. happened using cloud chambers. Discovery of pions was performed using nuclear emulsion technique. Bubble chambers were used in the discovery of neutral current in the weak interactions and to study other decay products in various interactions. The technology then evolved towards the electrical methods from these optical methods. Detectors that record the ionisation produced by the charged particles in the gaseous medium became popular as they used to record the position of the track and the time of its passage. Gaseous detectors such as wire or drift chambers [108] have successfully replaced the scintillator counters, particularly requiring high position resolutions. The amount of ionisation created inside the active volume of these gaseous detectors could also be used to determine the charge and velocity of the intercepted particle. In the multiwire proportional chambers or drift chambers position resolution up to 100 μm can be achieved as the electric field is highly concentrated around the central wire - usually to dimensions of the order of the wire diameter, and and all electrons need to drift into this region before amplification and the signal generation sets in. Time resolution of wire detectors is rather poor due to fluctuations in the drift time of the primary electrons. It also depends on the spatial distribution of the primary ionisation produced by the minimum ionising particle (MIP). This introduces a time jitter, limiting the time resolution of wire based detectors to a few nanoseconds. In fact, scintillator detectors generally outperform the wire based gaseous detectors as far as time resolution is concerned [109].

Time resolution in these gaseous detectors can be improved if a strong uniform electric field is used instead of a radial field. In this case, avalanche amplification sets in instantly for all primary clusters right after the primary ionisation. The intrinsic detector time resolution is then dominated by the spatial variation of the primary interaction leading to a temporal spread, avalanche statistics. Noise induced triggering time fluctuations are thus minimised. The first gas detector taking shape in this way was the Keuffel Spark Counter, a gaseous avalanche detector with parallel plate geometry [110]. In general, spark counters are consist of two planar metal electrodes with a high voltage applied to them, filled by a gas mixture. Primary ionisation triggers avalanches and at some stage avalanche transforms to a streamer, where photons produced due to recombination process of electrons and ions contribute to the spread of free charge carriers. At some stage, chamber starts discharging when a plasma like filament formed between two electrodes. The rapidly growing anode current is transformed by a resistor into a fast voltage signal and this signal can be taken as a time flag for the arrival of the charged particle. Here, signal strength is quite high and no need any further amplification, thus electronic time jitter is avoided [111]. Time resolution comes around 1 ns compare to Geiger-Müller counters which has time resolution about 100 ns. But the chamber size for the spark counters are at the order of few cm^2; if the area is increased discharge energy in a spark becomes large enough to damage the surface of the counter. That is why switching-off circuit is required to prevent the electrode. The dead time of these chambers is also long, about 1 s, so maximum detection rate is a constraint. Moreover, it is worked with low-pressure gas and had a very short operating span [111].

To overcome these problems, a new type of spark chamber introduced resistive plate electrodes and special gas mixtures for photon absorption in 1971 [112]. The discharge in the detector causes a voltage drop between the two electrodes. The resistivity of around 10^9 Ω-cm of the electrodes limits the discharge to an area around the primary avalanche and because the high voltage drops only locally, the remaining counter area is still sensitive to charged particles. The electrodes gets recharged with a time constant that is much longer than the typical time scale of the avalanche development. It then turns out that the multiplication process is self-extinguishing when resistive electrodes are used. Moreover, if organic gases with high ultra violet absorption capability are used then charge diffusion in the gas will be prevented and the actual area of the detector which suffers from the voltage drop is localised around the primary ionisation region. The main advantage of the use of resistive electrodes is that high voltage switching off circuits are no longer necessary and consequently a higher detection rate can be achieved. The energy in the sparks is much smaller than in the case of metallic electrodes and therefore larger electrode surfaces can be used. In this development, Planar Spark Chamber (PSC) was built by Pestov. Pestov Spark Counter [113, 114] with a 0.1 mm gap achieved a time resolution of 25 ps. But this thin gap and higher electric field (500 kV/cm) demand a very good surface smoothness of the electrodes. Inside gas pressure is also high here, about 12 bar. A Parallel Plate Avalanche Chamber (PPAC) [115] is a single gap gaseous detector very similar to the Spark Counter but operate in avalanche mode. It has a good rate capability up to 10 MHz/cm^2, time resolution 100 –250 ps. But signal strength is low so need low noise high gain pre-amplifiers.

1.6 Resistive Plate Chamber (RPC)

The Resistive Plate Chamber (RPC) was introduced in 1981 by R. Santonico and R. Cardarelli [116] as a practical alternative to the remarkable localised discharge spark counters, which ultimately achieved a time resolution of 25 ps. The basic principle in the RPC is same as that of Pestovs Planar Spark Chamber. Nevertheless, drastic simplifications were introduced in its realisation; such as, absence of high pressure gas, lower requirements of mechanical precision and use of plastic materials instead of glass. The resulting detector, was found to be free from damaging discharges by construction and provided a time resolution of the order of 1 ns. Together these merits made RPCs of potential interest in a different and wider range of applications in modern experiments. In particular it has replaced plastic scintillators, whenever large detecting areas are needed in low counting rate environments.

RPC is operated with an uniform and constant electric field between the two parallel electrodes, at least one of which is made of a material with high bulk resistivity. During ionisation, produced free charge carriers trigger avalanches of electrons in the high electric field and originate a discharge. Due to the high resistivity of the electrodes, effective electric field around the discharge point suddenly dropped. Thus the discharge is prevented from propagating through the whole gas volume. Rest of the counter area still remain sensitive to the particles. Gas mixture used inside the chamber has high absorption coefficient for ultraviolet light which kills photons produced in the discharge. This prevents secondary discharges from originating at other points, mainly at cathode surface of the detector. The propagation of the growing number of electrons induces a current on external strip electrodes.

Charged particles ionises the inside gas medium of the RPC and creates electron-ion pairs. The drift velocity of electrons is much higher than ions. The drifting of the electrons produce changes in the electric field lines which actually induces signals to the metallic electrodes on the either plane of the detector. Due to the large applied electric field across the electrodes, primary electrons produce further ionisation and this multiplication mechanism results in a distribution of free charge in the gas which has the characteristic shape of an avalanche.

Recombination processes during avalanche produce photons which are basically absorbed using quenching gas and thus stopping further secondary avalanches in the detector volume.

A schematic of the RPC detector is shown in Figure 1.4. The bulk resistivity of the resistive material is about 10^{10}–10^{12} Ω-cm, separated by a few mm. The electrodes are connected to a high voltage power supply in order to create a uniform and intense electric field (about 5 kV/mm) in the gap between them. A thin layer of graphite is coated over the external surface of the electrodes to permit uniform application of the high voltage. The electrodes are kept apart by means of small polycarbonate cylindrical spacers having a diameter of about 10 mm and a bulk resistivity greater than 10^{13} Ω-cm. A gas mixture could consist of Argon, Isobutane and Freon (R134a). Argon acts as target for ionising particles while Isobutane, being an organic gas, helps to absorb the photons that result from recombination processes thus limiting the formation of secondary avalanches far from the primary ones. An electronegative gas may serve the purpose of limiting the amount of free charge in the

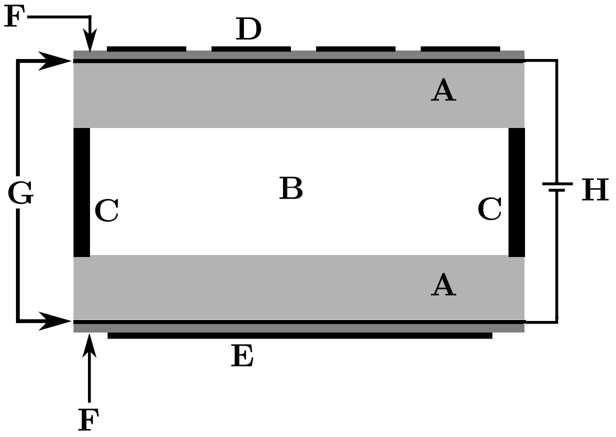

Figure 1.4. Constructional schematic of a basic RPC. A: High resistive electrode | B: Gas gap | C: Side spacers | D: Readout strips-X | E: Readout strips-Y | F: Insulator | G: Graphite coating | H: High voltage.

gas. We use mixture of R134a, Isobutane and SF_6 while operating in avalanche mode. The surface resistivity of the graphite coating is high enough to render it transparent to the electric pulses generated by the charge displacement in the gas gap. For this reason electric signals can be induced on metallic strips capacitively coupled to the gap. The strips are mounted on the external surface of the gap from which they are separated by a layer of mylar insulator. Two different sets of strips oriented in orthogonal directions may be arranged on both sides of the detector to obtain measurements in both planes. The strips behave like transmission lines with typical characteristic impedance of about 50 Ω. High resistivity of the electrodes prevents high voltage supply from providing the electric charge that would be necessary to maintain the discharge between the electrodes. Therefore the electric field drops drastically in the region of the discharge causing it to extinguish. Glass RPCs can handle counting rates of up to about 500 Hz/m^2 with a dead-time of less than 1%. Since typical bulk resistivity of bakelite is two orders of magnitude lower than that of glass, the rate capability of bakelite RPCs is proportionately higher.

The formation of the electric signal in the RPC is essentially based on the process of electron multiplication. Following the passage of an ionising particle through its gas gap, a certain number of primary electrons are created; they are grouped into clusters each of which is created by a single ionisation. The n_0 electrons of a given cluster are accelerated by the electric field and start the multiplication in the gas. This process is characterised by the parameter α (first Townsend coefficient), which represents the number of ionisation per unit length, and by β which is the attachment coefficient, i.e., the number of electrons that are captured by the gas per unit length. The parameter β becomes particularly important in the presence of electronegative gases. If x is the distance between the anode and the point where the cluster is produced then the number of electrons that reach the anode will be given by [117]:

$$n = n_0 e^{\eta x} \tag{1.6.1}$$

where, $\eta = \alpha - \beta$. The gain factor of the detector is defined as,

$$M = \frac{n}{n_0} \tag{1.6.2}$$

Operating regimes of the RPCs - avalanche or streamer, can be distinguished by the value of M. If M is greater than 10^8, then primary ionisation will give rise to streamers with high probability. On the contrary values of M much lower than 10^8 are low enough to prevent formation of additional secondary avalanches and the simple charge multiplication phenomenon occurs. In this case smaller amounts of charge are created and the detector is said to operate in avalanche mode. Transition into streamer regime by a RPC designed to operate in the avalanche mode is often a severe problem to deal with.

Y. N. Pestov suggested that a planar detector with resistive electrodes can be modelled as a set of discharge cells which to the first order can be considered independent of each other. The simple expression of the capacitance of a planar condenser leads to the result that the area of such cells is proportional to the total average charge Q that is produced in the gas gap [109]:

$$S = \frac{Qd}{\epsilon_0 V} \tag{1.6.3}$$

where, d is the gap thickness and V is the voltage applied to the electrodes. This expression explains the important role played by the parameter Q in the maximum detection rate that a RPC is capable to sustain efficiently: the smaller the value of Q, the smaller the surface of the discharge cells and therefore the higher the rate capability. The average charge produced in the gas gap for a RPC operating in the streamer mode is about 100 pC, while in the avalanche mode the value is about 1 pC. Operation in the avalanche mode requires, however sophisticated front-end electronics. Indeed the basic idea in this mode is to transfer a large fraction of the gain factor characterising the streamer regime from the gas gap to the front-end electronics. The latter must provide large amplification factors and at the same time a large bandwidth in order not to spoil the detector intrinsic time resolution.

More detailed discussion on RPCs, specially development of glass RPCs at Tata Institute of Fundamental Research (TIFR), Mumbai, is presented in ref. [118].

1.7 Scope of this thesis

Successful completion of designing, building and characterising large size glass RPCs have been done and reported in ref. [118]. During this study, a prototype stack of 1 × 1 m^2 with 12 layers was built to check RPC performance over a long period of time. This prototype stack is functioning continuously for last 6 years. It is used today as cosmic ray test stand not only to characterise new detectors but also to validate various electronic circuitry which are planned for the ICAL detector. This detector development work is further continued using this prototype stack to study in detail various operational parameters of the RPCs. Detailed study of muon tracking efficiencies by RPCs, its performance to measure muon flux on the Earth's surface, detailed study of time resolutions of the RPCs along with a scheme for time calibration for each RPC was taken up and is reported in the first part (Part I: Chapter 2 – Chapter 5) of the thesis. These calibrations are then used to study the cosmic muon flux on the Earth's surface and their directionality in the prototype RPC stack at TIFR. Such cosmic muons form major background to the study of atmospheric neutrinos which is the main focus of ICAL.

Atmospheric neutrinos contain mostly muon-type $(\nu_\mu,\ \bar{\nu}_\mu)$ and electron-type $(\nu_e,\ \bar{\nu}_e)$ neutrinos. At sufficiently long distances, oscillations of muon-type neutrinos to tau-type neutrinos $(\nu_\tau \text{ or } \bar{\nu}_\tau)$ are dominant due to the large relevant mixing angle, θ_{23}. The recent confirmation of large value of θ_{13} also enhances oscillations of electron-type neutrinos to tau-type neutrinos. Hence tau neutrinos (and anti-neutrinos) are expected to be copiously produced when atmospheric neutrinos pass through the Earth and reach the detector. These tau neutrinos $(\nu_\tau/\bar{\nu}_\tau)$ will undergo charged-current (CC) interactions, while interacting with the target material of the ICAL detector, to produce charged tau leptons $(\tau^\mp)$ in the detector. These tau leptons $(\tau^\mp)$ can decay into muons $(\mu^\mp)$, and thus contaminate the direct muon signal arising from direct CC interactions of muon neutrinos with the detector. Moreover, decays of taus to electrons and hadrons contaminate as well neutral current (NC) sample of atmosphere neutrinos. In the precision study of neutrino oscillation parameters, effects of any contaminated signal to the main signal can crucially alter the result. In view of that, a detailed study of tau decays to hadrons are reported in the second part (Part II: Chapter 6 – Chapter 9) of the thesis.

1.7.1 Part I : Detector R&D

First, the detector set up and the DAQ are discussed in Chapter 2. Analysis of muon tracks observed in the prototype stack at TIFR is presented in Chapter 3 followed by a Monte Carlo (MC) analysis and muon flux measurement. A brief summary of cosmic muon flux measurement and comparison with the present result is discussed in Chapter 4. Analysis of muon timing data and the directionality study are discussed in Chapter 5 and the directionality measurement is further reproduced using a MC analysis.

1.7.2 Part II : Physics simulation study

A brief discussion about the atmospheric neutrino flux is given in Chapter 6. Three-flavour neutrino oscillations along with necessary details are also discussed in this chapter. The neutrino-nucleon charge current cross section and necessary kinematics are discussed in Chapter 7. The estimation of number of tau events in the ICAL detector, decay of tau leptons to lighter leptons or hadrons are discussed in Chapter 8. A preliminary MC event generator for the tau events is presented in Chapter 9. Expectation of tau induced hadrons over the neutral current hadron sample is also analysed in this chapter and the phenomenological results are mentioned.

1.8 Chapter summary

First, a brief history of the particle physics along with the highlights of the neutrino experiments over the decade is discussed. Global picture of the neutrino oscillation as of today is then discussed. Potentiality of the ICAL detector to perform a precise measurement of the neutrino oscillation parameters and consequently requirements of the detector are discussed with necessary details. A brief summary of the particle detectors, mainly gaseous particle detectors and specially the Resistive Plate Chambers are discussed afterwards. Scope of the present thesis is then highlighted along with the future outlook.

2

Detector set up and the DAQ

2.1 The prototype stack

The prototype stack (as shown in Figure 2.1) used in this study consists of 12 layers of glass RPCs of 1×1 m^2 in area. The layers are labelled serially from 0 (bottom) to 11 (top). Each RPC has two readout planes, labelled as X and Y, located on either side of it. Each plane has 32 strips with strips in the X plane being orthogonal to strips in the Y plane. The width of the strips is 2.8 cm and the gap between adjacent

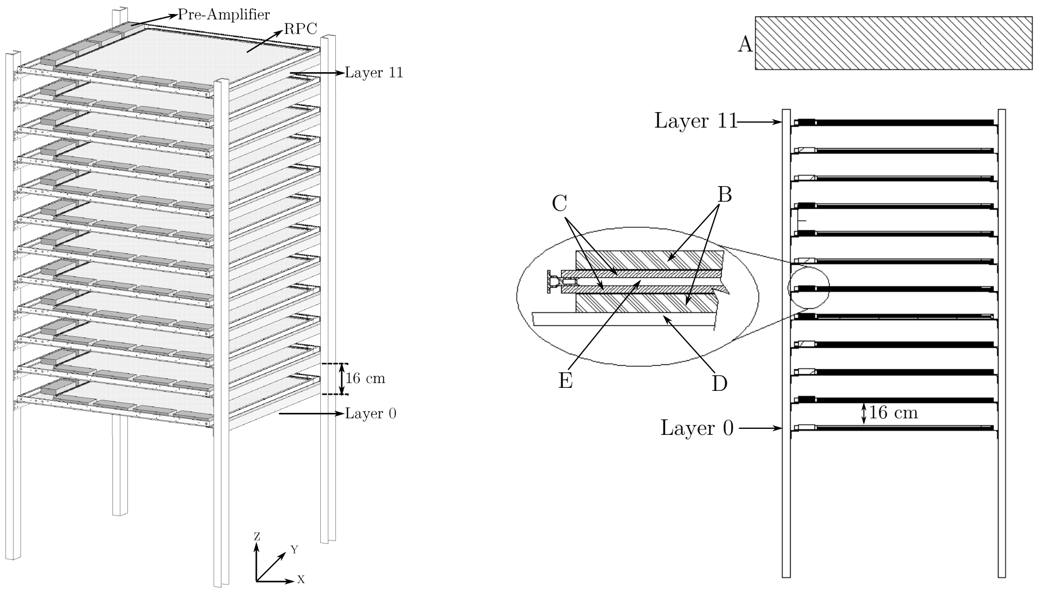

(a) 3D-view (b) 2D-view

Figure 2.1. Elevation of the prototype stack in two dimensional (2D) and three dimensional (3D) view. An RPC layer is shown with a zoomed view in 2.1b. Different materials are marked by A, B, C etc. Details are given in Table 2.1.

strips is 0.2 cm. The layers are stacked on top of each other, separated by a distance of 16 cm, thus resulting in a total stack height of 176 cm. Different materials which a muon has to traverse to generate the trigger are shown in Figure 2.1b. Thickness and densities of these materials are listed in Table 2.1. Total material thickness traversed by the vertically incident muon from the building's roof down to the second layer is about 141 g cm^{-2}. Energy loss for about 1 GeV/c muon is about 2 MeV per g cm^{-2} which makes minimum momentum cut off in the vertical direction to be about 280 MeV neglecting energy losses in the gas inside the RPC and in the air. Thanks to the good mechanical accuracy and by using alignment corrections derived by muon tracks, an overall position accuracy better than 1 mm is obtained (section 3.1.6). The RPCs are operated in avalanche mode with tracking efficiencies at the central region of (95 ± 2)% at an applied voltage of 9.9 kV (± 4.95 kV) (section 3.1.8). The time resolution of these chambers is (1.2 ± 0.2) ns (section 5.1.3). The flow of signals from the RPCs to the modules in the VME crate is shown in Figure 2.2. Brief description for each stage is given in the following sections.

Table 2.1. Material details.

Material Type	Material Name	Material Thickness (cm)	Material Density $(\mathrm{g\,cm^{-3}})$ [125]
A	Roof/Concrete	~ 45.0	2.3
B	Signal pick-up/ Polyethelene	0.5	0.94
C	Glass	0.3	2.4
D	Aluminium tray	0.5	2.699
E	RPC gas gap	0.2	$\sim 10^{-3}$

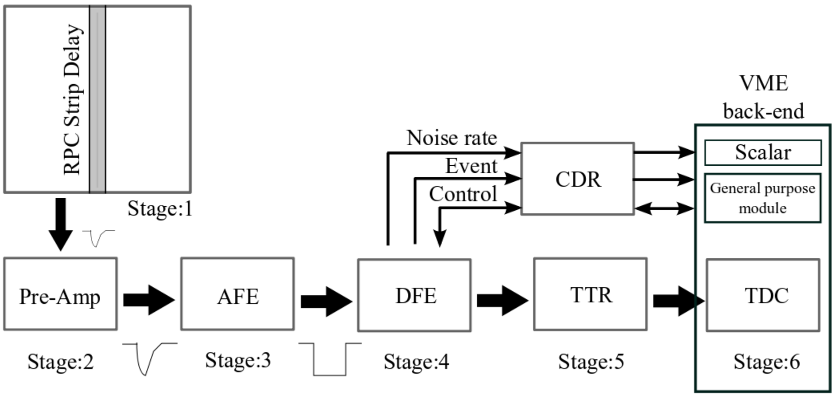

Figure 2.2. The data flow from the individual strips to the back-end VME DAQ system. The negative going pulses are only shown, whereas positive going pulses are also processed by similar electronics. The level-0 trigger signals are generated in stage 3 and the fold signals are generated in stage 4. The 1-fold trigger signal is used for timing measurements as discussed.

2.1.1 RPC

These are float glass RPCs of size 1×1 m^2. Glass thickness is 3 mm and the gap between two electrodes is 2 mm. Continuous flow of gas mixture, which is the active medium for the ionisation, is maintained using an open loop based gas recirculation system. A gas mixture of R134a, Isobutane and SF_6 in a proportion of 95.15%, 4.51% and 0.34% respectively are used to operate these RPCs in avalanche mode. High voltage (HV) region is chosen middle of the plateau region (HV vs. efficiency curve). Out of 12 layers, one layer is made of Italian glass where saturation region with respect to the detector HV is achieved at lower voltage compared to the other layers which are made of Indian Asahi float glass. Based on this consideration, the Italian RPC is maintained at 9.5 kV (± 4.75 kV) whereas Asahi RPCs are operated at 9.9 kV (± 4.95 kV). Chamber current drawn by these chambers, on an average, is $30-50$ nA. The surface resistivity of the graphite coating is maintained around 1 M$\Omega/\Box$. This particular value is chosen in such a way that the bias voltage can be applied on these coats and also to render it transparent to electric pulses generated by the charge displacement in the gas gap. Plastic honeycomb panels of 5 mm in thickness, laminated on one side by 100 μm thick aluminium sheet and other side by 50 μm thick copper sheet, are finally used for the electronic signal pick up. Readout strips of 28 mm width are realised by machining 2 mm wide gaps on the copper sheet at 30 mm pitch. Aluminium side acts as the signal reference layer/ground surface. These honeycomb panels provide a good mechanical support and its characteristic impedance is 50 Ω, which matches well with the front end electronics, i.e., the pre-amplifiers. They are placed on top and bottom such a way that copper strips face graphite coating. Mylar sheets of thickness 50 μm are inserted between copper strips and graphite coating for insulation.

2.1.2 Pre-Amplifier

In avalanche mode of operation, typical signal from RPC across a 50 Ω load is in the range 0.5 – 2.0 mV and rise time of about 1 ns. Hence, high speed and low noise pre-amplification are required before further processing by the front end electronics. Signal from each RPC strip is being extracted by terminating the far-end of the strip by a 50 Ω resistor and connecting the near-end to a 8-in-1 two-stage Hybrid Micro Circuits (HMC) based high speed high gain voltage pre-amplifiers. Two types of first stage HMCs (P1 in Figure 2.3) - one for positive polarity signals (BMC 1595) and other one for negative polarity of signals (BMC 1597) are used with a nominal gain of 10 and a negative polarity output signal. The second stage HMC (BMC 1513) (P2 in Figure 2.3) provides another stage of gain of 10 to these signals. Though the net designed gain is 100, on an average, a factor of 80 is achieved. In the range of few mV to about 40 mV of the input signal, the gain is more or less constant. Design characteristics of all HMCs are similar, such as signal handling range (100 – 200 mV), bandwidth (350 MHz), rise time (2 ns), power rails ($\pm$ 6 Volt) and power dissipation (120 – 140 mW). These pre-amplifier boards are fitted inside a galvanised iron (GI) mounting case to improve the EMI shielding as well as grounding especially at the input side of the board. The length of cables going from the pre-amplifiers to the Analog Front End (AFE) boards are equal for all channels (1.7 m). The characteristic impedance of these cables is also 50 Ω.

2.1.3 Analog Front End (AFE)

Each RPC has two dedicated AFEs per readout plane. Total 32 channels from a side of RPC are equally divided between two AFEs. The AFE is equipped with adjustable threshold (from $\pm$ 10 mV up to $\pm$ 500 mV) discriminators and ECL output signals. Practically a threshold of (-)20 mV is chosen based on the baseline noise. The discriminator used here is a ultra fast dual comparator (AD96687) (C1, C2 etc., in Figure 2.3) which accepts analog signal from pre-amplifier and gives differential ECL outputs. The negative logic signal goes to differential ECL driver (MC10101) (D1, D2 etc., in Figure 2.3) which is then passed through Digital Front End (DFE) for the monitoring purpose. The AFE also houses a primitive trigger logic where the positive logic outputs of quadruplets of channels $(0, 8, 16, 24;\ 1, 9, 17, 25;\ 2, 10, 18, 26;\ \text{etc.})$ are logically ORed (wire ORed) and then passed to a ECL monoshot (MC10198) (M1, M2 etc., in Figure 2.3) where output ECL signals are shaped to 100 ns width. These are the level-0 trigger signals and for a RPC layer we have total eight such signals called S0, S1, $\cdots$, S7. Standard ± 6 Volts power lines are used for these AFEs, whereas DFEs are running with ± 7.5 Volts. A schematic of signal processing from RPC strip to the end of AFE output is shown in Figure 2.3.

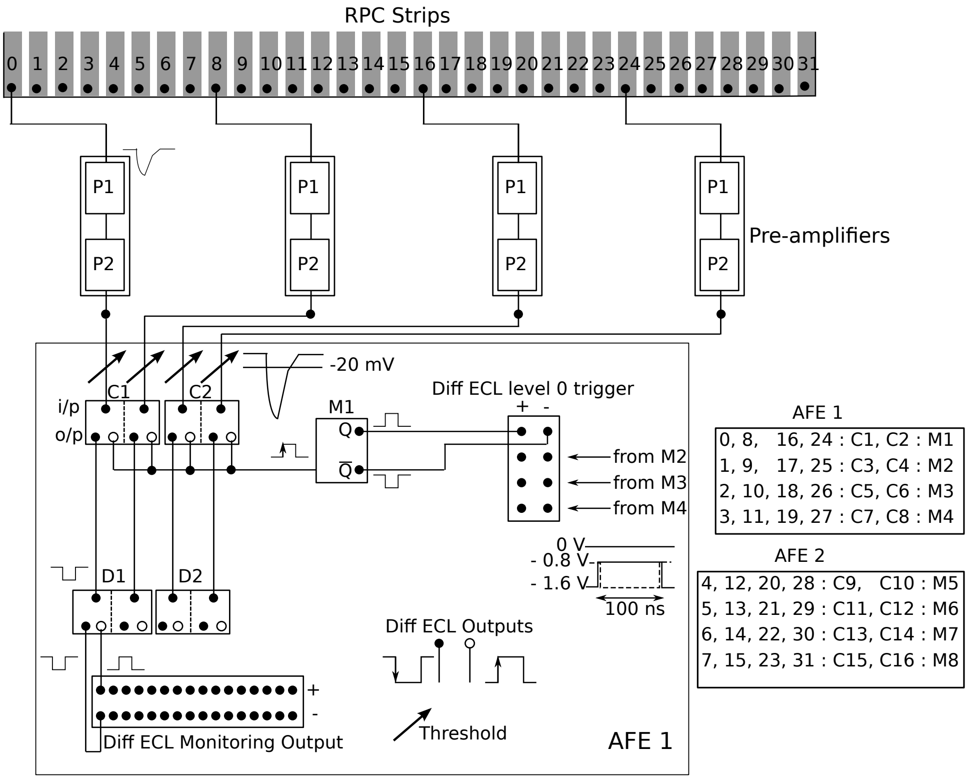

Figure 2.3. Flow of signals from RPC strips to AFE. P1 and P2 are the 1st and 2nd stages of the pre-amplifiers. The block AFE1 is one of the AFE boards. C1, C2, etc. are the comparators, D1, D2, etc., are the ECL drivers and M1, M2, etc., are the monoshots. Bunching of individual channels and their respective grouping through comparators and monoshots are also separately mentioned in the right side adjacent small boxes.

2.1.4 Digital Front End (DFE)

The DFE board is composed of four sections:

- The Decoder unit which controls data acquisition and noise monitoring, uses the hand-shake signals from the Control and Data Router (CDR).

- The Event section which handles the latching of the strip-hit information. These latched data are flushed out serially to the CDR on receipt of an appropriate signal from the Decoder unit.
- The Pre-trigger section which generates level-1 trigger signals from different combinations of S0, S1, $\cdots$, S7 signals (viz., 1-Fold, 2-Fold, 3-Fold, 4-Fold)[1]. These fold signals (LVDS output) are generated inside the CPLD 2 (1F, 2F, 3F, 4F in Figure 2.4) which are only monitored on this board. ECL signals are preferred for timing measurements as their rise times are faster compared to that of the logic signals. That is why, differential ECL level-0 signals generated in AFEs are simply ORed together to make a ECL 1-Fold signal. The timing measurement is made using the ECL 1-Fold signals separately from the X and Y planes for each RPC.
- The Noise Rate Monitoring section which latches the noise rate of the active strip or calibration signal on receipt of a clock signal from the Decoder unit and switches over to the next strip. At the end of the cycle (32nd strip), the cycle is reset and the monitoring continues from the first strip. The clocking is handled by the data acquisition (DAQ) system. Here differential ECL monitoring signals from AFEs are first translated to TTL and stretched to a width of 720 ns. This stretching is done to keep the signal line active until the trigger is validated and data is latched.

These monitoring and latching the event data are performed by the CPLD 1; inside the CPLD 1 only the multiplexing of signals are done, while the

---

[1] 1-Fold = S0 + S1 + S2 + S3 + S4 + S5 + S6 + S7, 2-Fold = S0·S1 + S1·S2 + S2·S3 + S3·S4 + S4·S5 + S5·S6 + S6·S7 and so on. Here, ‘+’ means OR and ‘·’ means AND.

actual counting is done by a scalar unit in the back-end VME DAQ system. This is a $2^6 : 1$ multiplexer (MUX), where we use only $40 : 1$, as there are 32 strip signals, 4 fold signals and 4 fixed calibrating frequencies.

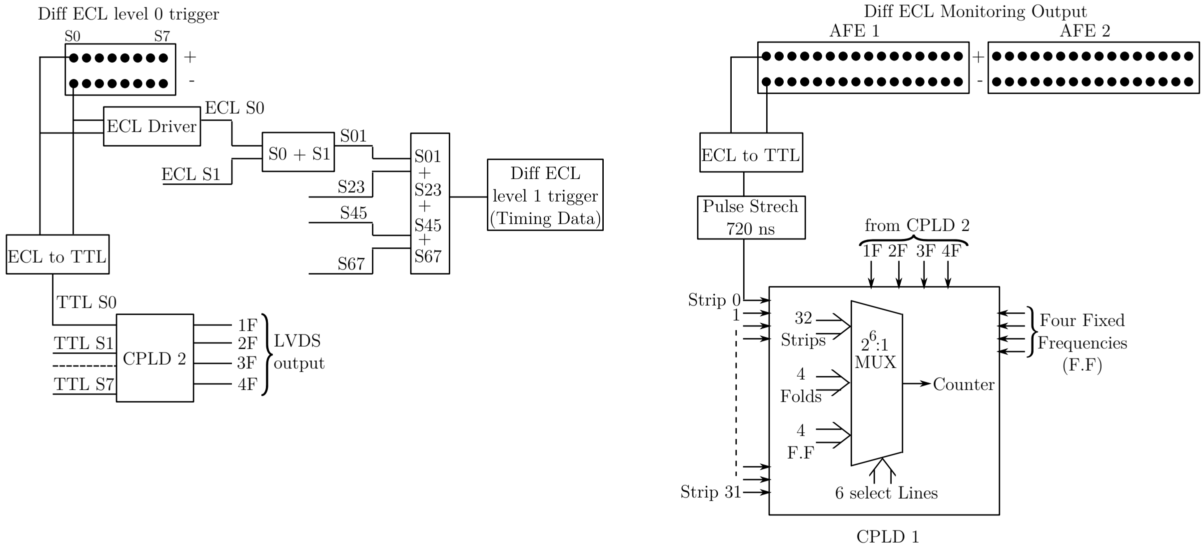

Figure 2.4. Schematic of the DFE board. Left block shows formation of 1-fold ECL signal for timing measurement and also four fold LVDS signals from the CPLD 2. Right block shows latching of noise rate and event data through the CPLD 1.

2.1.5 Control and Data Router (CDR)

CDR board accepts control signals from the INO DAQ Controller board through the address lines (A0, A1, A2 and A3) which check for board ID etc. E/$\bar{\text{M}}$ address line decides whether to latch event or monitoring data. SOX, SOY are the latched data information and CLKX, CLKY are their corresponding clock signals. Trigger address line carry the cosmic muon trigger information. MO is the monitoring signal, MCLK is the corresponding clock signal and MR is the monitoring reset signal. MR signal is reset after reading data from 32 strips, 4 fixed frequencies and 4 fold signals. In the present configuration, one CDR board can not handle data routing for 12 layers. Total 4 such CDR boards are there, one is called "Master CDR" and others are called "Slave CDR". Slave CDR boards only route monitoring signals as there are total 24 monitoring signals (MO) (total 12 layers, X and Y plane) for the entire detector stack.

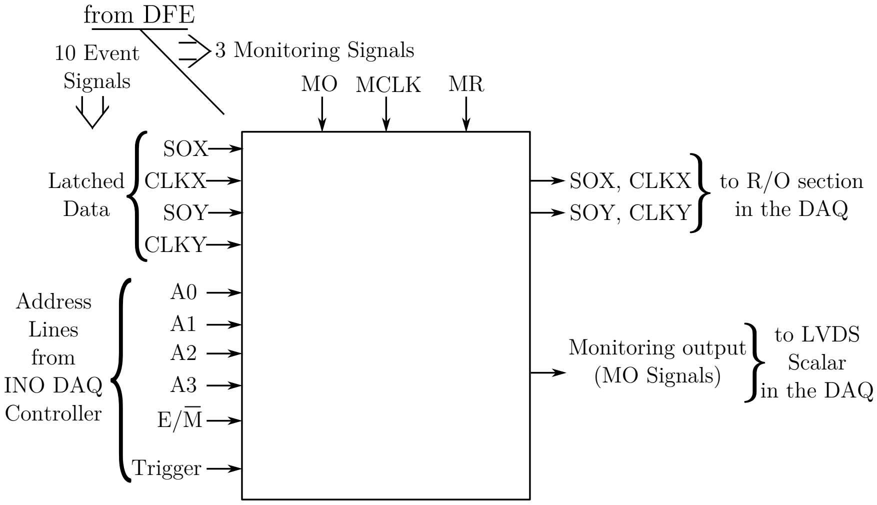

Figure 2.5. Schematic of the CDR board.

2.1.6 Time and Trigger Router (TDR)

TTR board is used for routing the time and trigger information. 4 fold signals from the DFE, i.e., 1-Fold, 2-Fold, 3-Fold, 4-Fold are inputs in this board, where 1-Fold is the ECL type and others are in the LVDS format (Figure 2.6). These signals are then translated to TTL format in the Receiver&Driver section. The conversion of these signals to TTL is required as bunching of TTL signals is easy to handle rather than differential signals. Bunching of 1-Fold signals for all layers are done and converted to ECL and LVDS formats; ECL signals are required to record the time in the TDC and LVDS signals are used in the Final Trigger Module (FTM) module. Other fold signals are also bunched together, one at a time and then translated to LVDS format. We do not need ECL format for these signals as they are only used in the FTM which accepts LVDS inputs.

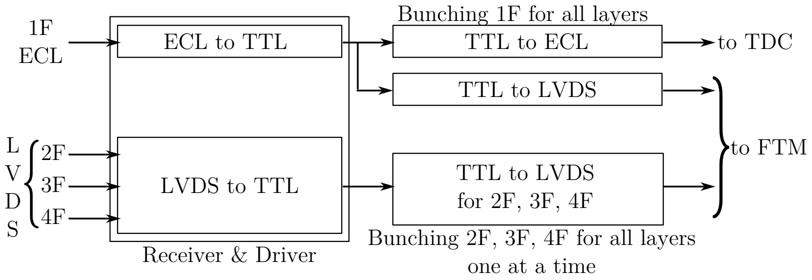

Figure 2.6. Schematic of the TTR board.

2.2 DAQ system

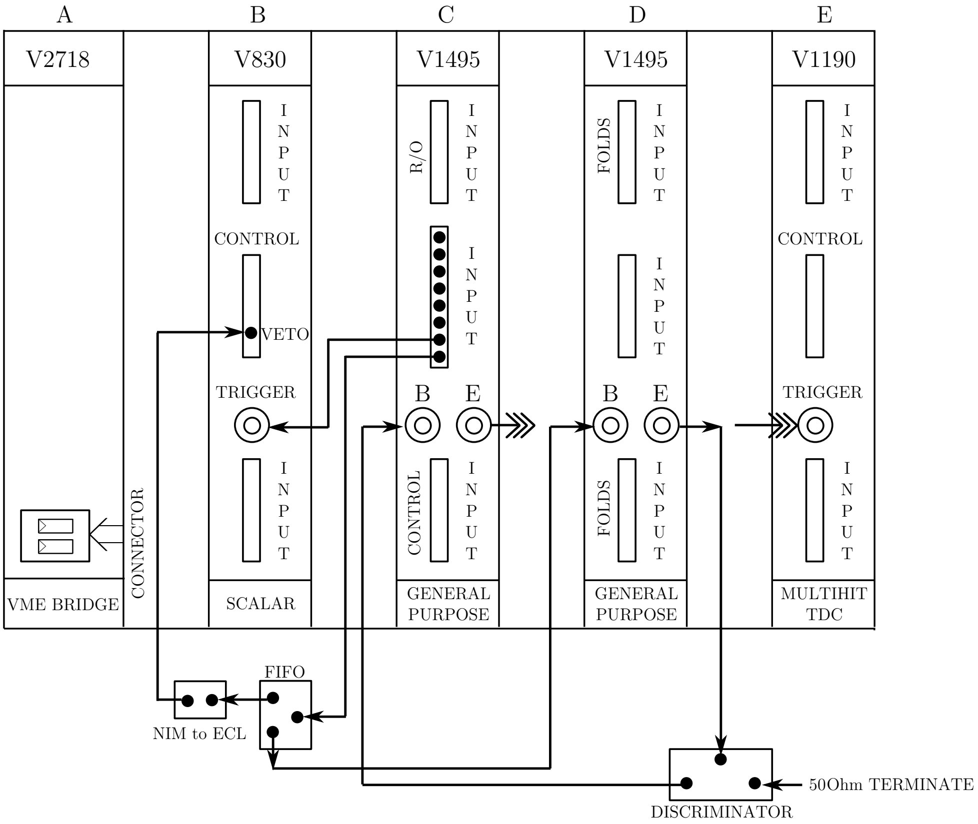

Figure 2.7. Schematic of the DAQ system. Module A: VME bridge, Module B: Scalar, Module C: General Purpose board for Read-Out (R/O) and Control, in general I/O Module, Module D: General Purpose board for Final Trigger Module (FTM), Module E: TDC. Interconnections between the modules are also shown.

Processed signals by the front-end electronic boards are transferred to the back-end DAQ system as Event or Monitoring data, which are finally recorded on the basis of valid trigger.

- The Event data, i.e., the (x, y) hit patterns in the layers due to the passage of cosmic muons, is read by an I/O Module (Customised CAEN V1495) (Module C in Figure 2.7). This I/O Module also manages the latching of the data from the appropriate DFE boards using the control lines in the CDR.

The timing data from each of these layers, from the TTR unit, is read by a multi-hit TDC (CAEN V1190) (Module E in Figure 2.7).

- The Monitoring data which contains strip noise rate, the four calibrating fixed frequencies and fold signals, are read by a 24 bit scalar (CAEN V830) (Module B in Figure 2.7) at regular intervals.

Muon flux measurement or their timing measurements are usually performed using a 4-layers coincidence, i.e., 1-Fold signals from these layers are ANDed to generate the trigger. This coincidence trigger also generates an interrupt via the TDC module, to read out the Event Data. The I/O module manages the periodic read out of noise rates and also generates an interrupt via the Scalar for the same. The event interrupt is random in nature as it is a consequence of a particle passing through the detector satisfying the coincidence condition. The noise rate interrupt is periodic as it samples each strip at a pre-defined frequency.

The DAQ back-end process has been designed to have a multi-threaded structure to support concurrent execution of various jobs in a prioritised manner thus enabling the application to offer the advantage of a full-fledged live analysis and plotting framework to the user. Although POSIX (Portable Operating System Interface) threads are widely used in C++, the QThread class offered by the Qt to implement the threads are used here. The QThread class supports the “signal and slot” mechanism making the communication between a thread and the GUI much simpler. There are four main threads that run in the background as described here:

- Interrupt Service Thread (IST),
- Event Thread,
- Noise Rate Monitoring Thread and the
- Event Plotting Thread.

The IST carries out the following jobs sequentially:

1. waits for an interrupt signal.
2. on receiving an interrupt, all interrupts are disabled via software.
3. identifies the source of interrupt (TDC/Scalar) by reading out the Interrupt Vector Register.
4. acknowledges the interrupt.
5. reads data from the relevant modules and appends them in a shared memory and triggers either the Event Thread or the Noise Rate Monitoring Thread.
6. enable interrupts.

The shared memory is a circular buffer which is allocated in the heap during the initialisation phase of the program. Two shared memories are used, one for the Event Data and another for the Noise Rate Data.

Both the Event Thread and the Noise Rate Monitor Thread are semantically similar to each other in the sense that they do same job but on different data. As soon as the IST sends a trigger (sequence 5 of IST), the latest data from the shared memory is appended to a file and the file is finally saved at an appropriate moment.

The graphical display of strip hits of various layers is helpful in cases where the detector and the electronics are being tested. The display of the particle tracks through the detector in real-time also gives a feeling of the status of the detector. This is accomplished in the Event Plotting Thread. Plotting of each and every event is not desirable and therefore, this thread is set to auto-trigger every n seconds, where n (usually 10 s) is set by the user in the GUI. This thread runs exclusively to plot the strip hit information in the layers. The thread reads the latest event, decodes them and plot on the canvas. Simultaneously, the same data are sent to a server.

As mentioned earlier, the QThread class has been used to implement all the threads. Each thread is scheduled for execution based on its priority. Qt offers several types of priorities which can be assigned to the threads by the user. The IST is assigned the maximum priority as it executes time-critical operations. The Event Thread and the Noise Rate Monitoring Thread are assigned normal priority as transfer of data from the shared memory is not a time-critical operation, provided a proper thread synchronisation mechanism is used. The plotting of events is a process that can be safely stopped or executed at a later point of time without hindering the data acquisition. Therefore, the Event Plotting Thread is assigned a low priority.

The threads run at their own time scheduled by the Operating System. However, when a file is being accessed by one thread, for example, to plot the timing distribution or the noise rate distribution, another access to the same file should be avoided. To overcome such situations, the threads are synchronised and files are protected within Inter Process Communication (IPC) objects called Mutex. Here again, the QMutex class by Qt is used to implement the mutexes. The threads check the status of the Mutex objects before writing to the file. In case the file is being accessed by the user, the thread waits until the job is completed and then proceeds with the writing.

2.2.1 Cosmic muon trigger

RPC time signals are used for trigger generation. Usually this in situ trigger is formed from 4 out of 12 layers coincidence. 1-Fold time signals (100 ns width) from each layer are used in this trigger formation. Other options, using 2-Fold or 3-Fold options are kept through the FTM module, but in this small prototype stack rate of a horizontal trigger is very low and mainly vertical trigger by using 1-Fold signals are formed. The cosmic-muon flux measurement and the directionality study of muons are done using 1-Fold signals from layer 2, 4, 7 and 9. This particular choice was made just to gain in the detector solid angular coverage. On an average trigger rate of 22 Hz has been observed in this case. Tracking efficiency measurements of RPC layers using muons were done with different set of trigger criteria to gain in the solid angular coverage. A schematic of the solid angular acceptance of the prototype stack is shown in Figure 2.8. The maximum solid angle subtended by the 2^{nd} and 9^{th} layer affects the corner regions of the layers in between and results in poor statistics. Different trigger criteria are therefore required

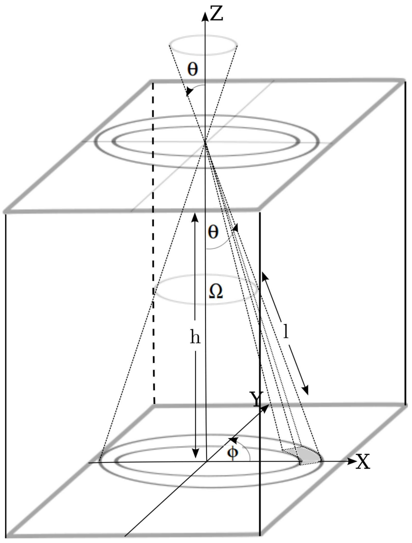

Figure 2.8. a schematic of the detector acceptance; for a fixed point in the top trigger layer solid angular acceptance in the bottom trigger layer is shown for a θ. An elemental area in the bottom layer is also marked with a shaded boundary.

to get an exact 2-D efficiency map for all layers so that the solid angle coverage is quite large and entire detector area can have good number of events. Two different trigger criteria are thus used for tracking efficiency measurements. Tracking efficiency of layers 0 to 5 are measured when trigger is formed by the layers 7, 9, 10 and 11 and for the efficiencies of layers 6 to 11, layers 0, 1, 3 and 4 are used in the trigger criterion.

2.2.2 Time measurement by TDC

Formal start-stop information is not available in the multi-hit VME-TDC. Depending on the trigger a programmable match window is opened with an extra search and reject margins (Figure 2.9). Both the trigger position and the match window have a jitter of 25 ns associated with them. Hence, no absolute time measurement can be done with respect to them. Time stamps due to muons from different layers are expected to be inside the match window for a genuine event. So, relative time stamps, i.e., time of a layer with respect to another layer, are used for any timing measurements. In general, 0^{th} layer is used as a reference. But during time offsets estimation or in the directionality study (Chapter 5, section 5.1.3), lowest selected layer based on the muon hit selection criteria is chosen as the reference layer. Different window settings of the TDC are listed in Table 2.2.

Table 2.2. Different window width for the TDC.

Match Window Width	5×25 ns
Extra Search Margin	1×25 ns
Window Offset	-6×25 ns
Reject Margin	1×25 ns
Lead Time Resolution	100 ps
Pulse Width Resolution	100 ps
Dead time between hits	5 ns
Maximum hit per event	No limit
Edge LSB	100 ps
Readout FIFO Size	16 words

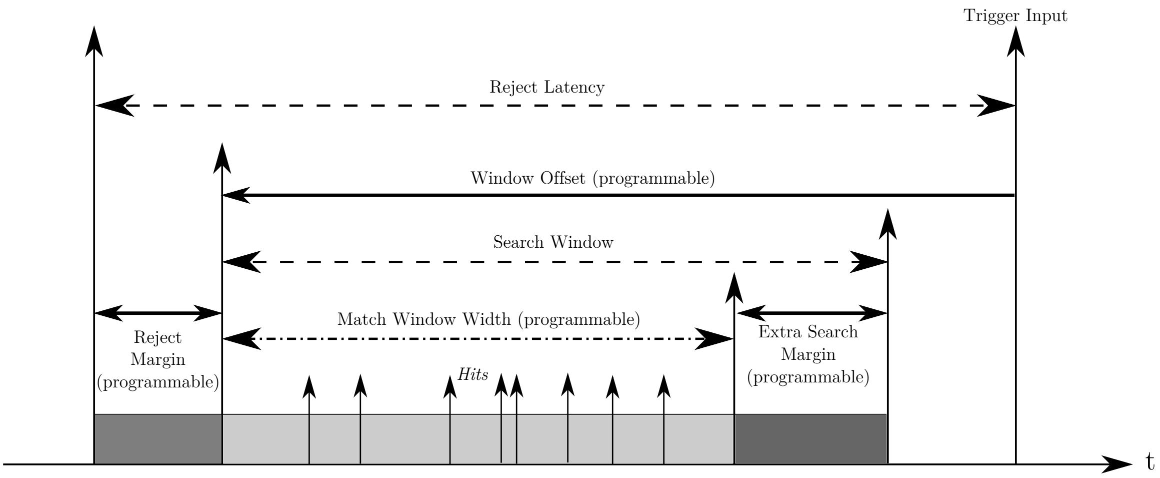

Figure 2.9. Schematic of time stamps in the multi-hit TDC.

2.3 Chapter summary

Experimental set up of the 12 layers 1×1 m^2 prototype stack, brief discussion on individual detector components and basic building blocks of the front-end electronics are discussed in this chapter. An overview of the DAQ system and its functionality are given here. Necessity for the different cosmic muon triggers and how they are formed are explained in this chapter. Brief discussion about the timing measurement by the TDC is also discussed, which also explains the relevance of the relative time measurement with respect to other layers for any timing data analysis.

3

Analysis of muon trajectory - Data and Monte-Carlo

3.1 Data

Cosmic muons leave behind its information as strip hits in the RPCs and its time of arrival. The trigger condition is in situ here as described in the section 2.2.1. Judicious selection criteria is thus necessary to choose good events over the background noise. In this chapter, selection criteria for muon hits and the track reconstruction procedure are described.

3.1.1 Strip hit profile

Cosmic muons arrive from all directions at the top of the detector stack. RPC strips are fired due to the passage of these muons. So, the strip hit distribution for a layer is expected to be uniformly distributed. In practice, a sinusoidal shape is observed as strips at the edges have less events than those at middle. This particular behaviour is due to in situ trigger condition. Usually, a top and bottom layers are present in the trigger formation and due to this geometry solid angular coverage is restricted for in between layers. The strip hit distributions for each layer is fitted using eq. 3.1.1.

$$y = p_0 + p_1 \times x + p_2 \times sin\left(\pi \frac{x}{32}\right) \tag{3.1.1}$$

where, x is the strip number and varies from 0 to 31. The linear term, $(p_1 \times x)$, was initially used due to an observed slope in frequency between the 0^{th} and the 31^{st} strip for some particular event samples. Later on, this nature is no more observed and in the present analysis this term is not being used. In the argument of the sine function, $(\frac{x}{32})$, is required which defines the sine function from 0 to π as there are 32 strips in a layer. Strip hit profile and their fitting with eq. 3.1.1 are shown in Figure 3.1. A strip is rejected if its counting rate is larger than 80% of the fitted value (y) and not being considered for further analysis.

3.1.2 Raw occupancy

The (x, y) hits are filled in a 2-D histogram for each layer to check functioning of the detector over its entire region. This includes also the noise hits. It is seen from Figure 3.2 that at some places event statistics is low which is due to inefficiency of the detector at that particular regions and/or trigger criteria. Some bands show higher counting which is due to noise hits.

3.1.3 Layer multiplicity and hit selection

The primary ionisation inside the RPC gas gap and flow of the charged particles towards their respective electrodes produce signals in the read out strips. The principle of signal induction by moving charges to the respective electrodes are relevant here to discuss. A detail discussion in this context is given in ref. [122]. A point charge q in the presence of a grounded metal plate induces a charge on the metal surface. This surface charge can be is calculated by using the Poisson equation for the potential ϕ with a point charge q at $z = z_0$, where z_0 is the distance of

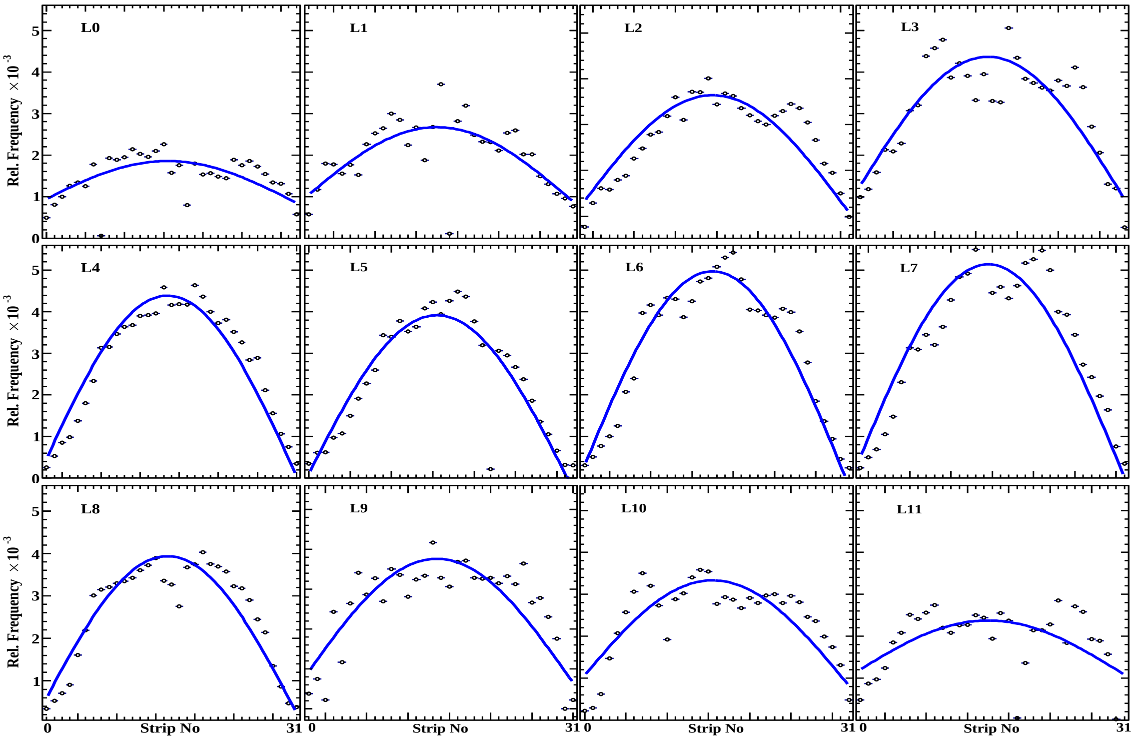

(a) X-view

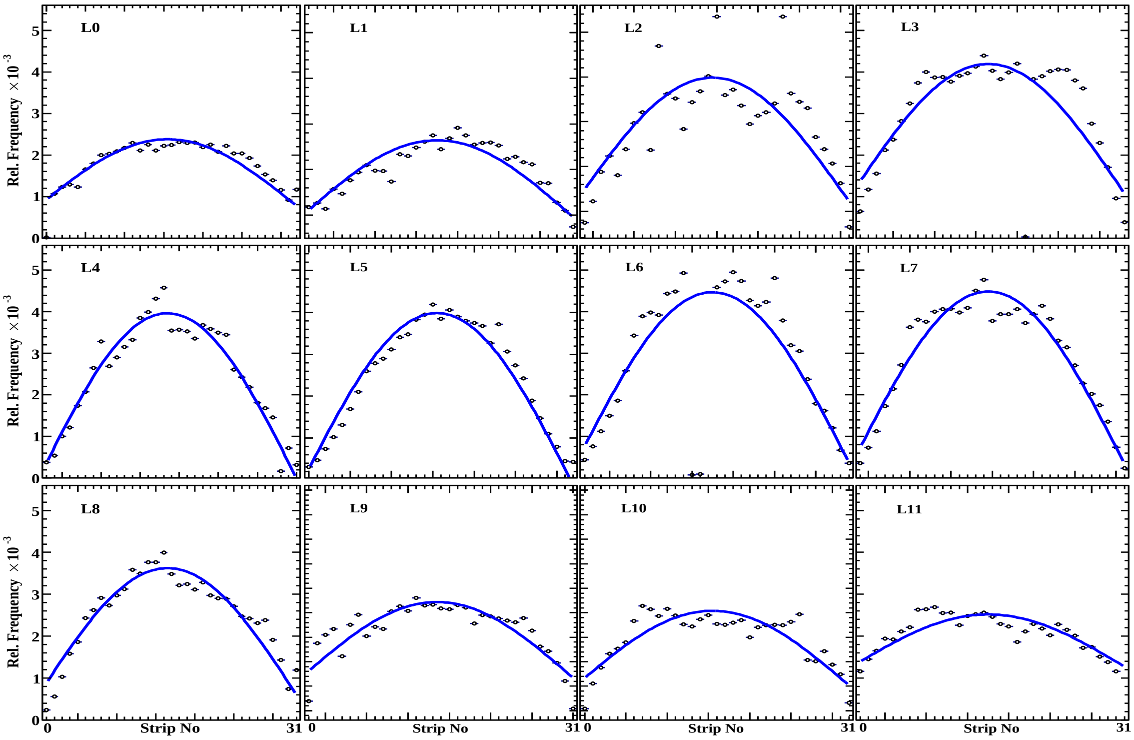

(b) Y-view

Figure 3.1. Relative distributions of the strip hit profile and their fitting. All the distributions are normalised with respect to the total number of events acquired.

the charge from the metal plate and the boundary condition that $\phi = 0$ at $z = 0$. Using Gauss's law $(E = -\nabla\phi)$ surface charge density $\sigma(x, y)$

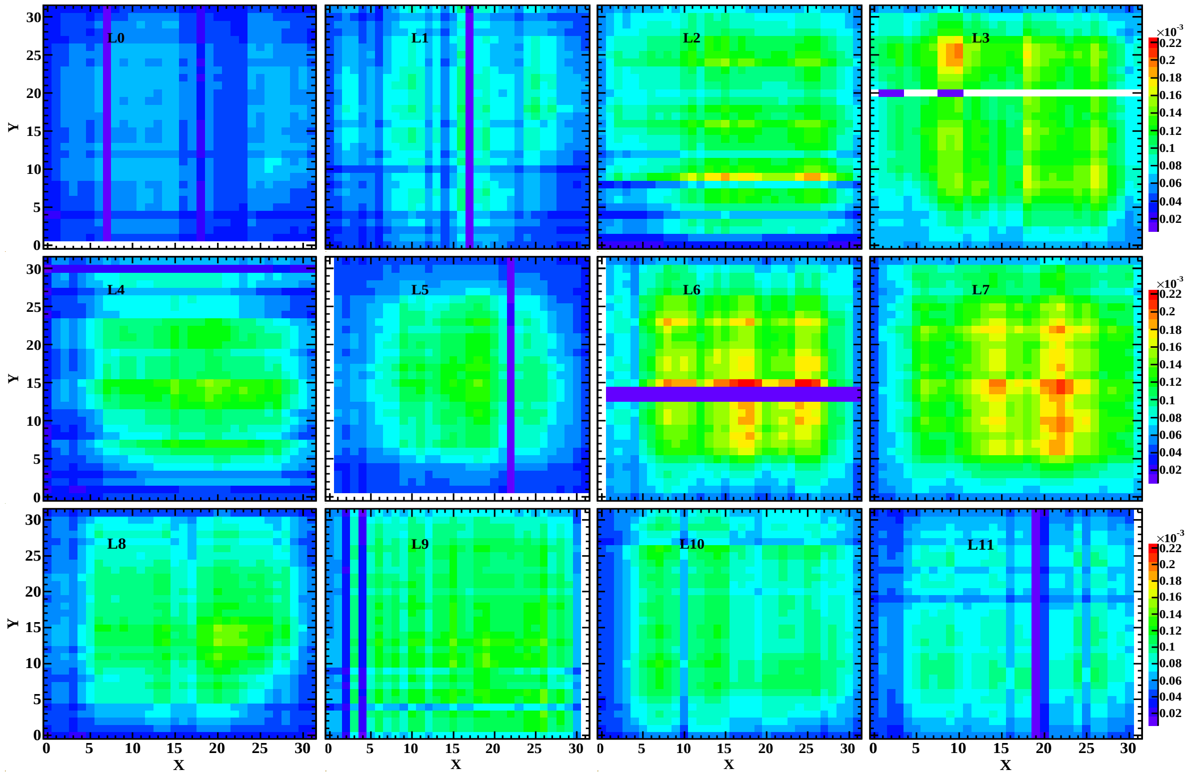

Figure 3.2. Raw occupancy profile for all layers. Distributions are normalised with respect to the total number of events acquired.

can be calculated. The total charge induced on the surface of the metal plate is obtained as $-q$ by integrating the $\sigma(x, y)$ over the plate surface where the limits are $-\infty$ to $+\infty$ for the x and y. Due to this simplicity of the problem we use the method of mirror charge situated opposite to the surface at the same distance z_0. In case of large plate dimensions compared to the distance of the charge from the plate, total charge induced on the plate is independent of the distance of the charge from the plate. But, let us imagine that the metal surface is segmented into strips of width w and each of the strips being grounded. Now, if we want to find the induced charge on the central strip, surface charge density is now has to be integrated over the strip width ($\int_{-w/2}^{w/2} dx$) whereas the y can be still integrated from $-\infty$ to $+\infty$. In this case induced charge is depends on the distance z_0 of the point charge q from the metal surface. If the charge starts moving to the electrode, time derivative of the instantaneous charge is defined as the induced current which flows between the electrode and ground.

Now, drift velocity of electrons is faster than ions. But current produced in the respective electrodes in the RPC happens at the same time. Though the basic principle of the induced current due to a moving charge in the metal electrode with respect to the ground is what we have discussed before, it is more realistic to understand this induced current development in the electrodes due to the change in the electric field lines due to the motion of the electrons inside the gas gap. Technically, it is known as Ramo's theorem [123]. A detail discussion on the signal production in the context of RPC using the Ramo's theorem is given in ref. [111]. Due to the small drift velocity of ions than electrons current induced by them is smaller than electrons. The induced current signal of $N(t)$ charge carriers in a cluster that is moving with the velocity $\vec{v}_D(t) = \dot{\vec{x}}(t)$ at time t is given by [123, 124]

$$i(t) = \vec{E}_w(\vec{x}(t)) \cdot \vec{v}_D(t)\, e_0 N(t), \tag{3.1.2}$$

where, e_0 is the unit charge and $\vec{E}_w$ is the electric field in the gas gap if we put one RPC read out strip on 1 V and ground all other electrodes. The value $\vec{E}_w$ is called the *weighting field*, and it is different from the actual electric field. A schematic plot of the weighting field and the signal induction process is given in Figure 3.3. For n_{cl} clusters moving in the gas gap of a RPC, the induced current signal is the sum over all clusters

$$i(t) = \sum_{j=1}^{n_{cl}} \vec{E}_w(\vec{x}_j(t)) \cdot \vec{v}_{Dj}(t) \, e_0 \, N_j(t) \,. \tag{3.1.3}$$

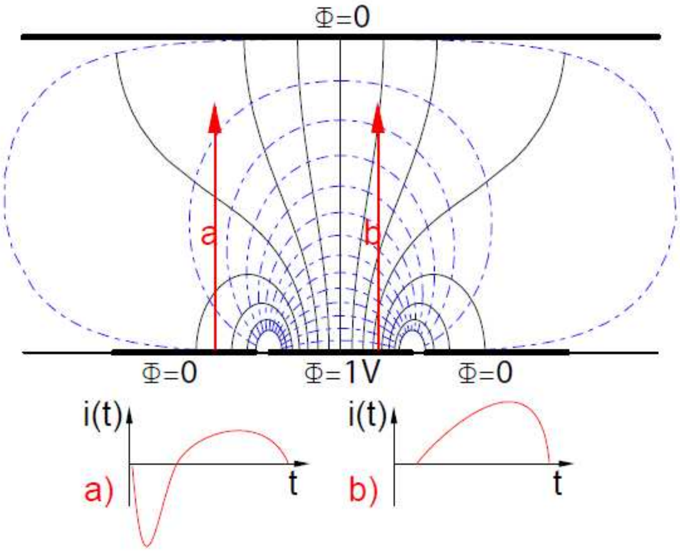

Figure 3.3. A schematic plot of the weighting field in a strip detector and the signal induction process in two examples. The induced current is calculated using the scalar product of the weighting field vector and the velocity vector(s) of the moving charges.

Primary ionisation takes place within a very small area 0.1 cm^2 inside the gas chamber. And the gap between two electrodes is also very small, 0.2 cm. Compared to these dimensions, area of a strip pixel, i.e., overlap area between the X and Y strip, is about 100 times larger. Hence, only single multiplicity in RPC strips are expected as we understand the signal induction process. But there are many other physical factors due to which higher multiplicity is observed in RPC. One of the reasons is the production of secondary avalanche due to photons inside the gas gap. But using isobutane in the gas mixture this possibility is get reduced. It may also happen that the surface resistivity due to graphite coating is not exactly uniform over the electrode surface. If the resistivity is less near the signal production region induction effect may spread over a broader region which can produce multiple strip hits. Moreover, cross talks between two adjacent RPC read out strips may also produce higher multiplicities. When a high frequency signal is passing through a RPC read out strip, which is basically a transmission line, it induces signal to the neighbouring transmission lines. Sometimes, muon pass in between two strips, where ultimate signal induction produce signals in both the strips. Except these, every RPC strip shares common electrical ground and if the net current is high then it may induce signals also in the adjoining strips. A typical nature of layer multiplicity is shown in Figure 3.4. Though the peak of each distribution is around one or two, a long tail exists due to all strip hits in a layer which is due to correlated electronic noise of that layer.

Layers like 2, 9 have maximum occurrence of single multiplicity, whereas, layer 0, 11 have missing hits as there is a large number of events at the 0^{th} bin and layers 4, 6, 7 show maximum times two strip hits. Layers 0, 1, 10 and 11 have more missing hits than others as they are either below of the bottom trigger layer or above the top trigger layer which put them outside the solid angular coverage for large angle muon tracks.

On an average, the frequency of hit multiplicities in a true muon trigger event is 48%, 34% and 16% for single, double and triple occurrence respectively, with an average strip multiplicity of 1.6. In order to select muon hits, either one strip hit or consecutive two or three strip hits in a layer are chosen. Average of strip positions are considered, in case of two or three multiplicities, during muon track reconstruction.

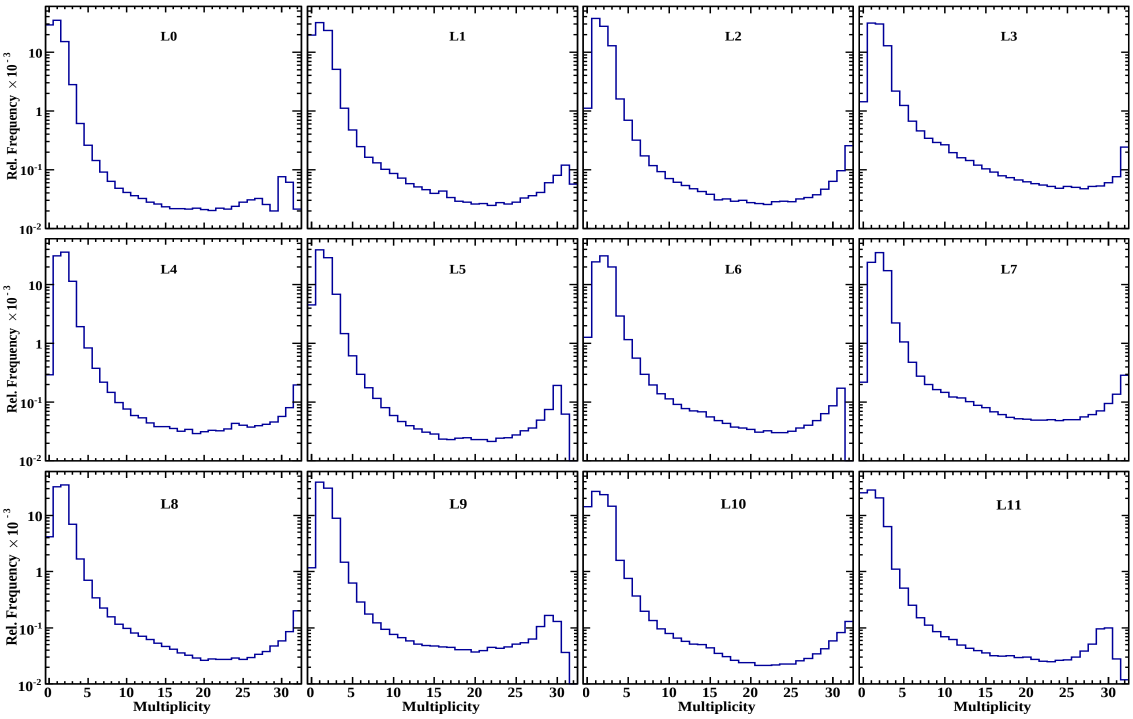

(a) X-view

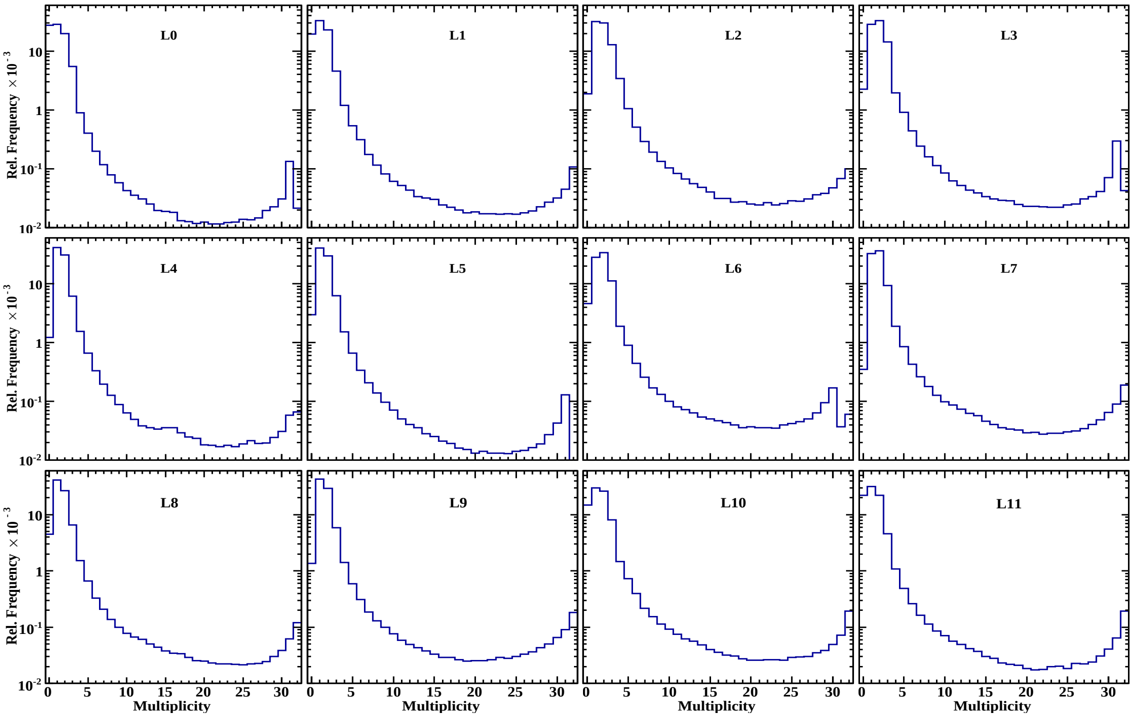

(b) Y-view

Figure 3.4. Relative distributions of layer hit multiplicities for X and Y-view. Distributions are normalised with respect to the total number of events acquired.

3.1.4 Muon track reconstruction

Muon tracks are linear here as magnetic field is absent. Sometimes soft particles (low energy pions, electrons etc.) may also produce tracks, but they are confined within 2 or 3 layers and chance of getting these tracks or multiple muon tracks in this stack is very small. Even if such track is present, due to the above mentioned event selection criteria those are neglected. A typical event display of a good event and a noisy event is shown in Figure 3.5.

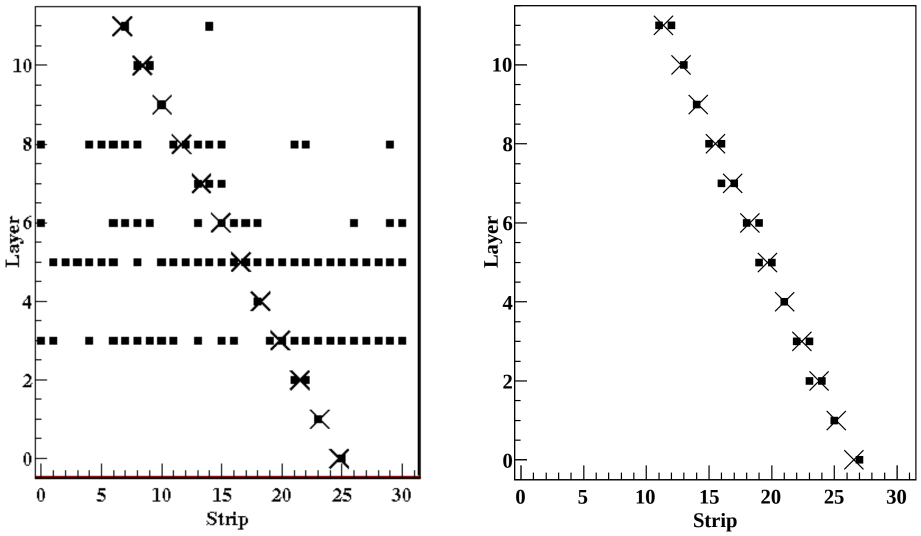

(a) Noisy Event (b) Good Event

Figure 3.5. 3.5a shows a typical noisy event and 3.5b shows a good event. The solid squares are the hits and the crosses are points from the straight line fit made using the algorithm discussed in the text.

3.1.5 Track fitting algorithm

Selected strips in the X-view and the Y-view are fitted separately with Least Square method of linear fitting (eq. 3.1.4),

$$x(/y) = a \times z + b \tag{3.1.4}$$

where, x or y are the respective coordinates of strip/hit from the X-view or Y-view respectively for the z-th layer, a is the slope and b is the intercept. The error matrix of the linear fitting is defined as,

$$\frac{1}{D}\begin{pmatrix} [z^2] & -[z] \\ -[z] & [1] \end{pmatrix} \tag{3.1.5}$$

where, the quantities in square brackets and the determinant D are given by,

$$\begin{aligned} [\chi] &= \sum_{i=1}^{n} \frac{\chi_i}{\sigma_i^2}, \\ D &= [z^2][1] - [z][z]. \end{aligned} \tag{3.1.6}$$

In eq. 3.1.6, n is the total number of data points used in the fitting and σ_i is the uncertainty in the y-coordinate for X-view (and vice versa) which is later on defined as σ_{pos}. The fit point (x' or y') is then estimated per layer along with the estimation error (σ_x or σ_{y}).

$$\sigma_x^2 = z^2\sigma_b^2 + 2z\,cov(a,b) + \sigma_a^2 \tag{3.1.7}$$

where,

$$\begin{aligned} \sigma_a^2 &= \frac{[z^2]}{D}, \quad \sigma_b^2 = \frac{[1]}{D}, \\ cov(a,b) &= \frac{-[z]}{D}. \end{aligned} \tag{3.1.8}$$

The distribution of $\sigma_{x/(y)}$ for all the layers are shown in Figure 3.6. Variation in error for the extrapolation either for bottom or top layers are seen larger than in between middle layers. This phenomenon is common in any kind of polynomial fitting where larger extrapolation errors are expected at edges than the middle confined points. A hit is rejected

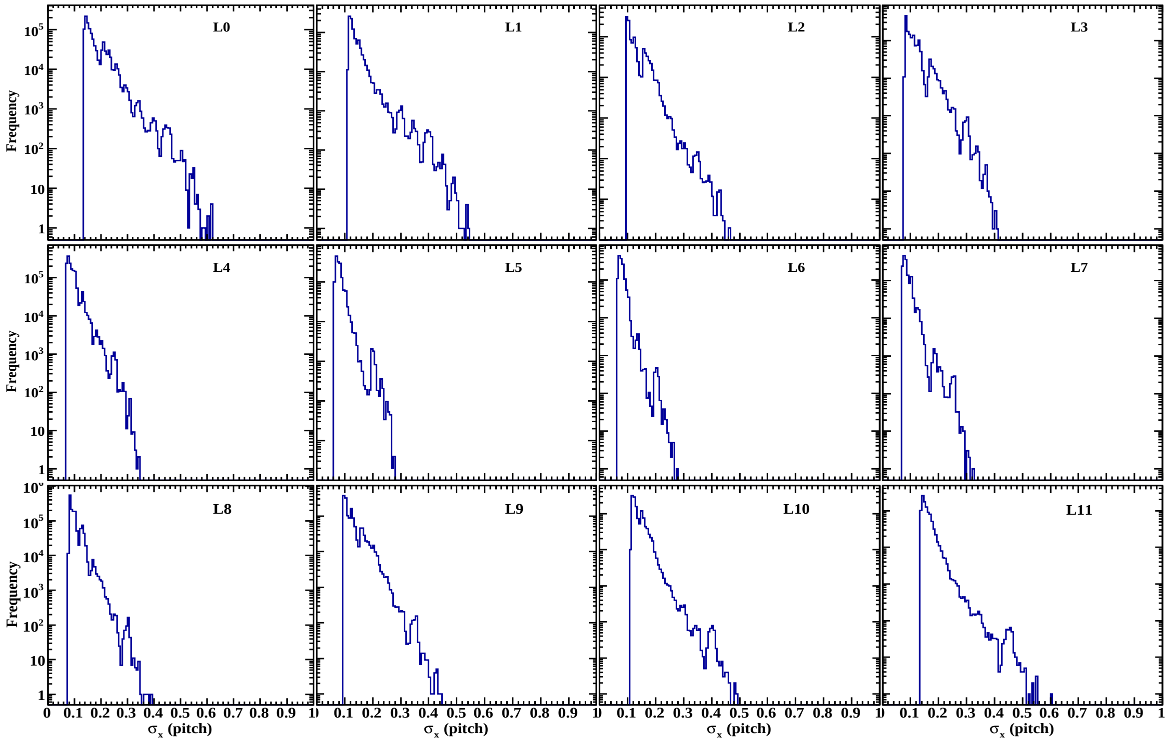

(a) X-view

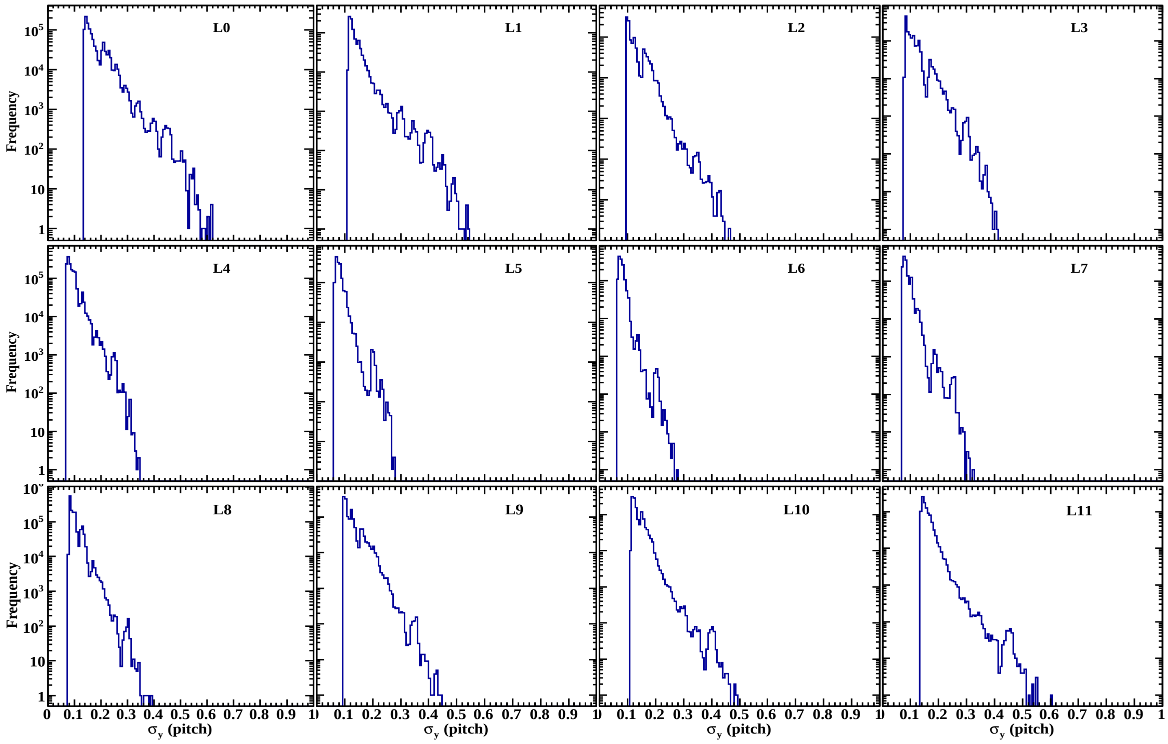

(b) Y-view

Figure 3.6. Extrapolation error of the strip hit for each layer for the both the views are shown.

if $|\Delta R| >$ one strip pitch, where ΔR is the residual defined as the difference between a hit and fit position ($\Delta R = x(/y) - x'(/y')$), and another fit is made for the same event with remaining hit points. It was observed that after the second trial hardly ($\sim 0.001\%$) any data point get rejected due to the above mentioned condition. Normally, a hit is rejected after the first trial only due to outliers. To avoid a bias in the determination of the layer residual, the calibrating layer is excluded from the fitting and its residual (ΔR) is obtained. This procedure is followed by excluding one layer at a time and the residuals for all 12 layers are estimated.

3.1.6 Position residue

Thanks to the good mechanical accuracy and by using alignment corrections derived by muon tracks, an overall position accuracy better than 1 mm is obtained. Typical position residue distributions are shown in Figure 3.7a. Mean of the position residue distributions are used as position offsets for a layer, which is shown in Figure 3.7b along with their RMS values. Quoted numbers in the Figure 3.7 are from the Gaussian fit to the individual distributions. Statistical error to the mean and RMS to these distributions are very small, about 10^{-6}, and not shown in the figures.

3.1.7 Position resolution and the χ^2 definition

Muon hits in the RPC strips are read by the strip number. So, any real position on the strip is equally probable through which the muon has passed and this impulses to consider position resolution, σ_{pos}, as $1/\sqrt{12}$ (in strip unit). Perfect selection of the σ_{pos} is reflected in the reduced χ^2 distribution. An overestimation in the σ_{pos} shifts the peak towards

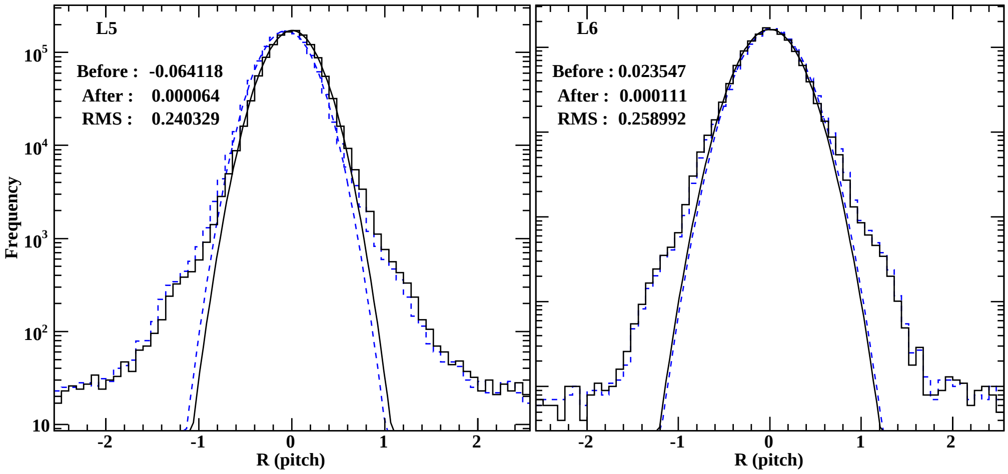

(a)

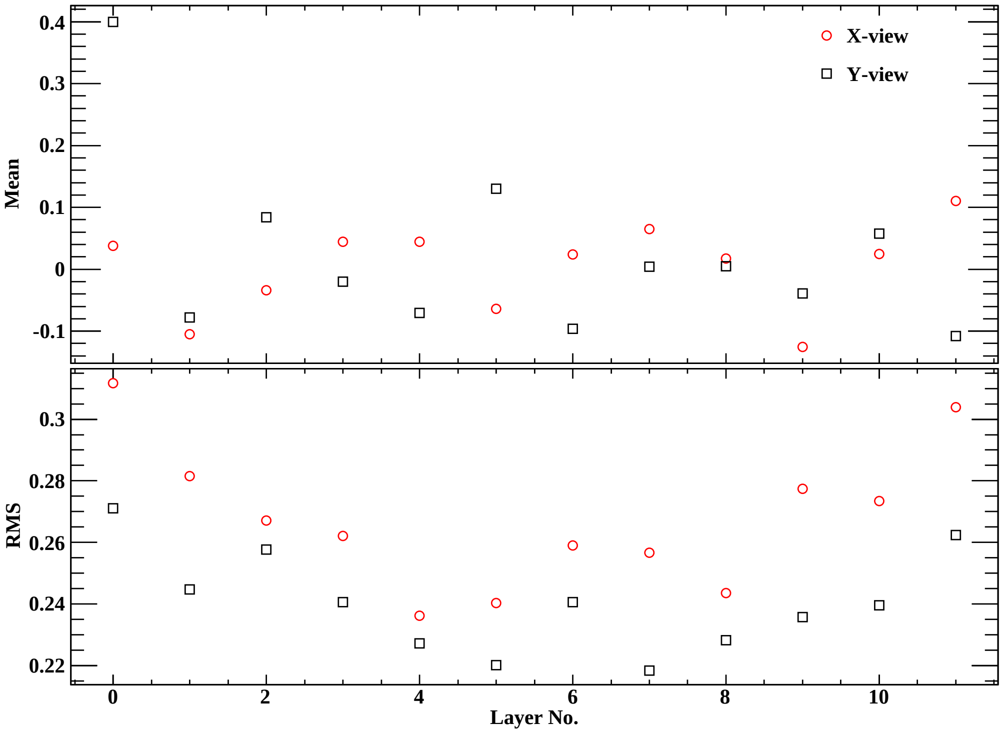

(b)

Figure 3.7. 3.7a shows typical position residue distributions, before (dotted blue line) and after correction (continuous black line) and their Gaussian fit for the layers 5 and 6 (X-view). The mean and RMS values of these position residue distributions for both the views are shown in 3.7b.

lower side from 1 and vice versa. RMS values of the position residual distributions are thus used as σ_{pos} for individual layers instead of having a constant value. In contrary to the previous section, all the selected layers are present in fitting while determining the position residuals for each layer. This particular choice is followed, because combined fitting of the data of all selected layers are later on used for physics analysis, like muon flux measurement or the directionality study etc. Position residual distributions for three cases of multiplicities for the X-view are shown in Figure 3.7. Average of RMS values over all the layers for each case is defined as σ_{pos}, which is 0.184, 0.185 and 0.273 (in strip units) for single, double and triple hit multiplicities respectively. This selection of σ_{pos} improves the mean of the reduced χ^2 distribution of the track fitting as shown in Figure 3.8, where two cases are mentioned, a constant $\sigma_{pos} = 1/\sqrt{12}$ and the used variable σ_{pos} for different cases of multiplicities. On an average, RMS values of the position residual distributions (Figure 3.7), including all three cases of multiplicities, appear to be about $1/\sqrt{12}$.

Tracks to be used in the analysis were required to have hits in both X and Y views and at least two degrees of freedom (ndf = $\mathrm{N} - 2 > 2$, N being the number of layers used in the fit). We also require a good fit by asking $\chi^2/\mathrm{ndf} < 2$ in both views.

3.1.8 Trigger and tracking efficiency

Selected muon events based on the reduced χ^2 and ndf quality criteria are used to determine trigger and tracking efficiencies for all layers. Separate trigger criteria are essential here than the normal trigger criteria used to track muons (discussed in section 2.2.1). This separate trigger helps to gain in the solid angular coverage so that entire detector is well inside it and each portion of the detector should have enough events. Layers 0, 1, 3 and 4 are used in trigger formation to get efficiencies for layer 6 to 11 and layers 7, 8, 10 and 11 are used to get efficiencies for

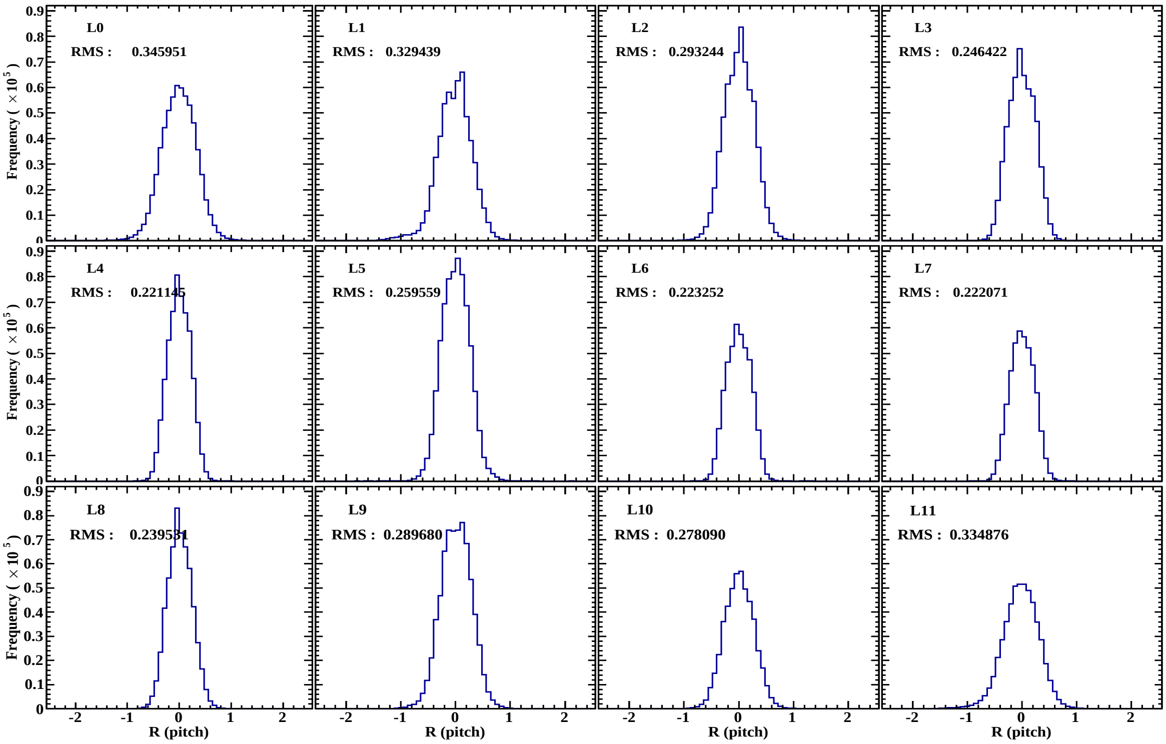

(a) Multiplicity = 1

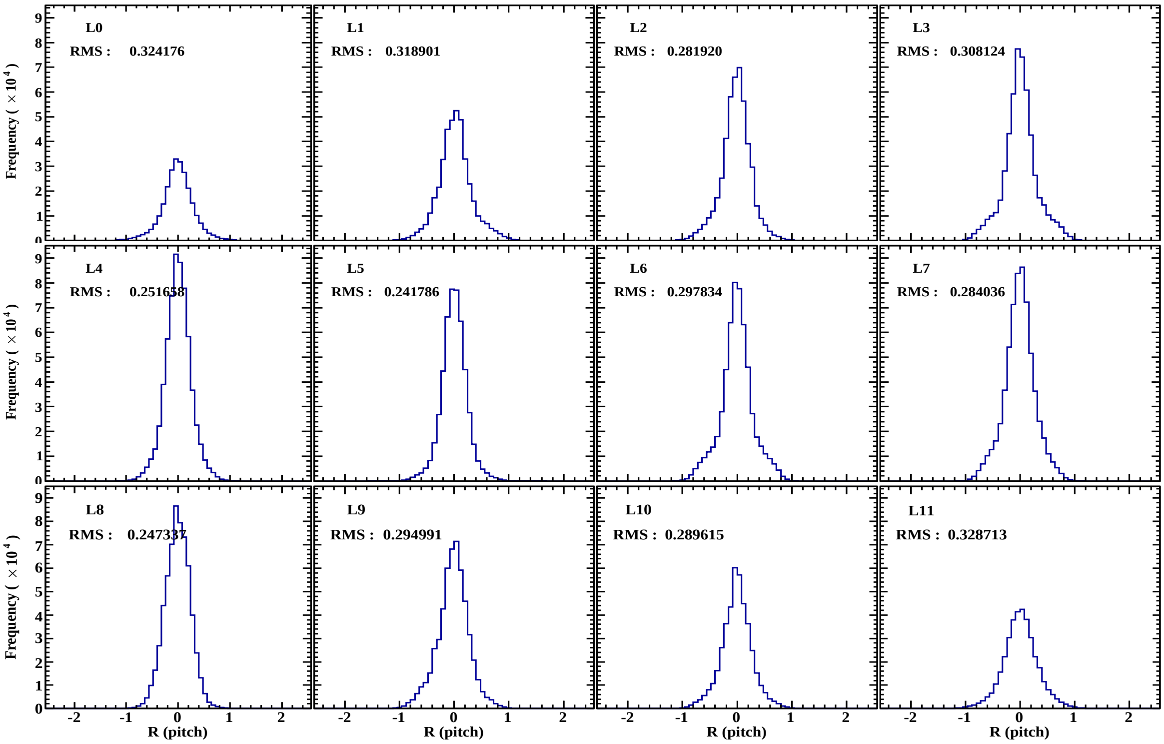

(b) Multiplicity = 2

Figure 3.8. Residual distributions (X-view) for different cases of multiplicities.

other layers. Data from these two different trigger schemes are analysed in the same way as described above. Apart from the fitting procedure

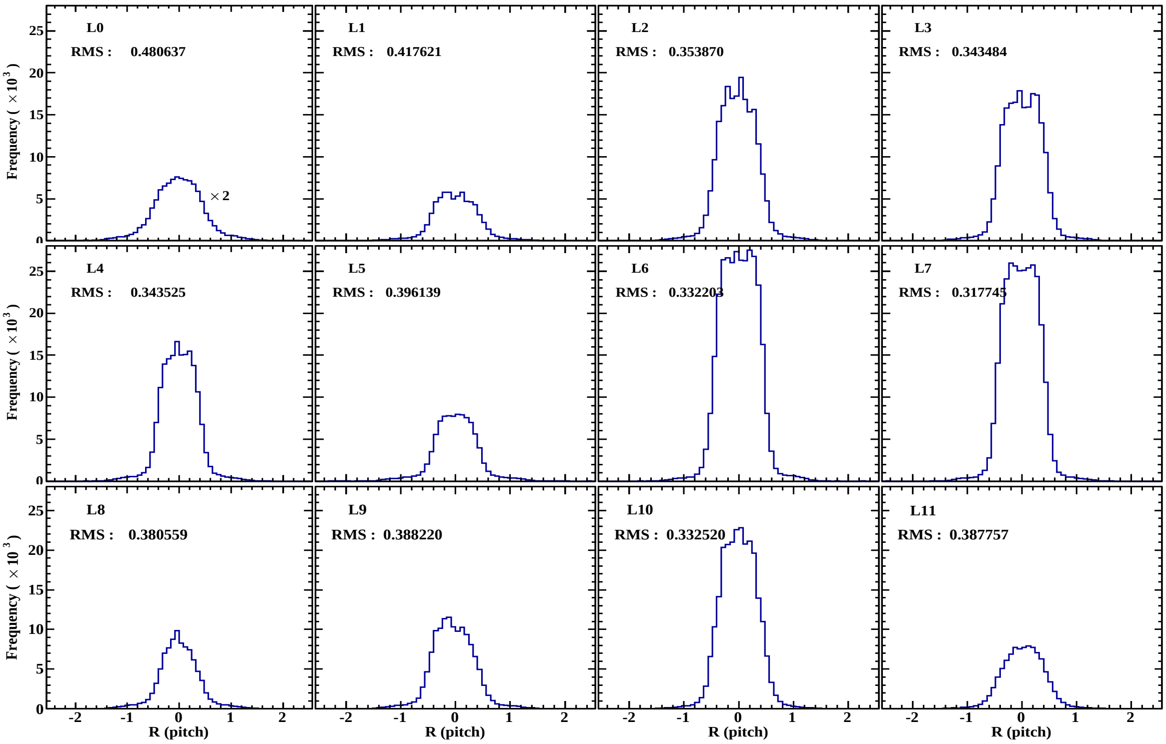

(c) Multiplicity = 3

Figure 3.7. Contd.. Residual distributions (X-view) for different cases of multiplicities.

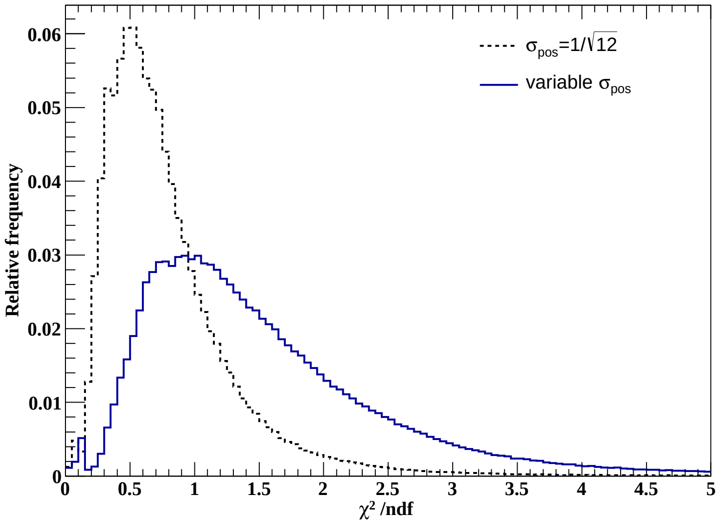

Figure 3.8. Comparison of reduced χ^2 distributions with constant σ_{pos} and variable σ_{pos}.

and event selection criteria after track fit, as discussed above, additional selection criteria (X and Y-view together) is used to minimise the error in fit and to get a better 2-D efficiency map.

- Error on extrapolated/interpolated x/y position ($\sigma_{x/y}$) should be $<$

0.2.

- The deviation (δ) of a fit point from the mid point of a strip is calculated.

- A fit point is accepted if $|\delta| + \sigma_{x/y} < R'$, where R' is equal to 1.25 of the strip pitch. This additional quarter width of a strip is added in the search window to ensure averaged raw muon hit in case of triple multiplicity are within it. Accepted fit points per pixel per layer are filled in a 2-D histogram, say h_{Total}.

- More than one strip in a trigger layer may have hits and that also will produce trigger. But during the track fitting, hits from this layer may be rejected. So, to get 2-D trigger efficiency map, the difference between a fit point and the actual strip hit recorded in data is estimated and accepted if deviation is within R' . This broader window is chosen since maximum of three consecutive strip hits are accepted as a muon signal from a RPC.

  Fit points are accepted in a layer if any strip of that layer has signal and then accepted fit points are filled pixel-wise, i.e., corresponding to the particular $(x, y$ coordinate, for each layer in another 2-D histogram, say h_{Trig} and division of h_{Trig} by h_{Total} gives 2-D trigger efficiency profile for all layers.

- The residual (ΔR) is considered within a strip pitch for tracking efficiency measurements. Accepted fit points are then filled in another 2-D histogram (say h_{Effi}). Division of h_{Effi} by h_{Total} similarly gives 2-D tracking efficiency profiles.

Strip multiplicity is stored as a function of extrapolated muon trajectory in a strip (i.e., δ) for each layer for both the views as shown in Figure 3.9. In case of zero multiplicity or multiplicity higher than three the δ value is equally probable within the strip. The occurrence of these cases are less as we see most of the times single or double multiplicities in a layer. Due to inefficiencies in the layers 1, 2, 4, 11 etc. in the X-view we see occurrence of zero multiplicity than the other layers. In case of consecutive three strip hits, average hit position appears at the middle of the central strip. So, δ value is equally probable on either side of the central position of the central strip. This behaviour is visible for layers 6, 7, 10 in the X-view data. For single strip hit, there is no averaging involved in the strip position and hence, δ value is expected to be peaked around central position of the strip as shown for all the layers in both the views. In case of consecutive two strip hits, the average position appears at the edge of both strips which make δ to be peaked around the either edge of the strip depending on either left or right with respect to the central position of a strip. The 2-D tracking efficiency profiles for all the layers are shown in Figure 3.10.

3.1.9 Iterative process

To align all detectors and to have better estimate of all tracking efficiencies, this fitting process is repeated iteratively, i.e., from section 3.1.4 to section 3.1.8, where residuals are corrected and updated in each iteration. After $4-5$ iterations, no appreciable change is noticed in the mean and RMS of the residual distributions. The fit parameters of the last iteration are considered for the following analysis.

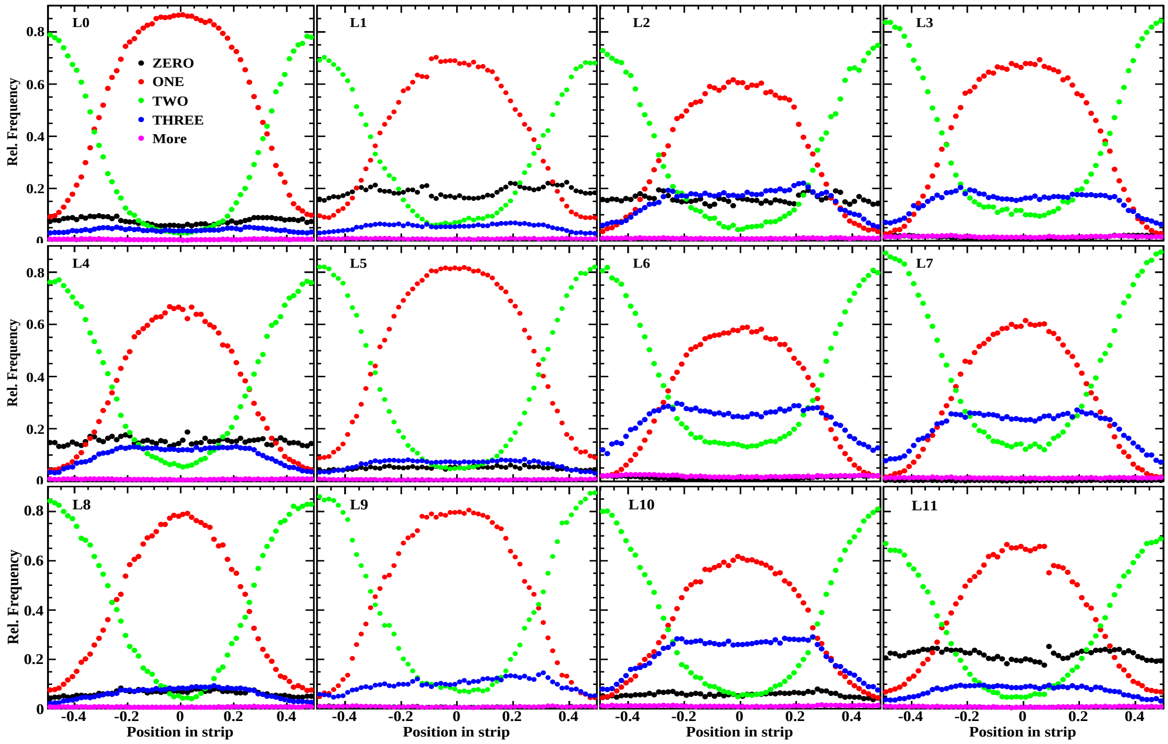

(a) X-view

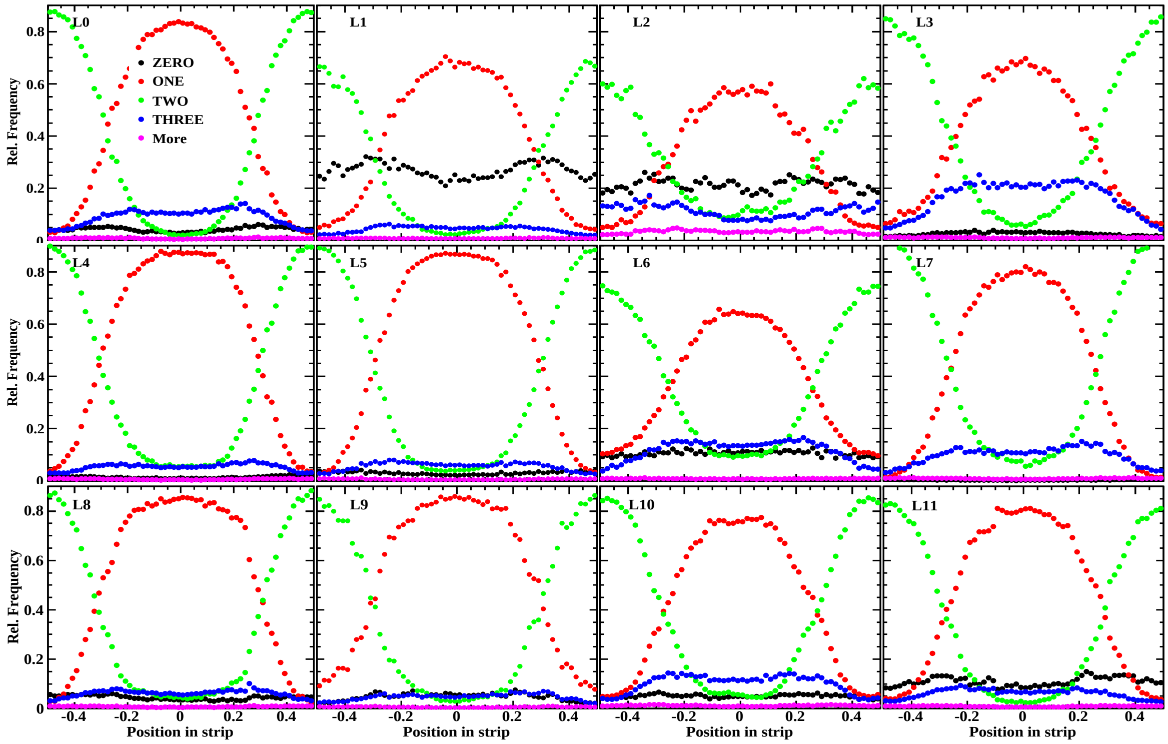

(b) Y-view

Figure 3.9. Strip multiplicity as a function of extrapolated muon trajectory in a strip.

3.1.10 Zenith angle distribution

Individual track fitting results from both the views are used to calculate the zenith angle (θ) of incoming muons. The θ is defined as,

$$\theta = cos^{-1}\left(\frac{h}{l}\right) \tag{3.1.9}$$

where, h is the stack height and l is the track length between 0^{th} and 11^{th} layer. The θ distribution with different quality criteria (as mentioned below) are shown in Figure 3.11.

1. $\chi^2/ndf < 2$ and N > 4,
2. all trigger layers (X-view only) have raw hits,
3. all trigger layers (X-view only) data is used in the fitting,
4. data from all the trigger layers of the Y-view is used in the fitting,
5. $|R| <$ one strip pitch for all the trigger layers for both the views.

These quality criteria do not change the shape of the observed θ distributions, but it is important in the MC analysis, where this criteria helps to reduce the error between simulated and reconstructed zenith angle (Figure 3.17).

3.2 Monte-Carlo (MC)

The cosmic muon analysis is also verified through a MC simulation. The hit positions in the MC are smeared (in terms of position) and according to the resolutions observed in real data. The track fitting and analysis of simulated data are carried out using the same procedure applied to real data.

3.2.1 Generation of muon trajectory

First the impact points on the 9th layer, the top trigger layer, (x_9, y_9) are generated using a uniform distribution. The direction of the track is then fixed by the simulated zenith angle (θ_s) and the azimuthal angle (ϕ_s) and the hit points for intermediate layers are obtained. The θ_s angle is generated uniformly over the solid angle and ϕ_s angle uniformly over the $0-2\pi$ range (eq. 3.2.1).

$$\begin{aligned} X &= m\, cos\theta_s\, +\, c \\ Y &= m'\, \phi_s\, +\, c'\,. \end{aligned} \tag{3.2.1}$$

X and Y are the uniform random numbers in eq. 3.2.1 distributed in between 0 and 1. Constants, m, c etc. are determined here using suitable boundary conditions, which are given by:

$$\begin{aligned} X\, &=\, 0\;\; \text{at}\, \theta_\text{s}\, =\, 0\;\, \Rightarrow\, c\, =\, -m \\ X\, &=\, 1\;\, \text{at}\, \theta_\text{s}\, =\, \tfrac{5\pi}{18}\, \Rightarrow\, m\, =\, \frac{1}{cos\frac{5\pi}{18}\, -\, 1} \\ Y\, &=\, 0\;\; \text{at}\, \phi_\text{s}\, =\, 0\;\, \Rightarrow\, c'\, =\, 0 \\ Y\, &=\, 1\, \text{at}\, \phi_\text{s}\, =\, 2\pi \Rightarrow\, m'\, =\, 1\,. \end{aligned} \tag{3.2.2}$$

The maximum range in θ_s is chosen as 50° as no events are observed after that (Figure 3.11) in this particular trigger criteria (layers 2, 4, 7 and 9 are in trigger). The θ_s angle distribution is similar as shown in Figure 3.11. While two adjacent layers are considered, the maximum angle subtended by the edge of a strip on the upper layer w.r.t. to the centre of the same strip on the lower one is $\sim\, 5.0^\circ\, (\theta_1)$. If the range is taken up to the edge of the same strip then it is $\sim 9.9^{\circ}\,(\theta_2)$, and if it is up to the centre of the next strip on the lower layer then the maximum angle becomes $\sim 15.4^{\circ}\,(\theta_3)$ and up to the edge of that strip is $\sim 19.9^{\circ}\,(\theta_4)$ (Figure 3.13).

Exactly vertical tracks ($\theta_s = 0^{\circ}$) are not possible due to the solid angular effect ($sin\theta\, d\theta$), but in reality we are not dealing with a point but a pixel whose area is 3×3 cm^2. So, very few events are visible in the 1^{st} angular bin. And then number of events start rising from 10° onwards. Again, very large angle tracks can not be detected due to the geometry of the detector, which is constrained by the total height and the base area of the detector. When muons pass through almost diagonally from the top plane to the bottom plane of the detector, then ϕ_s angles are 45°, 135° etc., and in this case range of θ_s is maximum. Due to this fact a periodic behaviour is observed for the ϕ_s angle with the θ_s angle as shown in Figure 3.12.

3.2.2 Comparison of hits between data and MC

Hit distribution of the top trigger layer, the 9th layer, is plotted using selection criteria that the fitted points in the 9th layer match with the raw hits when the 2nd layer also has raw hits (Figure 3.14a). The symmetric nature in the distribution is observed with respect to the centre of the plane as expected due to the solid angular effect. Similarly, hit distribution is plotted for the bottom trigger layer, the 2nd layer when track fit selects a raw hit in the same plane (Figure 3.14b). Asymmetry in the hit distribution near the 0th strip corner in Figure 3.14b is observed which is due to the detector inefficiency. Hit distributions are also plotted in

MC for the 9th layer when 2nd layer has a hit (Figure 3.14c) and the hit distribution itself for the 2nd layer (Figure 3.14d). A good agreement in the hit distributions between data and MC is observed (viz., comparison between Figures 3.14a & 3.14c and between figures 3.14b & 3.14d.)

3.2.3 Smearing effects to the generated hits

Resolutions in position measurement are first applied to the generated hits to implement real alignment situations like in data. Hits are then digitised and accepted within 0 to 31 as in data RPC strip hits due to muons are read by the same numbers.

It is also observed that muon track detection efficiencies are not uniform over the RPC area. A hit in a layer is accepted according to a 2-D efficiency map obtained from the data. Two approaches are followed here. First, a uniform random number is generated and if it is less than the observed efficiency for that particular pixel, hit is accepted. In another method, it is assumed that there is a constant value along with a slope over the deviation of the strip position from its central point. But in practice, no appreciable change is observed between these two methods.

A further level of smearing to these hit positions is done to simulate the hit multiplicity effect. In a real scenario, up to three consecutive strip hits are considered as a muon signal from the RPC. Averaging of the strip number for multiplicity greater than one creates uncertainty in the actual hit information. This effect is generated here using the measured multiplicity distributions of detector layers. An assumption is made here that the percentage occurrence of multiplicity (ϵ) in a layer follows linearly with the $\delta' = \frac{\delta}{\omega}$ (section 3.1.8), ω is the strip width and δ is the distance of muon position with respect to strip centre.

$$\epsilon = m\,\delta' + c \tag{3.2.3}$$

Boundary conditions are assumed as follows:

$$\begin{aligned} \delta' &= 0, \quad \epsilon = 0 \qquad \Rightarrow c = 0\,, \\ \delta' &= 0.5, \epsilon = 2\epsilon_{avg} \Rightarrow m = 4\,. \end{aligned} \tag{3.2.4}$$

where, ϵ_{avg} is the observed average multiplicity in data. A uniform random number is generated (r), and if $r < \epsilon$ the strip is shifted by an amount $\omega/2$ either in positive or negative direction depending on δ is positive or negative. In case $r > \epsilon$, another random number is generated (r_1) and if r_1 is smaller than the occurrence of average three strip multiplicities, the strip is shifted by an amount ω either in positive or negative direction 10% of times. At the end, applied layer offsets are again corrected.

3.2.4 Track fitting

The track fitting and analysis of these selected hits are done using the same procedure applied to real data. 2-D efficiency profiles are also regenerated using simulated data to compare with the used 2-D efficiency maps from real data. The number of layer distribution used in the track fitting is shown in Figure 3.15 for data and MC. The reduced χ^2 distribution for the track fitting is shown in Figure 3.16 for data and MC. Similar quality criteria used in data (Section 3.1.10) are also used here to have the simulated zenith angle distribution (θ_s). The final θ_s distribution, i.e., after all the quality criteria, are used to estimate detector differential aperture as described in the next section.

3.2.5 Differential aperture of the detector

The observed θ_s distribution provides the shape of the differential aperture or the solid angular acceptance of the prototype stack. All observed systematics in the data are included here. A proper normalisation (λ) to this obtained θ_s distribution is required to get the differential aperture.

$$\lambda = \frac{AN'}{N} \int_0^{\frac{5\pi}{18}} sin\theta_s \, d\theta_s \int_0^{2\pi} d\phi_s \quad (\mathrm{cm^2 sr}) \tag{3.2.5}$$

N is the total number of random number samples generated over the solid angle and throughout the area A of the 9^{th} layer and N' is the accepted number of events when (x_2, y_2) are within the RPC area. The range for θ_s is chosen similar to the observed θ distribution in data. The distribution of the differential aperture ($\omega(\theta_s)$) is shown in Figure 3.18.

3.2.6 Muon flux measurement

Primary cosmic rays arrive isotropically at the top of the Earth's atmosphere. But muon flux observed on the Earth's surface (i.e., at sea level) or at a certain altitude or depth from the sea level has a zenith angular dependence. The general distribution of the measured flux is of the form $I(\theta) = I_0 cos^n\theta$ ($\mathrm{cm^{-2}s^{-1}sr^{-1}}$), where I_0 is defined as the vertical flux and $I(\theta)$, in general, is the flux at an angle θ. The exponent, n, is observed to vary over a wide range depending upon muon cut off momentum, latitude and altitude etc. The observed data can be parametrised by the following equation:

$$\int_{\theta}^{\theta+d\theta} N_{obs}(\theta)\,d\theta = \int_{\theta}^{\theta+d\theta} I_0 cos^n\theta\,\omega(\theta)\,d\theta \tag{3.2.6}$$

where, $N_{obs}(\theta)$ shows observed number of events per second in a θ bin and $\omega(\theta)$ is the differential aperture of the stack. It is to be noted that limits of the integration in eq. 3.2.6 is shown for θ only. In this detector set up, ϕ can be integrated from $0-2\pi$ for a certain values of θ. The ϕ integration, which comes from the solid angle, is actually involved in determination of the $\omega(\theta)$ distribution. As no analytical integration is actually involved to estimate $\omega(\theta)$, the dependency of ϕ over θ appears in an indirect way through the selection of a hit point in the bottom trigger layer for certain θ and ϕ.

The experimentally observed θ distribution of events $(N_{obs}(\theta))$ and the $\omega(\theta_s)$ distribution for the detector solid angular acceptance are used to estimate statistically the best fit value for I_0 and n using the χ^2 minimisation process. The χ^2 is defined as,

$$\chi^2 = \sum_{\theta=0}^{\theta_{max}} \frac{(N_{obs}(\theta) - I_0 cos^n\theta \times \omega(\theta))^2}{N_{obs}(\theta)} \tag{3.2.7}$$

The best fit value of n (eq. 3.2.8) gives the actual shape for the cosmic muon angular distribution.

$$n = 2.150 \pm 0.011 \tag{3.2.8}$$

While determining the shape of the muon flux distribution, θ_s was generated uniformly over the solid angle (eq. 3.2.1) to get the shape of the zenith angle distribution. But to estimate I_0, θ_s has to be generated considering the actual cosmic ray flux distribution as obtained above, i.e., $\frac{dN}{d\theta_s}\propto cos^{2.15}\theta_s$.

I_0 obtained afterwards from minimisation process needs a proper normalisation to give the vertical flux. The normalisation factor ξ is given by eq. 3.2.9.

$$\xi = \xi_{trigger} \times \xi_{selection} \times T \times \lambda^{'} \tag{3.2.9}$$

T is the total time (second) taken to record the entire data set including DAQ dead time correction (about ms/event here). $\xi_{trigger}$ is a fraction of selected events by the trigger condition to the number of incident events on the top trigger layer $\left(\text{i.e.}, \xi_{\text{trigger}} = \frac{\text{N}_{\text{trigger}}}{\text{N}_{\text{incident}}}\right)$. $\xi_{selection}$ is a fraction of selected events by the track reconstruction algorithm to the number of triggered events $\left(\text{i.e.}, \xi_{\text{selection}} = \frac{\text{N}_{\text{selected}}}{\text{N}_{\text{trigger}}}\right)$. $\lambda^{'}$ is the solid angular acceptance factor. It differs from λ as observed cosmic muon flux distribution is taken into consideration for the solid angular acceptance part as shown in eq. 3.2.10.

$$\lambda^{'} = \frac{AN^{'}}{N} \int_0^{\frac{5\pi}{18}} cos^{2.15}\theta_s \, sin\theta_s \, d\theta_s \int_0^{2\pi} d\phi_s \quad (\text{cm}^2\,\text{sr}) \tag{3.2.10}$$

The modification for λ to $\lambda^{'}$ is necessary, otherwise ξ is overestimated and I_0 becomes underestimated. The best fit value of I_0 after normalisation comes out to be,

$$I_0 = (6.217 \pm 0.005) \times 10^{-3} \quad \text{cm}^{-2}\,\text{s}^{-1}\,\text{sr}^{-1} \tag{3.2.11}$$

The experimentally observed muon flux distribution normalised by ξ is shown in Figure 3.19.

3.3 Chapter summary

The selection of muon hits and track reconstruction procedure is described in this chapter. Detailed discussion on position resolution is presented here. Tracking efficiencies of RPC layers are discussed. Inefficiency observed in some layers is an experimental fact. Detail study of these inefficiencies and how to overcome it is beyond the scope of this thesis. Different experimental arrangements are already planned to study it, both in the experimental and simulation level. Zenith angle distribution of the observed muons are also shown with different quality criteria.

Muon data is simulated considering all observed systematics. Effects of strip multiplicities, tracking efficiencies are considered here while calculating detector differential aperture. Muon flux spectrum at sea level are fitted and vertical flux is measured using this prototype stack.

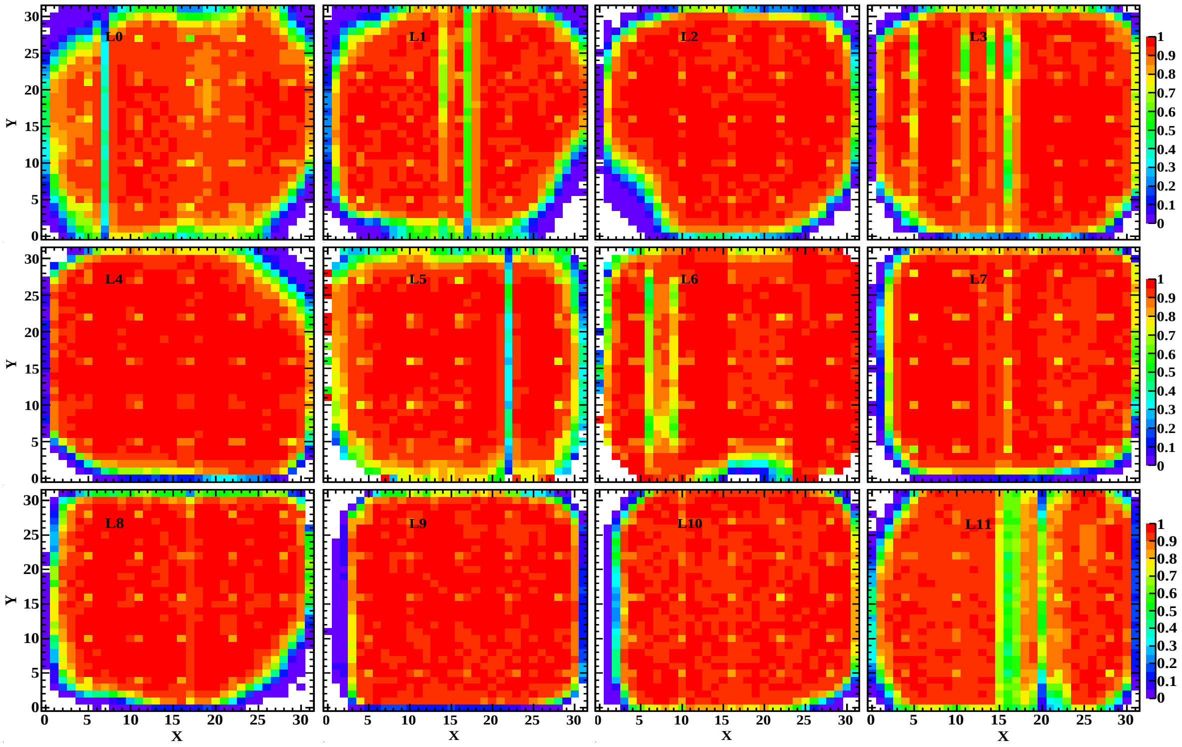

(a) X-view

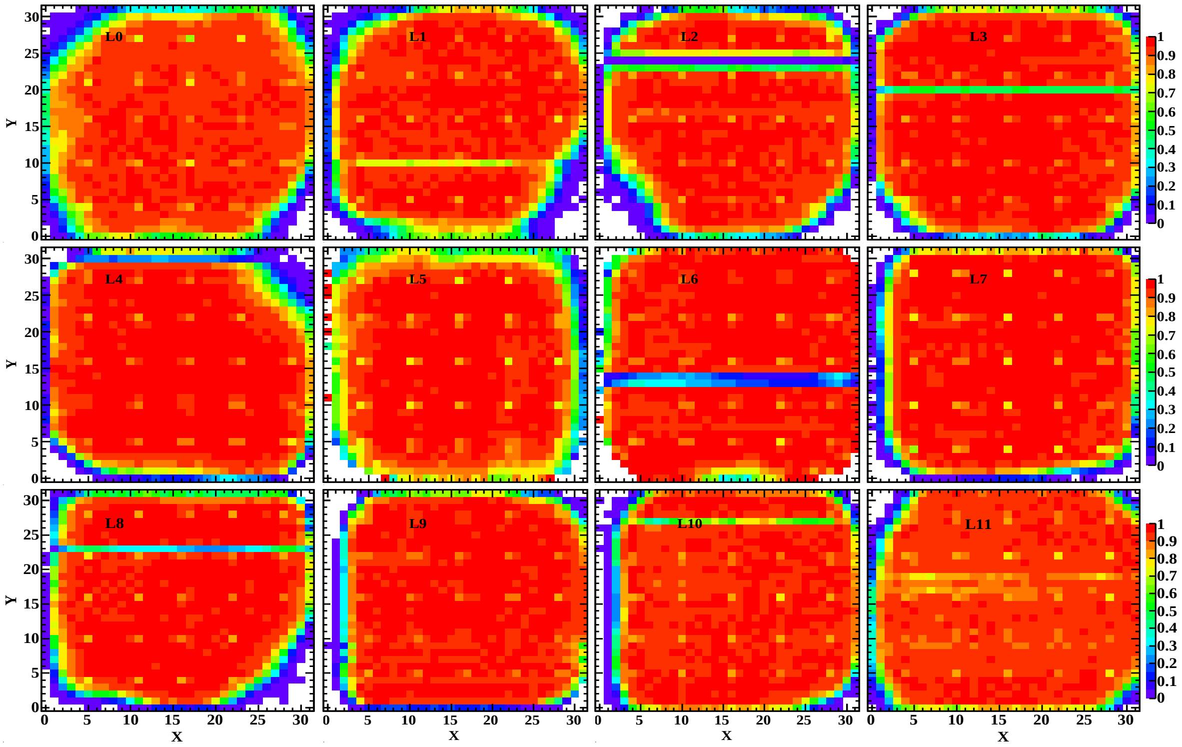

(b) Y-view

Figure 3.10. Tracking efficiency for all layers are shown for both the views. The regular pattern of pixels with efficiencies of 0.8 (orange) embedded in the red regions with efficiencies of 0.9 are due to button spacers, which are put to maintain uniform gap between the two electrodes. The continuous patch (green) along the 17th strip in X-axis of layer 1 in the X-view is due to a dead strip and similarly for other layers but the colour may change depending on the number of events.

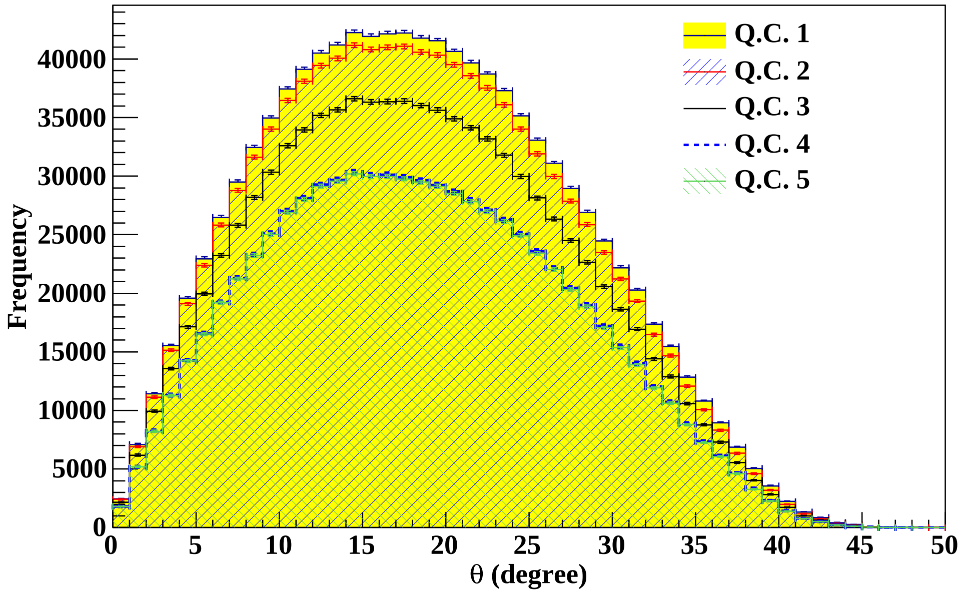

Figure 3.11. Zenith angles with all quality criteria. Any quality criterion always include previous quality criterion or criteria.

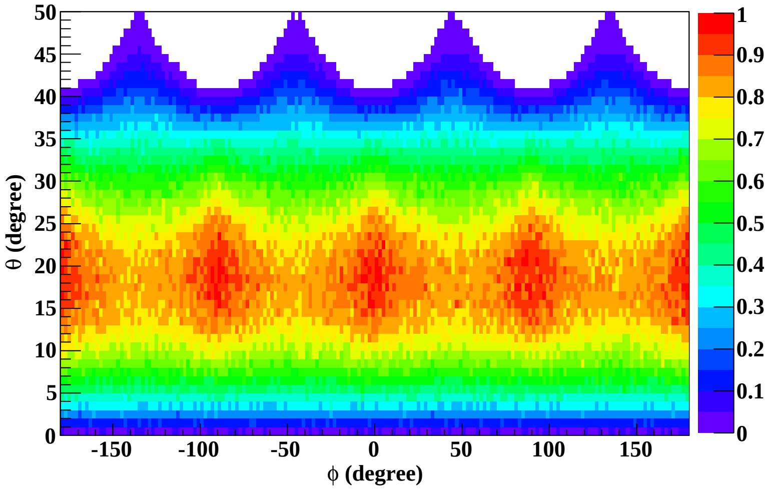

Figure 3.12. The correlation between the angles θ_s and ϕ_s is shown. Distributions are scaled with their maximum number of counts.

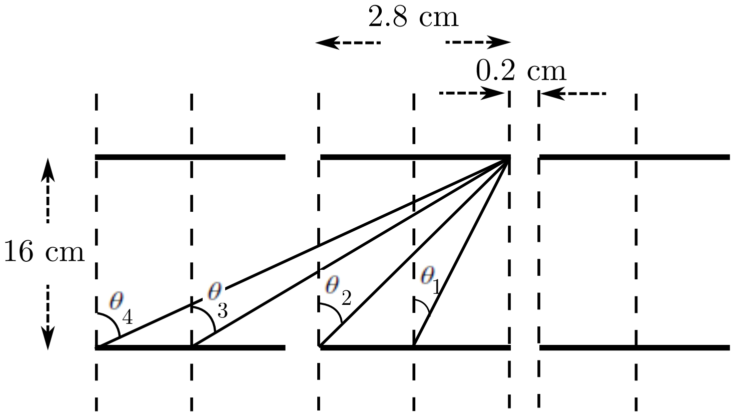

Figure 3.13. Geometry of the RPC strips.

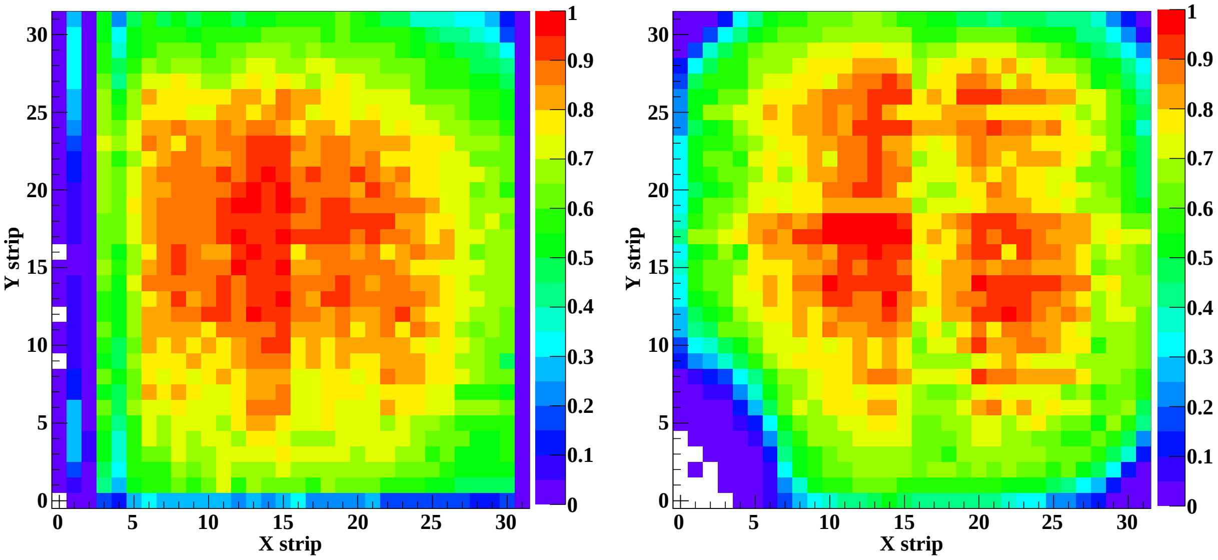

(a) Data (b) Data

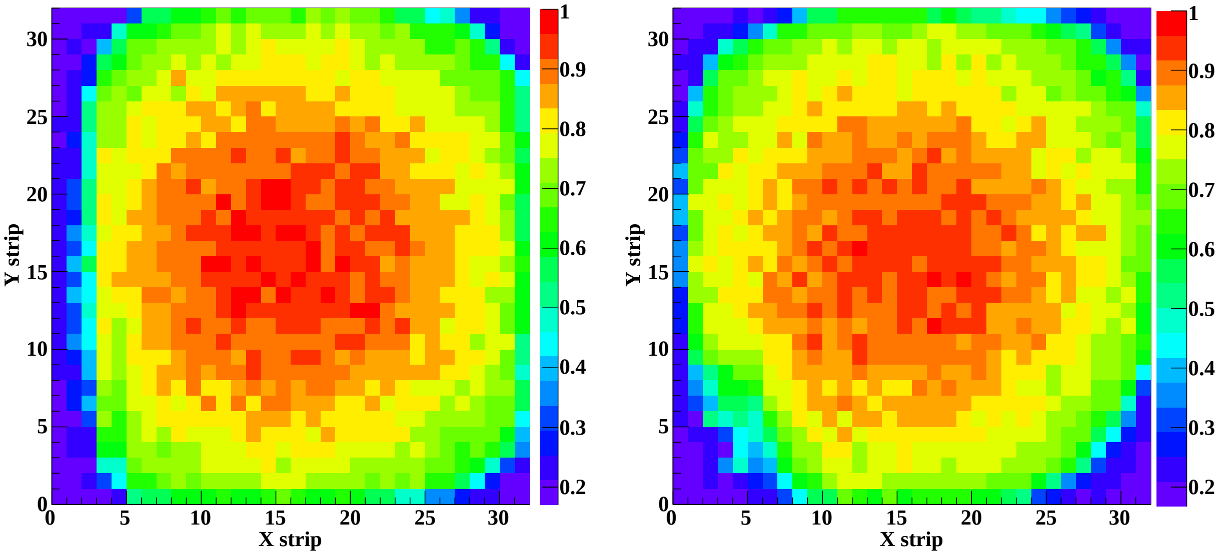

(c) MC (d) MC

Figure 3.14. Comparison of hit distributions between data and MC for top and bottom trigger layers.

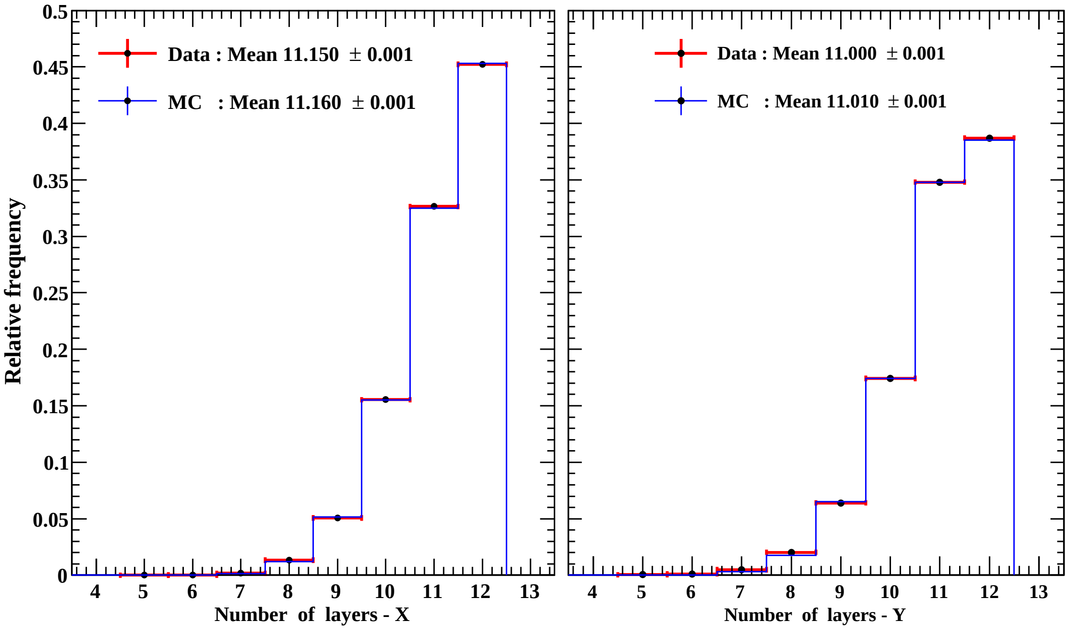

Figure 3.15. Distribution of the number of used layers in the track fit in data and MC. The distributions are scaled over their respective area.

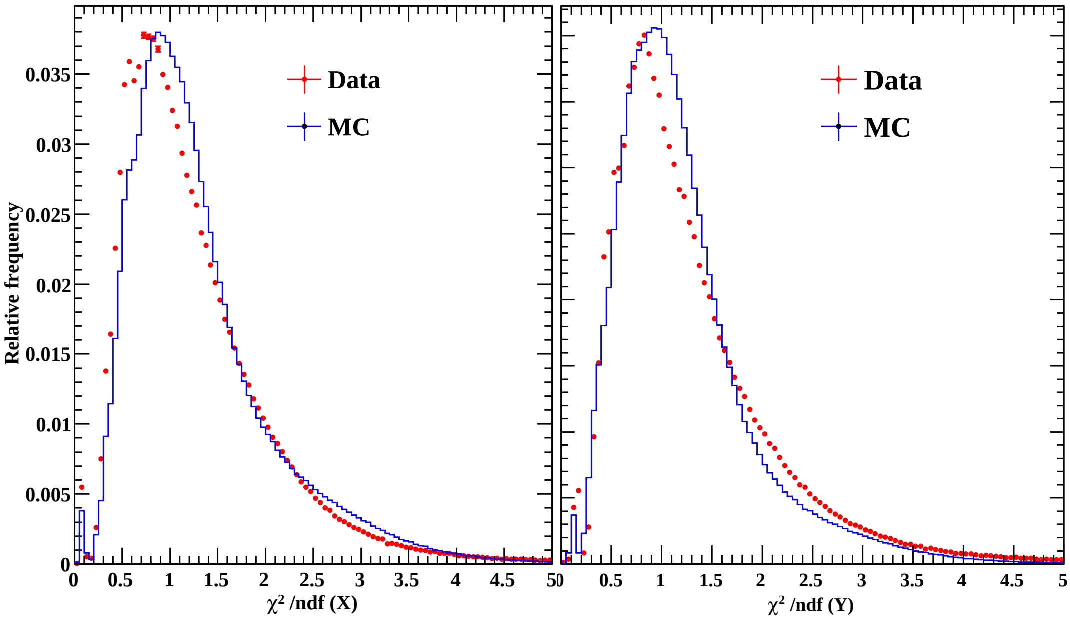

Figure 3.16. Reduced χ^2 distribution of track fitting of the X-view (left) and Y-view (right). The distributions are scaled over their respective area.

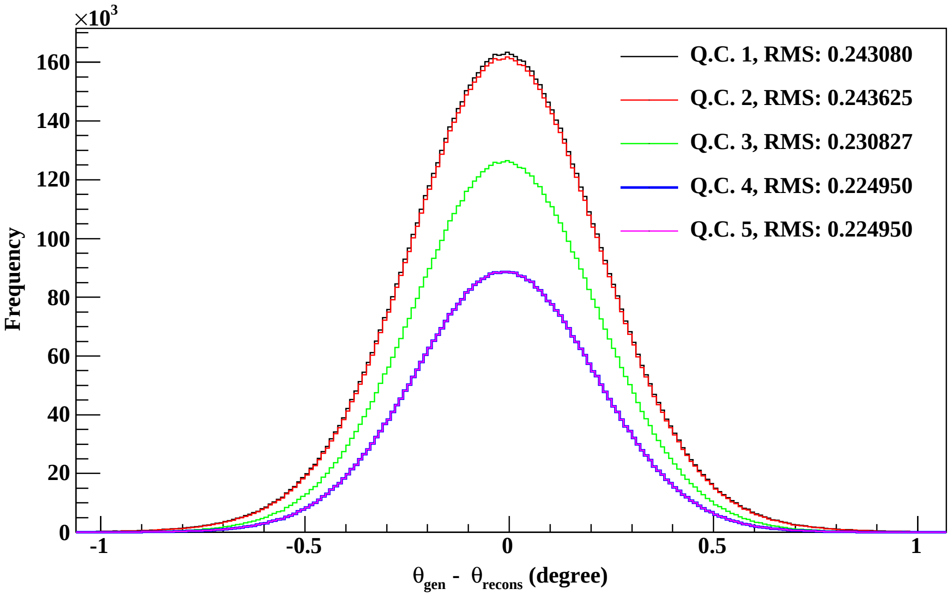

Figure 3.17. Difference between generated and reconstructed θ_s for different quality criteria as described in Section 3.1.10 for the observed zenith angle distribution (Figure 3.11).

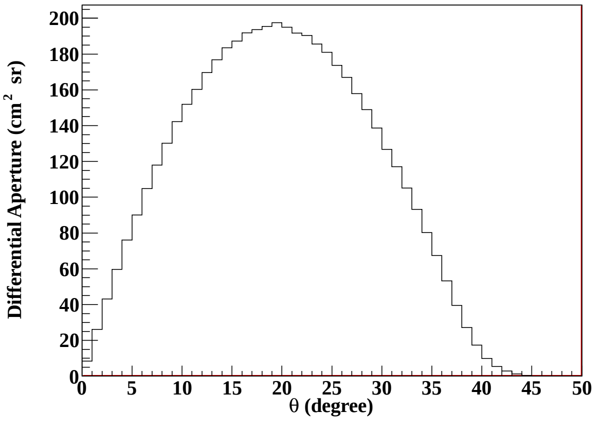

Figure 3.18. Differential aperture of the prototype stack.

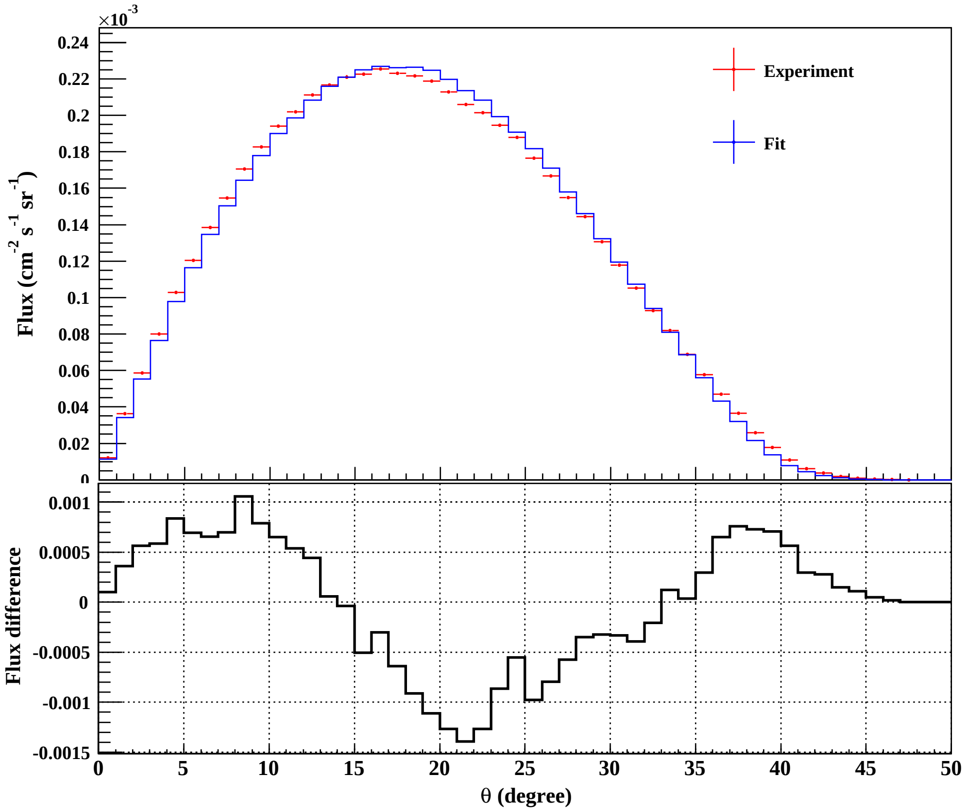

Figure 3.19. The normalised observed muon flux distribution along with the fitted distribution. Difference between the observed flux and the fitted value is also shown below.

4

A brief summary of cosmic muon flux measurement and comparison with the present result

Details of cosmic ray experiments over the last decade are explained vividly in ref. [126]. The primary cosmic radiation predominantly consists of protons, alpha-particles and heavier nuclei. While approaching towards the Earth, these particles are influenced by the galactic, the interplanetary, the magnetospheric and the geomagnetic magnetic fields. The cosmic ray flux is also modulated by solar activity. It manifests an 11 year cycle and for certain effects also a 22 year cycle, and other solar influences. Both cycles cause various effects on the galactic cosmic radiation in the heliosphere.

Primary cosmic radiation is subject to interact with electrons and nuclei of atoms and molecules that constitute the air while entering the atmosphere. The composition of the radiation changes as it propagates and all particles suffer energy losses through hadronic and/or electromagnetic processes. Incident hadrons are subject to strong interactions with air molecules, such as nitrogen and oxygen. Above an energy of few GeV mesons and other secondary particles are produced. The most abundant particles emerging from energetic hadronic collisions are pions, but kaons, hyperons, charmed particles and nucleon-antinucleon pairs are also produced. The majority of the heavy nuclei of the primary radiation are fragmented in the first interaction that occurs at a higher altitude than for protons, because of the much larger interaction cross section, $\sigma_i\,(\mathrm{cm}^2)$ and correspondingly shorter interaction mean free path, λ_i. The σ_i and λ_i are related as

$$\lambda_i = \frac{N_A}{A}\sigma_i\ (\mathrm{g\,cm^{-2}}) \tag{4.0.1}$$

So, there is practically no chance for a heavy nucleus to penetrate down to sea level. A hadron having an initial energy E_0, undergoing n interactions with a mean inelasticity, $< k >$, will retain on an average an energy, E, of

$$E = E_0\,(1- < k >)^n\,. \tag{4.0.2}$$

It is assumed that typically for a vertically incident high energy proton traversing the full atmosphere down to sea level $< k >= 0.5$ and $n = 12$ which gives

$$\frac{E}{E_0} = (0.5)^{12} \simeq 2.5 \times 10^{-4}. \tag{4.0.3}$$

This is known as leading particle effect, where incident nucleon or antinucleon retains on an average a relatively large fraction (~50%) of its initial energy when emerging from a collision than any of the secondary particles. For pions and kaons the leading particle effect is also observed but it is less pronounced. Meson initiated interactions are in general more inelastic than nucleon or antinucleon initiated interactions.

High energy strong interactions as well as electromagnetic processes, such as pair production, lead to the production of secondary particles.

Of all the secondaries (pions, kaons, hyperons, mesons etc.) pions are the most abundant. Unstable particles such as pions, kaons etc., decay. The competition between decay and interaction depends on the mean life and energy of the particles and on the density of the medium in which they propagate. For a given particle propagating in the atmosphere the respective probabilities for the two processes become a function of energy, altitude and zenith angle. Charged pions have a mean life at rest of 2.6×10^{-8} s and for neutral pions it is 8.4×10^{-17} s at rest. The interaction mean free path for charged pions is $\sim 120\,\mathrm{gcm^{-2}}$ in air. At high energies their mean life is significantly extended by time dilation. Mean life of muons coming from decay of pions are also short, $\sim 2.2 \times 10^{-6}$ s. Due to time dilation, a majority of these muons survives down to sea level. Decay probability (W) for an unstable particle in the vertical direction is given by,

$$W \simeq \frac{m_0 X}{\rho \tau_0 p}, \tag{4.0.4}$$

and in the inclined trajectories it is enhanced by the zenith angle factor,

$$W \simeq \frac{m_0 X sec\theta}{\rho \tau_0 p}, \tag{4.0.5}$$

where, m_0 (GeV/c^2) is the rest mass of the unstable particle, X ($\mathrm{g\,cm^{-2}}$) is the thickness traversed in the atmosphere, τ_0 (s) is the mean life of unstable particle at rest, ρ ($\mathrm{g\,cm^{-3}}$) is the density of the traversing medium, θ is the zenith angle and p (GeV/c) is the momentum of the particle. The decay probabilities for vertically downward propagating pions and kaons in the atmosphere at a depth of 100 $\mathrm{g\,cm^{-2}}$ as a function of kinetic energy are illustrated in the ref. [126] (Chapter 1, figure 1.5) which shows from 1 GeV to 10 GeV, $W = 1$ for both the particles, pions and kaons. After that W falls faster in case of pions than kaons. The survival probability ($S = 1 - W$) of muons coming from the decay of mesons is also given in the ref. [126] (Chapter 1, figure 1.6) for an atmospheric depth of 100 $\mathrm{g\,cm^{-2}}$, where it shows around 100 GeV, $S = 1$ and the curve falls almost exponentially towards lower energy and around 1 GeV, S is equal to 0.3.

At higher energies, mesons not only decay but also interact strongly with the nuclei that constitute the air. Thus, in the case of pions some decay into muons while others interact and, hence are losing energy. At constant density the competition changes in favour of interaction with increasing energy since time dilation reduces the probability for decay. This trend is amplified with increasing density. These effects give rise to a steepening of the muon spectrum relative to the pion spectrum above a certain energy. The differential energy spectrum of the muons ($j_\mu(E)$) and for pions ($j_\pi(E)$) are proportional to each other ($j_\mu(E) \propto j_\pi(E)$) in the energy range of 10 to 100 GeV and $j_\mu(E) \propto j_\pi(E)\left(\frac{1}{E}\right)$ for energy greater than 100 GeV which describes the steepening of the energy spectrum for muons compare to pions ref. [126] (Chapter 1, figure 1.7). Charged particles undergo variety of electromagnetic interactions with the medium in which they propagate that lead to energy losses. All known processes, ionisation and excitation, bremsstrahlung and pair production etc., happen depending on the energy of the projectile and its mass, and on the nature of the target.

Different observables are studied to characterise cosmic ray radiation. The directional intensity, $I_i(\theta, \phi)$ (cm$^{-2}\, s^{-1}\, sr^{-1}$), of particles of a given kind, i, is defined as the number of particles, dN_i, incident upon an element of area, dA, per unit time, dt, within an element of solid angle, $d\Omega$. The I_i also depends on the energy, E, and at low energy on the time, t. The directional intensity is simply termed as intensity. The vertical intensity is obtained for $\theta = 0^\circ$. The flux, J_1 (cm$^{-2}\, s^{-1}$), is defined as the integrated intensity over the solid angle for the upper hemisphere. The omnidirectional or integrated intensity, J_2, is obtained by integrating the $I_i(\theta, \phi)$ over all all angles. The zenith angle dependence of I_i is expressed as,

$$I_i(\theta) = I_i(0^\circ)\, cos^{n_i}\theta\,. \tag{4.0.6}$$

The exponent for the i-th component, n_i, depends on the atmosphere depth, X g cm^{-2}, and the energy, E, i.e., $n_i = n_i(X, E)$.

Primary cosmic ray fluxes and spectra has a east-west asymmetry up to energies of about 100 GeV, because of the geomagnetic field and the positive charge excess of the primary radiation. Due to the zenith angle dependence of the cosmic ray deep inside the atmosphere, which goes roughly as $cos^2\theta$, this asymmetry is less pronounced at sea level. There are other effects as well, such as azimuthal effect due to dipole shape of the geomagnetic field, latitude effect due to geomagnetic cutoff, longitude effect due to geomagnetic dipole axis is asymmetrically located with respect to the Earth's rotation axis.

Detail results of cosmic ray experiments carried out at altitudes higher than sea level, at sea level and also at the underground are described in ref. [126]. A brief discussion is reported here for cosmic rays at sea level.

Muon flux measurements up to 1973 had been summarised by Allkofer and Jokisch (1973). Based on the measurements by Greisen, Rossi (1948) derived the vertical differential flux for a muon momentum of 1 GeV/c. But measurements by Allkofer et al. during 1970 show about 26% higher flux than the estimated Rossi flux. A worldwide re-measurement of the muon fluxes thus had been initiated during 1970 to clarify this variation in the measurements. A complete set of vertical absolute integral fluxes of cosmic ray muons at or near sea level are given in Table 3.12 in [126]. A few of them are listed here in Table 4.1.

Table 4.1. Comparison of vertical integral fluxes of cosmic ray muons at sea level

Authors	Geomagnetic Latitude (°N)	P_c (GV)	Altitude (m)	Muon momentum (GeV/c)	Flux $\times 10^{-3}$ ($\mathrm{cm^{-2}s^{-1}sr^{-1}}$)
Allkofer et al.[127]	9	14.1	S.L.	$\geqslant 0.32$	7.25 ± 0.1
Karmakar et al. [128]	16	15.0	122	$\geqslant 0.353$ $\geqslant 1.0$	8.99 ± 0.05 6.85 ± 0.04
Sinha & Basu[129]	12	–	30	0.27	7.3 ± 0.2
Gokhale[130]	19	–	124	$\geqslant 0.32$	7.3 ± 0.1
Fukui et al.[131]	24	12.6	S.L.	$\geqslant 0.34$	7.35 ± 0.2
Present data	18	16	S.L.	$\geqslant 0.287$	6.217 ± 0.005
Rossi[132]	$\geqslant$50	~ 1.8	S.L.	$\geqslant 0.32$	8.3
Greisen[133–135]	54	1.5	S.L.	$\geqslant 0.33$	8.3 ± 0.1
Crookes & Rastin[136]	53	2.2	40	$\geqslant 0.35$	9.13 ± 0.12

Geomagnetic cut off rigidities (P_c) for cosmic rays vary with latitude and longitude. Variation along latitudes for a fixed longitude is seen more than the other way around. This is due to the Earth's magnetic field which varies with latitude and prohibits cosmic rays with rigidity below that is applicable to the corresponding magnetic field, entering the Earth's atmosphere. The P_c is lower at places away from the equator. That is why cosmic ray muon flux is expected to increase with latitudes as moving away from the equator. Results from [132]–[136] agree with this phenomenon.

At the lower latitudes, the observed muon flux is given in [127]–[131]. The result from [128] shows higher muon flux though the latitude and P_c are comparable with results from other lower latitudes. The present result is compared with [127], [129] and [131]; the P_c for the present site is slightly higher ($\sim$ 14–27%) than the other two ([127] and [131]). If only the P_c is considered then muon flux may appear to be little less than the other two places. The lower momentum cut off is similar for all four places. The present result shows $\sim 14 - 15\%$ less muon flux in the vertical direction than mentioned in [127] and [131]. The lower momentum cut off varies rapidly for low energy particles. For the present detector set up lower momentum cut off is also checked for most inclined particles and they do not differ much from the vertical direction.

4.1 Chapter summary

Present measurement of cosmic muon intensity in the vertical direction at sea level at lower latitude shows $\sim$14% deficit which could be due to geomagnetic cutoff. Detector efficiencies and other fluctuations are well considered here while estimating the differential aperture of the detector. If the tracking efficiencies at the corner region is decreased by 1%, n increases by 1% and I_0 decreases by 1.4%. The effect of misalignment of the detector if increased by 2 mm of Gaussian smearing, n decreases by 0.4% and I_0 decreases by 1%. Dead time is negligible in the VME DAQ system though this correction is taken into consideration while normalising the vertical flux. The effect of multiple scattering is not considered here since it is expected to be small and the data selection criteria automatically rejects any such tracks. All efficiencies/inefficiencies of the detector are well considered in the analysis. In the present set up higher zenith angle measurement is not possible as the set-up can not be rotated. If only few layers are put in trigger to observe higher zenith angle events, the fitting of those tracks is difficult due to the small number of hits.

This measurement was performed for a particular time. Variation of muon vertical intensity will be studied over a long period and at present this study is out of scope of this thesis.

5

Analysis of muon timing data and the directionality study

5.1 Data

Selected events after cosmic muon track fit are used for timing analysis (section 3.1.7). While in muon track reconstruction maximum three consecutive strip hits are considered, single strip multiplicity is considered for the time delay measurement and maximum two consecutive strip hits are taken in the directionality study. In this chapter, time delay measurements using an on-line and off-line methods, and the directionality study using corrected muon timing are discussed.

5.1.1 Measurement of the delay contributions of individual RPCs

Each stage of the electronic circuitry introduces its own delay which should be measured to get back the correct signal time. The first stage delay can be easily measured by knowing the muon hit position on the strip, whereas a particular effort is required to measure delays from stage 2 to stage 6 as shown in figure 2.2 in chapter 2.

5.1.2 Measurement with pulse generator

For preliminary studies, the calibrations were done using a pulse generator wherein a signal is simultaneously sent to two AFEs for two different layers among which one is the reference and the other is to be calibrated. A schematic of this calibration method is shown in figure 5.1. With this method the time delay of stages 3 to 6 (figure 2.2) is measured while the delays of the readout strips and pre-amplifiers are not taken into account. The delays from RPC strips to the pre-amplifiers as well as from pre-amplifiers to the AFE inputs are equalised for all the channels using equal lengths of interconnecting cables. The 0th layer is chosen as the reference to calibrate other layers and the 1st layer is chosen as the reference to calibrate time delays for the 0th layer. In particular, signal is given to the 31st strip of the reference layer.

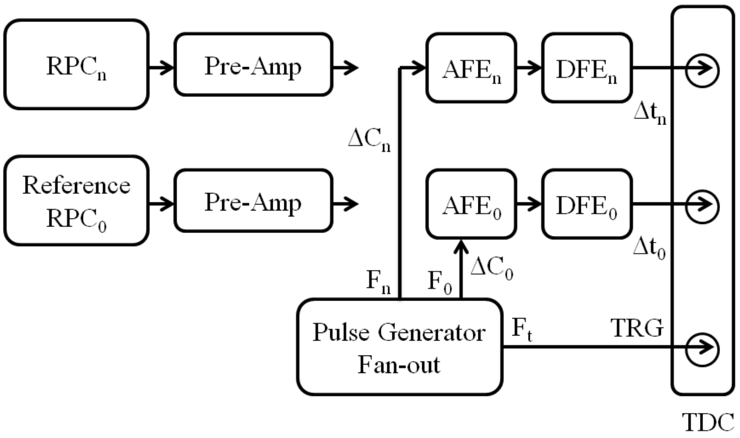

Figure 5.1. Schematic of the time delay measurement circuit. F's denote fan-out of the signal from pulse generator. Δt denotes the time delay from AFE to TDC and ΔC is the cable delay from pulse generator to the corresponding AFE input. Here the time delay of n^{th} layer with respect to the 0th layer is defined as $\Delta t_n - \Delta t_0$.

Three fan-out signals from the pulse generator are connected to their respective places; F_n to the calibrating layer, F_0 to the reference layer and F_t to trigger input of the TDC. If ΔC is the pulse propagation time from the pulse generator fan-out to AFE and and Δt is the pulse propagation time from AFE to the respective TDC channel, then the pulse propagation time difference between the reference layer and the calibrated layer, which is measured by the TDC, is given by,

$$\Delta t = \left(\Delta t_{cn} - \Delta t_{c0}\right) + \left(\Delta t_{n} - \Delta t_{0}\right). \tag{5.1.1}$$

To minimise systematic errors, the fan-out channels are swapped at the AFE input and the measurement is repeated. The time difference is now given by,

$$\Delta t_{swap} = \left(\Delta t_{c0} - \Delta t_{cn}\right) + \left(\Delta t_{n} - \Delta t_{0}\right). \tag{5.1.2}$$

The corrected time offset is thus given by,

$$\Delta t_{offset} = \Delta t_{n} - \Delta t_{0} = \left(\Delta t + \Delta t_{swap}\right)/2. \tag{5.1.3}$$

The strip-wise time delays were measured following this method. Using this method to calibrate the entire detector is cumbersome and time consuming. The results obtained from this measurement nonetheless give an idea of the order of magnitude of the delays. Figure 5.2a shows the total time delay contribution from stage 3 to stage 6 of the individual strips (X-view) for two RPCs in the stack. A pattern is seen among strips i, $i + 8$, $i + 16$ and $i + 24$ due to the fact that they are in wired-OR in the AFEs ('i' denotes here the strip number). The variation of time delay observed here between layer 0 and layer 8 is due to the particular choice of the reference layer. Figure 5.2b shows layer-wise time offsets between the 31st strip of the reference layer and the 31st strip of the calibrating layer for the X and Y-view.

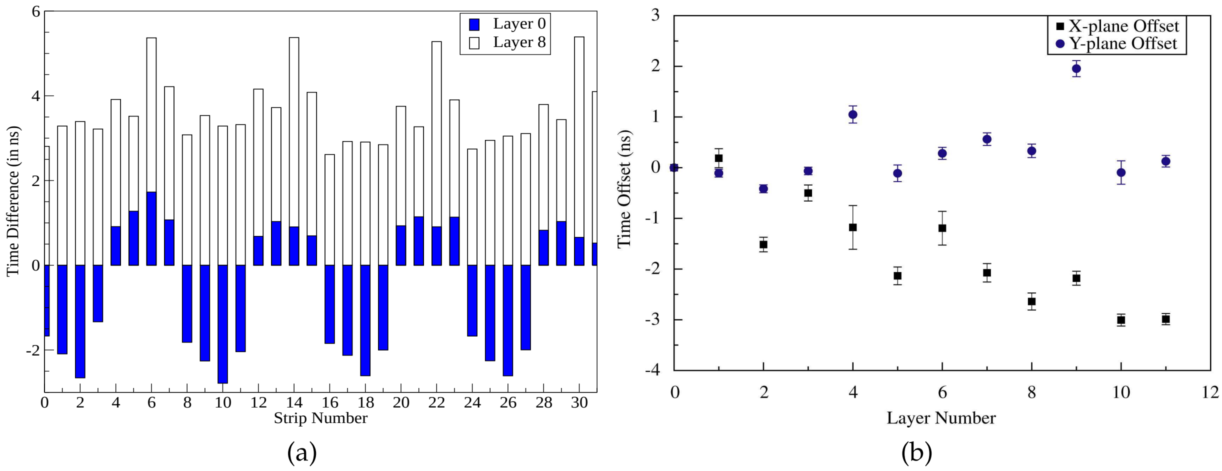

Figure 5.2. 5.2a shows time offsets for the strips of the 0^{th} and 8^{th} layer. 5.2b shows time offsets for all layers with respect to the 0^{th} layer for both the views.

5.1.3 Measurement with muon tracks

In view of the shortcomings seen in the method using the pulse generator, an alternative method is adopted using muon tracks as a source of timing calibration. The total time delay has been divided into two parts; the first comes from stage 1 (figure 2.2), which is due to the time delay in the RPC strips and the other part includes the time delays due to all electronics from stage 2 to 6. In order to measure the time delay in RPC strips, we consider events with single hit multiplicity and plot the time recorded in a particular RPC strip in the X-view against the Y coordinate of the firing strip in the Y-view. A linear fitting of time vs. hit here provides the time delay in the RPC strips which is found to be (4.8 ± 0.2) ns/m. An approximate value of 5 ns/m is considered in the following for the analysis. The raw TDC timing is first corrected by the time delay due to RPC strips and then used to determine the time delays from the stage 2 to 6 using this formula:

$$t_i = \delta + \frac{1}{c} l_i \tag{5.1.4}$$

where, t_i is the relative time of i^{th} layer with respect to the lowest layer with a valid hit and l_i is the corresponding cosmic muon track length. The only free parameter in this fitting, the intercept (δ) has to be estimated using the track length, timing information from other layers as shown in eq. 5.1.4. Initially, time offsets measurements were tried in a similar manner like layer residual measurements, where the calibrating layer is away and remaining selected layers are present in the fitting. But, in case of time fitting, similar approach does not provide converging results through iterative process of fitting. In case of muon track fitting, position uncertainty is less compared to the timing data. While doing linear fitting considering all selected layers, we implicitly assume timings of these layers have less uncertainty. So, difference between an extrapolated point in the calibrating layer and the raw timing provides the time delay for that particular strip. It is seen, after correcting these time offsets, measurement of time slope is diverged for a large number of iterations (more than 6). Therefore, in eq. 5.1.4, slope of the reference line is kept fixed and only the intercept is calculated.

Signals from all 32 strips for one side of a RPC are ORed in the AFE and DFE board which generate the final 1-Fold trigger signal for that layer (section 2.1.3, 2.1.4 in chapter 2). This time ORing for multi-hit layers introduces an uncertainty in the final time signal. To avoid this uncertainty, only layers having a single strip hit is considered. To avoid a bias in the determination of the time delays, the calibrating layer is excluded from the fitting and its time residual (Δt), the difference between the fitted time using other layers and the recorded time, is obtained. A constant time resolution (σ_{time}) equal to 1.6 ns is initially assumed in the fit. Timing data in any layer with $\Delta t > 3\sigma_{time}$ is excluded and another fit is performed. The probability to remove any data point after the second iteration is negligible ($< 10^{-5}$). This procedure is followed by excluding one layer at a time and the residuals for all 12 layers are estimated.

The strip wise residual distributions are later fitted with a Gaussian distribution and the mean value is considered as the time delay for a corresponding strip of a layer. RMS values of these distributions are later on used as time resolutions for every strip instead of having a fixed time resolution for all layers. Noisy channels[1] are neglected in this time delay calculation as well as for the directionality study (section 5.1.4). This entire process is repeated iteratively where residual distributions of time are corrected and updated for each strip of a layer in each iteration. After 4 – 5 iterations, no appreciable change is noticed in the mean and RMS of the time residual distributions. The fit parameters of the last iteration are considered for the following analysis. Typical corrections and resolutions for RPC strips as a function of the number of iterations are shown in figure 5.3.

5.1.4 The measurement of directionality

Selected events after cosmic muon track fit and applying all time offsets corrections are used for the directionality study. Moreover a strip hit multiplicity of at most 2 consecutive strips per layer is considered in this directionality measurement in order not to lose too much statistics[2]. Due to ORing of time signals in a layer, the earlier strip signal defines

---

[1] On an average, strip rate is 50 Hz. Noisy strips show higher count rates. To remove noisy strips, strip rate greater than 100 Hz are not used in this calculation. A strip is also neglected if the RMS of its Δt distribution is larger than 2 ns.

[2] The frequency of hit multiplicities is 48%, 34% and 16% for single, double and triple occurrence respectively, with an average hit value of 1.6.

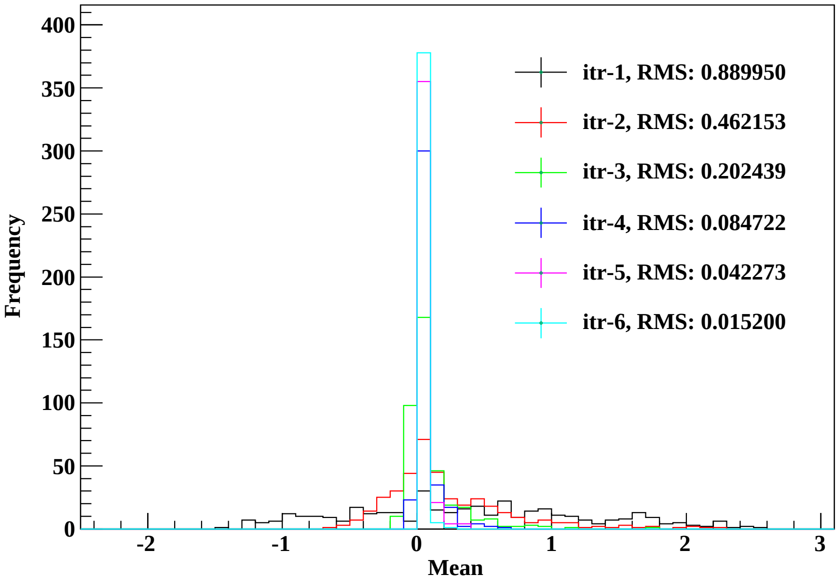

Figure 5.3. Variation of the mean of the strip wise time residual distributions with iteration number is shown for all X-view strips for all RPCs.

the timing. For this reason, the strip having smaller time offset is chosen for the strip time offset correction in case of double hit multiplicity. By doing so we implicitly assume that the true timing for both strips is the same. Following this procedure, three consecutive strip hits could also be considered but this was chosen not to be appropriate since the timing uncertainty would have increased.

Arrival times of muon tracks in each layer after the correction for the known delays are linearly fitted:

$$t_i = \delta' + m \times l_i \tag{5.1.5}$$

The δ' is different from the earlier mentioned δ in the sense that we have one free parameter in eq. 5.1.4 whereas, eq. 5.1.5 has two free parameters. X and Y-view time data are fitted separately. After time fitting, events are selected having at least two degrees of freedom ($\mathrm{ndf_t} = \mathrm{N_t} - 2 > 2$, N$_t$ being the number of layers used in the time fit) and by asking

$\chi^2_t/\mathrm{ndf}_t < 2$. All these selection cuts (track and time fit together) results in acceptance of about 50% of the total acquired events.

The time fit slope m multiplied by $(-1/c)$ is shown for the X-view in figure 5.4. It is evident from eq. 5.1.5, that the slope (m) is negative for down-going particles as $\mathrm{t_i} < \mathrm{t_0}$. Considering the RMS of the distribution (0.239 ns) and counting the number of events falling below zero (4.2 RMS units away from the peak), we see that 0.06% of the events are classified as up-going muons, which is assigned as the mis-identification rate of the muon direction.

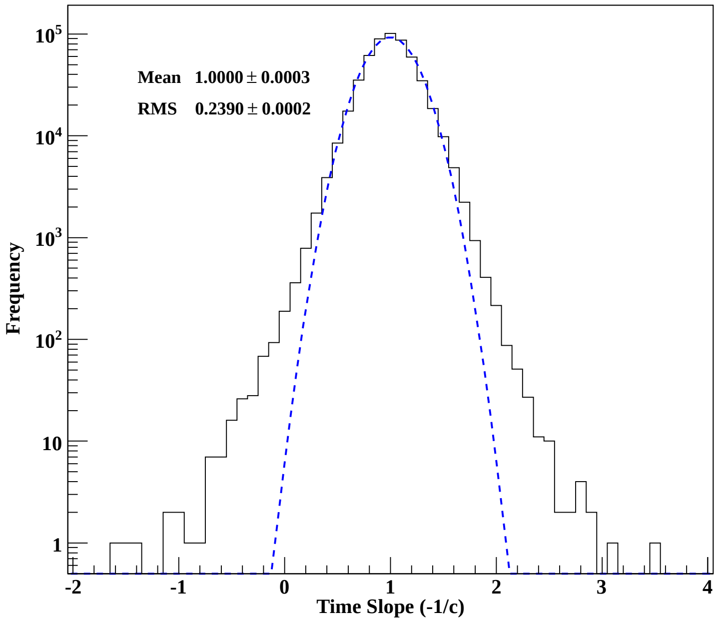

Figure 5.4. Time slope distribution for X-view with track and time fit event selection cut. Minimum N_t cut greater than 4 is chosen for time fit. Dotted line is the Gaussian fit to the data (solid line).

The distributions of the time slope multiplied by $(-1/c)$ are shown in figure 5.5 with different quality cuts on N_t. As the minimum acceptable N_t is increased we observe a decrease in the RMS as reported in Table 5.1. In this study, only the X-view timing data is shown and later on compared with a MC analysis. Y-view timing data is not simulated

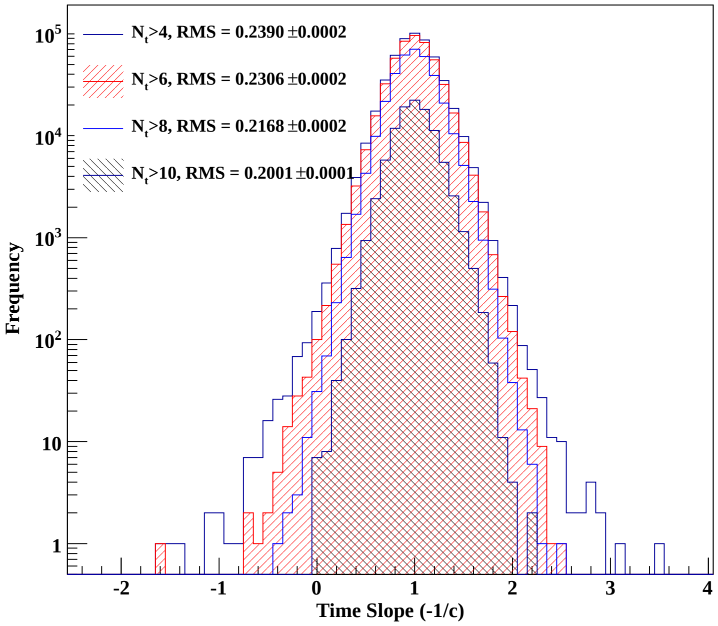

Figure 5.5. Overlay plot with different N$_t$ cuts of time slope for X-view is shown.

assuming its behaviour is the same as that of the X-view. There is no evident correlation between the time slope and zenith angle (θ) as shown in figure 5.6. But, a correlation is observed between the time slope and

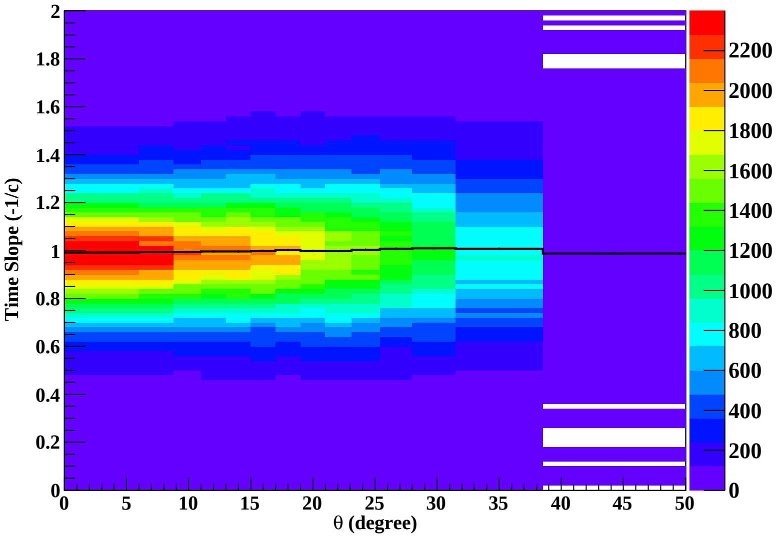

Figure 5.6. Correlation between the time slope and zenith angle (θ).

azimuthal angle (ϕ) as shown in figure 5.7.

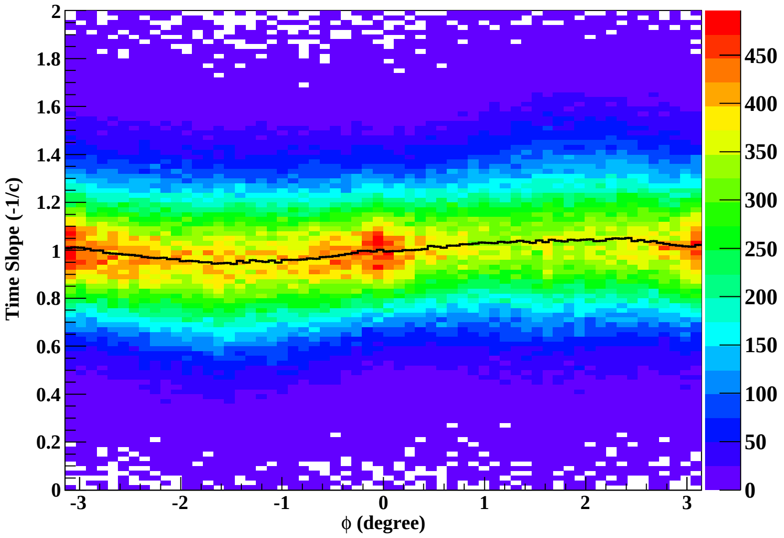

Figure 5.7. Correlation between the time slope and azimuthal angle (ϕ).

5.1.5 Timing correlation between layers

Timing correlation between layers are studied before applying time offsets correction. During the first iteration, considering all accepted layers time residual is used to calculate the time covariance matrix. Muon tracks are selected using same criteria as minimum number of layers N> 4 and $\chi^2/ndf < 2$. Single strip multiplicity events are considered in this analysis. Time residual greater than $3\sigma_{time}$, where $\sigma_{time} = 1.6$ ns, for any layer is neglected. The covariance matrix $M(12 \times 12)$ is defined as $M_{ij} = \frac{1}{N_{ij}} \sum_{n=1}^{N_{ij}} \Delta t_i \times \Delta t_j$, where $i,\ j = 0,\ 1,\ 2,\ \cdots,\ 11$ and N_{ij} is the number of accepted events for the ij^{th} element. After the normalisation,

$$M_{ij} = M_{ij}/\sqrt{M_{ii} \times M_{jj}}$$

it is given by,

$M(12 \times 12)$ =

$$\begin{pmatrix}
1 & -0.16 & -0.279 & -0.479 & -0.241 & -0.193 & -0.135 & -0.039 & 0.01 & 0.201 & 0.286 & 0.247 \\
-0.16 & 1 & -0.108 & -0.413 & -0.192 & -0.149 & -0.059 & 0.014 & 0.053 & 0.176 & 0.277 & 0.208 \\
-0.279 & -0.108 & 1 & -0.1 & -0.172 & -0.141 & -0.065 & 0.002 & 0.01 & 0.122 & 0.211 & 0.094 \\
-0.479 & -0.413 & -0.1 & 1 & -0.229 & -0.201 & -0.112 & -0.089 & -0.028 & 0.012 & 0.1 & 0.047 \\
-0.241 & -0.192 & -0.172 & -0.229 & 1 & -0.234 & -0.201 & -0.134 & -0.023 & -0.038 & 0.013 & 0.06 \\
-0.193 & -0.149 & -0.141 & -0.201 & -0.234 & 1 & -0.079 & -0.201 & -0.03 & -0.118 & -0.093 & -0.056 \\
-0.135 & -0.059 & -0.065 & -0.112 & -0.201 & -0.079 & 1 & -0.063 & -0.032 & -0.195 & -0.172 & -0.18 \\
-0.039 & 0.014 & 0.002 & -0.089 & -0.134 & -0.201 & -0.063 & 1 & -0.013 & -0.336 & -0.297 & -0.237 \\
0.01 & 0.053 & 0.01 & -0.028 & -0.023 & -0.03 & -0.032 & -0.013 & 1 & -0.127 & -0.206 & -0.054 \\
0.201 & 0.176 & 0.122 & 0.012 & -0.038 & -0.118 & -0.195 & -0.336 & -0.127 & 1 & -0.402 & -0.437 \\
0.286 & 0.277 & 0.211 & 0.1 & 0.013 & -0.093 & -0.172 & -0.297 & -0.206 & -0.402 & 1 & -0.168 \\
0.247 & 0.208 & 0.094 & 0.047 & 0.06 & -0.056 & -0.18 & -0.237 & -0.054 & -0.437 & -0.168 & 1
\end{pmatrix}$$

The reason for this observed correlation within nearby layers are unknown and yet to be studied.

5.2 MC

The result on the directionality misidentification is verified through a MC simulation. The hit positions in the MC are smeared (in terms of position and timing) according to the resolutions observed in real data. The track fitting and analysis of simulated data are carried out using the same procedure applied to real data.

5.2.1 Generation of muon timings

First muon tracks are simulated as described in chapter 3.2. The simulated zenith angle is generated following observed muon flux distribution ($dN/d\theta_s \propto cos^{2.15}\theta_s$). Similar selection criteria, used in the data, are used to select fitted tracks for the time analysis.

Timing for layers are generated assuming propagation with the speed of light and assigning the zero of time when the track crosses the lowest layer with valid hit for the directionality measurement. These generated timings data are then smeared followed by the strip-wise time residual distributions. Time residual in different layers are expected to be uncorrelated, but in real data a correlation of residuals among different layers is observed (section 5.1.5) and a covariance matrix is introduced. This covariance matrix is used to smear the muon timings in all layers. If no correlation between layers, the smearing of a data point towards positive or negative sides has equal probability. If there is a positive correlation then it is most probable timing of the next layer is shifted to the positive side and vice versa.

If any strip (X or Y-view) is rejected in the track fit that particular layer timing is neglected for further analysis. The different strip multiplicity criterion in the directionality study (maximum two consecutive strip hits instead of three are allowed) introduces an extra inefficiency. So, in addition to efficiency in position, a 2-D time efficiency map is also used to select a particular strip for timing measurement.

5.2.2 Time fitting results

Timing of selected simulated events are fitted with a straight line (like eq. 5.1.5, chapter 5) and the slope of the time fit multiplied by $(-1/c)$ is obtained. Event selection criteria is similar what is used in the data. The distribution of the number of selected layers used in the time slope fit (figure 5.8), the reduced χ^2 distributions for time fitting (figure 5.9) are shown for data and MC. There is an agreement between the time slope distributions of the data and MC (figure 5.10) though tails in the data are a little larger than in the MC.

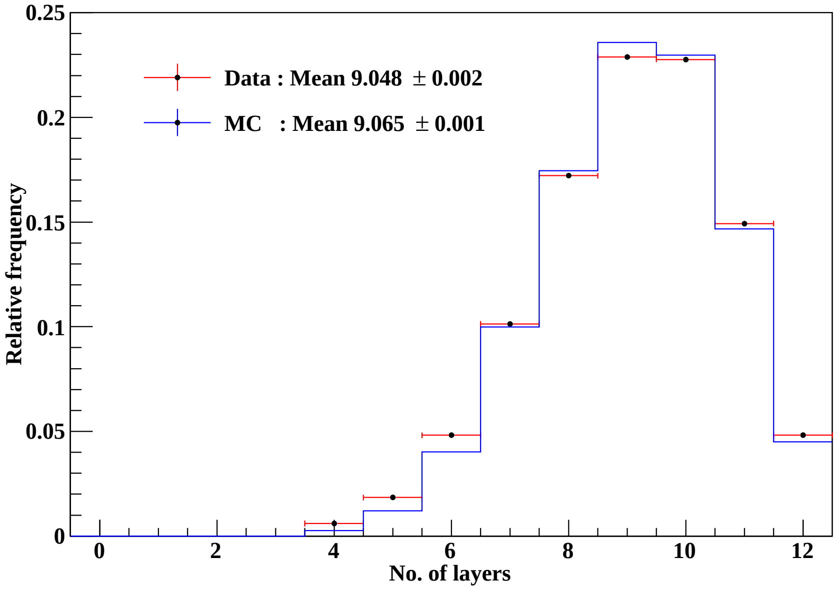

Figure 5.8. Distribution of the number of used layers for tracks used in the time fit in data and MC. The distributions are scaled over their respective area.

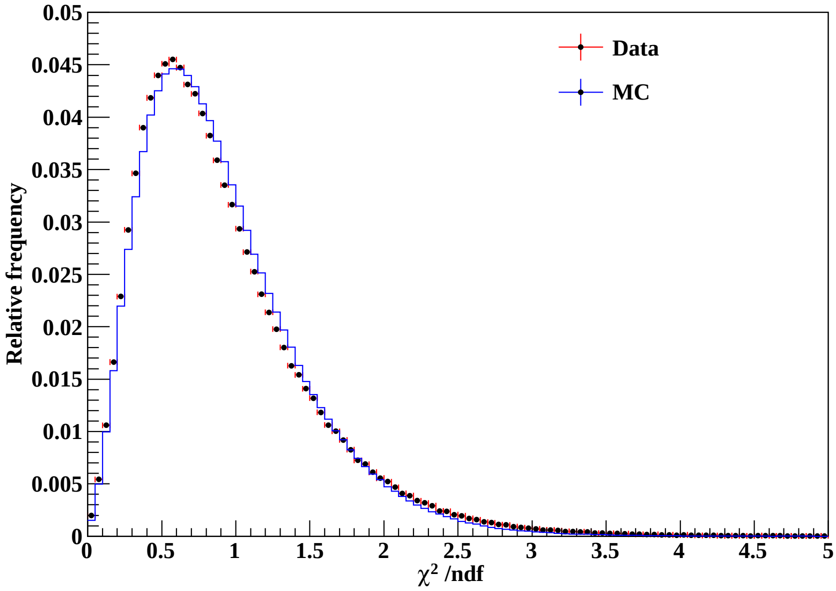

Figure 5.9. Reduced χ^2 distribution of time fitting (X-view). The distributions are scaled over their respective area.

A comparison of the results between data and MC with statistical errors is shown in Table 5.1. A reasonable agreement between data and MC is obtained. The mis-identification of muon direction (MisId) in the MC is lower

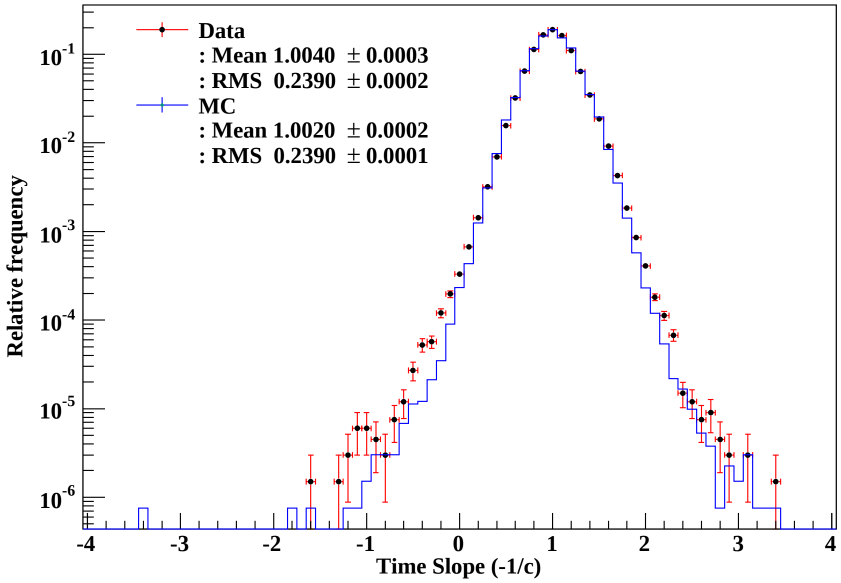

Figure 5.10. Time fit slope distribution of data and MC for $N_t > 4$. The distributions are normalised over their respective area.

Table 5.1. Comparison of the mis-identification of cosmic muon direction in data and MC. The mean values of the time slope distributions and the RMS with statistical errors are also given.

N_t	Data		MC		MisId $\left(\times 10^{-4}\right)$
	Mean	RMS	Mean	RMS	Data [MC]
> 4	1.0000 ± 0.0003	0.2390 ± 0.0002	1.0000 ± 0.0002	0.2408 ± 0.0001	6.21 ± 0.30 [2.17 ± 0.12]
> 6	1.0000 ± 0.0003	0.2306 ± 0.0002	1.0000 ± 0.0002	0.2330 ± 0.0001	2.74 ± 0.20 [2.07 ± 0.12]
> 8	1.0000 ± 0.0002	0.2168 ± 0.0002	1.0000 ± 0.0002	0.2210 ± 0.0001	0.88 ± 0.12 [0.67 ± 0.07]
> 10	1.0000 ± 0.0002	0.2001 ± 0.0001	1.0000 ± 0.0002	0.2050 ± 0.0001	0.18 ± 0.05 [0.08 ± 0.02]

than in the data as tails in the time slope distribution is not reproduced well enough in the MC.

5.3 Chapter summary

Time offset correction using pulse generator and using cosmic muon timings are discussed in this chapter. Offline algorithm for time offset correction using muon timings provides satisfactory results and it can be used in future for the main ICAL experiment. The proposed scheme of the electronics for the ICAL experiment is different from that used to read this prototype detector data. Each RPC in ICAL will have its own DAQ module integrated with it. Data from each RPC will be transferred to the back-end server on TCP/IP network. We foresee to perform the time calibration of the electronics at surface using this method. The time delays due to cables from each RPC module to the back-end will be separately calibrated. The muon directionality is verified by a MC simulation in the next chapter. Observed correlation among layer timings and also between the time slope and ϕ angle are still have to be studied. This is currently beyond the scope of this thesis.

The capability of the prototype detector in distinguishing between up-going and down-going particles has been studied. The tails in the directionality distribution can be explained from the timing fluctuations observed in the data. This has been verified through the use of a MC simulation though the magnitude of the effect is not completely reproduced by the MC. Using eight layers, the mis-identification of muon direction is about 9×10^{-5} (Table 5.1). We expect that in the INO experiment the mis-identification would be even lower due to the lower average muon momentum and the aid of the tracking in the magnetic field.

Part II

Physics simulation study

6

Formation of tau neutrinos in the atmospheric neutrino flux

6.1 Atmospheric neutrino flux

Atmospheric neutrinos are created by the interactions of primary cosmic rays with the nuclei in the atmosphere. Primary cosmic rays while propagating through the atmosphere produce many secondary cosmic rays, which include all the hadrons and their decay products, with an energy spectrum which has a peak in the GeV range and extends to higher energy with an approximate power law. In particular, many secondary pions are produced. Kaons are also produced at higher energies. These pions or kaons decay mainly into muons and muon neutrinos.

$$\pi^+ \to \mu^+ + \nu_\mu, \quad \pi^- \to \mu^- + \bar{\nu}_\mu \,. \tag{6.1.1}$$

These muons which decay before reaching the ground generate electrons, electron neutrinos, and muon neutrinos through the processes

$$\mu^+ \to e^+ + \nu_e + \bar{\nu}_\mu, \quad \mu^- \to e^- + \bar{\nu}_e + \nu_\mu \,. \tag{6.1.2}$$

These neutrinos generated in these interactions are called atmospheric neutrinos. These neutrinos have energies from about 100 MeV to about 100 GeV, and can be detected in underground laboratories through scattering on nuclei, electrons, etc. The neutrino fluxes (Φ) at low energies ($\lesssim 1$ GeV) satisfy the following ratios

$$\frac{\Phi_{\nu_\mu} + \Phi_{\bar{\nu}_\mu}}{\Phi_{\nu_e} + \Phi_{\bar{\nu}_e}} \simeq 2, \quad \frac{\Phi_{\nu_\mu}}{\Phi_{\bar{\nu}_\mu}} \simeq 1, \quad \frac{\Phi_{\nu_e}}{\Phi_{\bar{\nu}_e}} \simeq \frac{\Phi_{\mu^+}}{\Phi_{\mu^-}} \,. \tag{6.1.3}$$

At higher energies ($\gtrsim$ 1 GeV) the fraction of muons which hit the ground before decaying increases, leading to an increase of the flavour ratio of muon-type neutrinos to electron-type neutrinos.

The atmospheric neutrino fluxes used here have been taken from the model by Honda et al; details can be found in references [137] and [138]. Neutrino fluxes are computed using a 3D-scheme considering various interaction models, such as JAM, which is used in PHITS (Particle and Heavy-Ion Transport code System) [141] and DPMJET-III [142]. Using this code, atmospheric muon fluxes at high energy is computed and compared with the observed fluxes at sea level and mountain altitudes. Initial observed deficiencies in the calculated spectra are corrected using the "modified DPMJET-III", so that it reproduces observed atmospheric muon spectra with better accuracy at high momenta ($\gtrsim$ 30 GeV/c), and used in the calculation of the atmospheric neutrino fluxes [139]. The HARP experiment has greatly improved our knowledge of the hadronic interaction at low energies [143]. The JAM interaction model agrees a little better than the DPMJET-III with the HARP experiment.

The scheme for calculating the atmospheric neutrino fluxes is given in references [139, 140]. The Cartesian coordinate system is used for the 3D calculation of the atmospheric neutrino fluxes, where the origin is chosen at the center of the Earth with the Z-axis extending to the north pole, and the surface of the Earth is taken as a sphere with a radius of $R_e = 6378.18$ km. For the sake of mathematical simplicity, any position on the Earth is represented by the spherical polar coordinate system (r, θ, ϕ) with $r = R_e$, related to the Cartesian coordinate system by

$$\begin{aligned} x &= R_e \sin\theta \cos\phi \\ y &= R_e \sin\theta \sin\phi \\ z &= R_e \cos\theta \end{aligned} \tag{6.1.4}$$

The local coordinate system at the detector is constructed based on this polar coordinate system. The direction of the X-axis is in the increasing direction of θ, the direction of the Y-axis is in the increasing direction of ϕ, and the direction of the Z-axis is in the increasing direction of r. Therefore, the azimuth angle is measured south in the local coordinate system. In addition to the surface of the Earth, three more spheres, the injection sphere, the simulation sphere and the escape sphere, are considered for calculation. The radius of the injection sphere as $R_{injc} = R_e + 100$ km, and the radius of the other two spheres are considered as $10 \times R_e$ to increase computation power.

Cosmic rays are sampled on the injection sphere uniformly toward the inward direction, following the given primary cosmic ray spectra. Before they are fed to the simulation code for the propagation in air, they are tested to determine whether they pass the rigidity cutoff, i.e., the geo-magnetic barrier. Neutrino detectors are very small compared to the dimension of the Earth, and are considered as infinitesimal points on the surface of the Earth. But a finite size detector is required to compute the 3D neutrino fluxes. The finite size of the virtual detector introduces an error, since it averages the neutrino flux over positions where the geomagnetic conditions are different from the position of target detector. Error due to this virtual detector, named as "virtual detector correction", has been discussed in [139].

The neutrino flux computed for the Kamioka site (SuperK flux) is considered by the INO collaboration for various physics analysis. Flux data at the INO site is also available but still some upgrade work (mainly improvement in the sub-GeV energy region) is in progress. A comparison between SuperK and preliminary INO flux is shown in figure 6.1a, where sum of averaged neutrino flux over all directions are plotted. Beyond 3 GeV there is no appreciable change between two fluxes where significant change is observed in the lower energy region (< 1 GeV) due to mainly latitude effects. The input consists of ν_μ , $\bar{\nu}_\mu$, ν_e and $\bar{\nu}_e$ spectra distributed over E_ν, $\cos\theta$ and ϕ, where θ is the zenith angle, ϕ is the azimuth angle and E_ν is the energy of the incoming neutrino. The energy range for E_ν is from 0.1 GeV to 10 TeV as given in the Honda flux [137]. The flux is falling as $E_\nu^{-2.7}$.

Notice that there are no primary cosmic ray interactions that produce tau-neutrinos. They are produced due to oscillations of the other two flavours and hence are a good signal for neutrino oscillations. Tau-neutrinos are best detected in charge-current interactions with the subsequent production of the charged tau. The τ production from ν_τ has a threshold of function $E_\nu \gtrsim 3.5$ GeV due to the large tau mass. The neutrino fluxes are symmetric about $\cos\theta$ for such energies ($E_\nu > 3.2$ GeV) between the up- and down-going directions where $\cos\theta = -1$ refers to the up-going neutrinos (see Figure 6.1b).

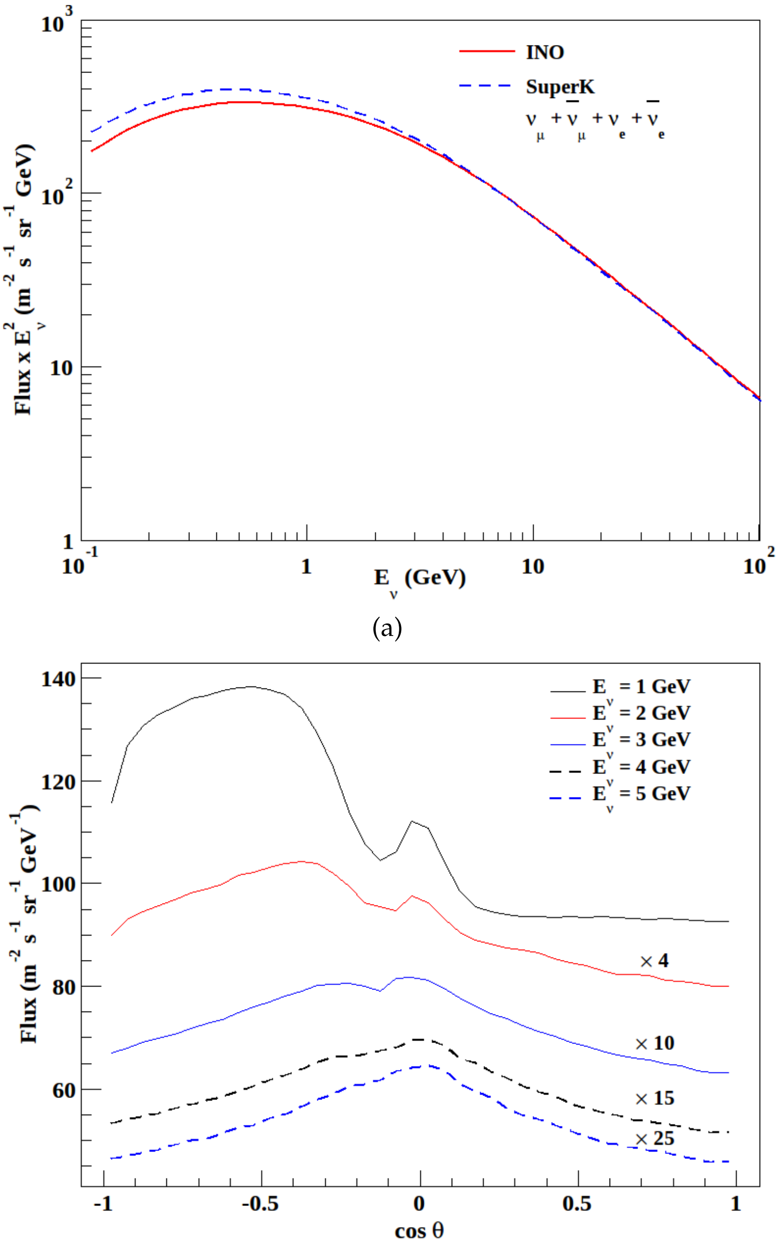

(a)

(b)

Figure 6.1. 6.1a shows sum of averaged atmospheric neutrino flux over all directions. 6.1b shows ν_μ flux variation over $\cos\theta$ for different sets of E_ν, where fluxes from and above 2 GeV are multiplied with a constant factor for the comparison plot. Similar behaviour is also observed in other neutrino flavours.

6.2 Neutrino oscillations

Neutrino oscillation is a quantum mechanical phenomenon proposed in the late 1950s by Pontecorvo [50] in analogy with K^0–$\bar{K}^0$ oscillations. The oscillations are generated by the interference of different massive neutrinos, which are produced and detected coherently because of their very small mass differences. In 1962 Maki, Nakagawa, Sakata [52] considered for the first time a model with the mixing of different neutrino flavours.

Later on, the standard theory of neutrino oscillations in the plane-wave approximation was developed in 1975-76 by Eliezer and Swift [54], Fritzsch and Minkowski [55], Bilenky and Pontecorvo [56], and then reviewed by Bilenky and Pontecorvo in ref. [57]. We summarise the relevant results below.

In a three neutrino framework, the neutrino flavour states $|\nu_\alpha\rangle$, $\alpha = e,\, \mu,\, \tau$, are defined as linear superpositions of the neutrino mass eigenstates $|\nu_i\rangle$, $i = 1,\, 2,\, 3$, with masses m_i:

$$|\nu_\alpha\rangle = \sum_i U_{\alpha i} |\nu_i\rangle \,. \tag{6.2.1}$$

The $|\nu_\alpha\rangle$ are the states produced in association with the charged leptons. The 3×3 unitary matrix U may be parametrised [52] (ignoring Majorana phases, which may be included by multiplying U by diagonal phases in addition to $\delta_{\rm CP}$) as

$$U = \begin{pmatrix} c_{12}c_{13} & s_{12}c_{13} & s_{13}e^{-i\delta_{\rm CP}} \\ -c_{23}s_{12} - s_{23}s_{13}c_{12}e^{i\delta_{\rm CP}} & c_{23}c_{12} - s_{23}s_{13}s_{12}e^{i\delta_{\rm CP}} & s_{23}c_{13} \\ s_{23}s_{12} - c_{23}s_{13}c_{12}e^{i\delta_{\rm CP}} & -s_{23}c_{12} - c_{23}s_{13}s_{12}e^{i\delta_{\rm CP}} & c_{23}c_{13} \end{pmatrix} \tag{6.2.2}$$

where, $c_{ij} = \cos\theta_{ij}$, $s_{ij} = \sin\theta_{ij}$, and $\delta_{\rm CP}$ denotes the CP violating (Dirac) phase. The 3×3 neutrino mass matrix M_ν^2 in the charged-lepton mass basis is diagonalised by U:

$$U^\dagger M_\nu^2 U = \mathrm{diag}(\mathrm{m}_1^2,\, \mathrm{m}_2^2,\, \mathrm{m}_3^2) \,. \tag{6.2.3}$$

The fundamental neutrino parameters therefore are the mixing angles θ_{ij}, phase $\delta_{\rm CP}$, and the mass-squared differences $\delta_{ij} \equiv m_i^2 - m_j^2$.

The time evolution of the mass eigenstates is governed by the Schrödinger equation,

$$|\nu_i(t)\rangle = e^{-iE_i t}|\nu_i(0)\rangle \,. \tag{6.2.4}$$

Consequently the time evolution of the flavour states is given by the equation,

$$i\frac{d}{dt}[\nu_\alpha] = \frac{1}{2E} U M_\nu^2 U^\dagger [\nu_\alpha] \,. \tag{6.2.5}$$

where $[\nu_\alpha]$ is the vector of flavour eigenstates, $[\nu_\alpha]^T = [|\nu_e\rangle,\, |\nu_\mu\rangle,\, |\nu_\tau\rangle]$.

The evolution equation in the presence of matter is given by

$$i\frac{d}{dt}[\nu_\alpha] = \frac{1}{2E}\left[UM_\nu^2U^\dagger + \begin{pmatrix} A & 0 & 0 \\ 0 & 0 & 0 \\ 0 & 0 & 0 \end{pmatrix}\right][\nu_\alpha], \tag{6.2.6}$$

where the matter term A (ignoring the diagonal neutral current contribution) is given by

$$\begin{aligned} A &= 2\sqrt{2}G_F n_e E \\ &= 7.63\times10^{-5}\ \mathrm{eV}^2\,\rho(\mathrm{gm/cc})\,\mathrm{E(GeV)}\,\mathrm{eV}^2\,. \end{aligned} \tag{6.2.7}$$

Here, G_F and n_e are the Fermi constant and electron number density in matter and ρ is the matter density. The evolution equation for anti-neutrinos has the sign of A and the phase δ_{CP} reversed.

In general, the 3-flavour probabilities, in particular, $P_{\mu\tau}$ and $P_{e\tau}$ of interest here, depend on all oscillation parameters: θ_{12}, θ_{23}, θ_{13}, δ_{21}, δ_{32}, and the CP phase δ_{CP}, as well as the density of Earth's matter.

Propagation of a flavour state over the time t from $|\nu_\alpha(0)\rangle$ to $|\nu_\alpha(t)\rangle$ and its projection on a flavour state $|\nu_\beta\rangle$ gives the oscillation probability amplitude and hence the oscillation probability $P_{\alpha\beta}\,(\nu_\alpha \to \nu_\beta)$; similarly, for the anti-neutrinos it is $P_{\bar{\alpha}\bar{\beta}}\,(\bar{\nu}_\alpha \to \bar{\nu}_\beta)$. The general expression for the $P_{\alpha\beta}$ is

$$P_{\alpha\beta} = \delta_{\alpha\beta} - 4\sum_{i<j}\mathrm{Re}(\square_{\alpha\beta\mathrm{ij}})\sin^2(\Delta_{\mathrm{ji}}) - 2\sum_{\mathrm{i<j}}\mathrm{Im}(\square_{\alpha\beta\mathrm{ij}})\sin(2\Delta_{\mathrm{ji}}) \tag{6.2.8}$$

The negative sign of the last term flips for the $P_{\bar{\alpha}\bar{\beta}}$. Here, $\square_{\alpha\beta ij} = U_{\alpha i}U_{\beta j}U^*_{\alpha j}U^*_{\beta i}$ and $\Delta_{ji} = (m_j^2 - m_i^2)/(4E)$.

For the atmospheric mass squared difference, it is convenient to introduce the scale Δm^2 instead of δ_{32}:

$$\Delta m^2 \equiv \delta_{32} + \delta_{21}/2 = m_3^2 - \frac{1}{2}(m_1^2 + m_2^2), \tag{6.2.9}$$

so that a normal or inverted hierarchy is simply indicated by a sign (and not magnitude) change in this parameter. This is an important probe of the sign of this mass-squared difference that is still not known.

Analytically, the effect of nonuniform matter poses a problem, while, in principle, the oscillation probabilities may be computed numerically to the requisite precision. A Runge-Kutta solver is used to calculate the oscillation probabilities for various energies and zenith angles. The density profile of the Earth is taken from the Preliminary Reference Earth Model (PREM) [144]. All results are obtained by numerically evolving the flavour eigenstates through Earth's matter. The matter density jumps at inner-outer core and core-mantle transitions and this affects oscillation probability as well. Details of the oscillation probabilities and its sensitivities to oscillation parameters are discussed in [145]. Current best fit oscillation parameters are given in Table 6.1 [146]. The oscillation probabilities $P_{\mu\tau}$ and $P_{e\tau}$ are shown in Figure 6.2 for different E_νs with $\cos\theta$.

Table 6.1. Currently accepted(/used) best-fit values of oscillation parameters [146].

Parameter	Best-fit value (3σ range)
$\sin^2\theta_{12}$	0.302 (0.267 –0.344)
θ_{12}	33.36° (31.09° –35.89°)
$\sin^2\theta_{23}$	0.5 (0.342 –0.667)
θ_{23}	45.0° (35.8° –54.8°)
$\sin^2\theta_{13}$	0.0257 (0.0156 –0.0299)
θ_{13}	9.217° (7.19° –9.96°)
$\delta_{\rm CP}$	0 (0 –2π)
δ_{12}	7.5 (7.0 –8.09) ($\times 10^{-5}$ eV^2)
$\lvert\Delta m^2\rvert$	2.4 (2.1 –2.6) ($\times 10^{-3}$ eV^2)

Atmospheric tau neutrinos, which are produced in the atmosphere (i.e., not from the oscillations), can be produced through the leptonic decay of D_s mesons produced in the interactions of the cosmic rays with air nuclei:

$$\begin{aligned} p(He) + A_{air} \rightarrow\ & D_s + X \\ & \hookrightarrow \tau + \nu_\tau \\ & \quad \hookrightarrow \nu_\tau + X' \end{aligned} \tag{6.2.10}$$

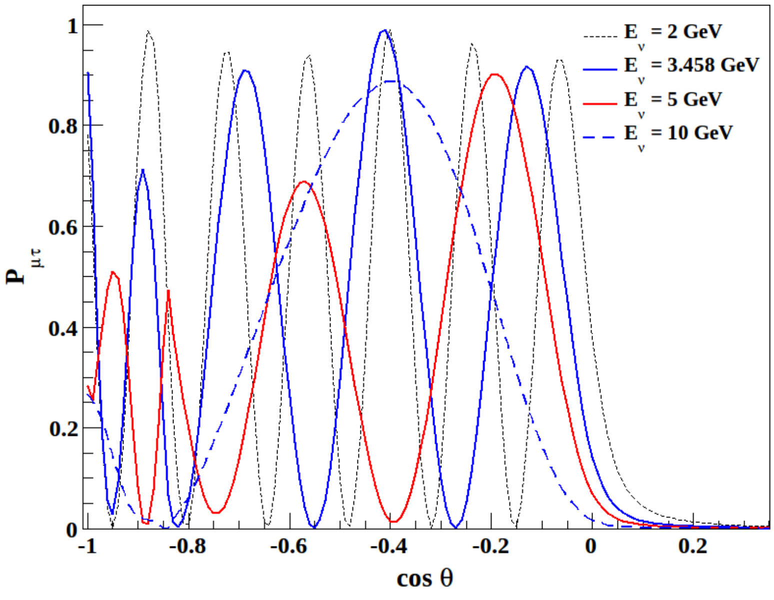

(a)

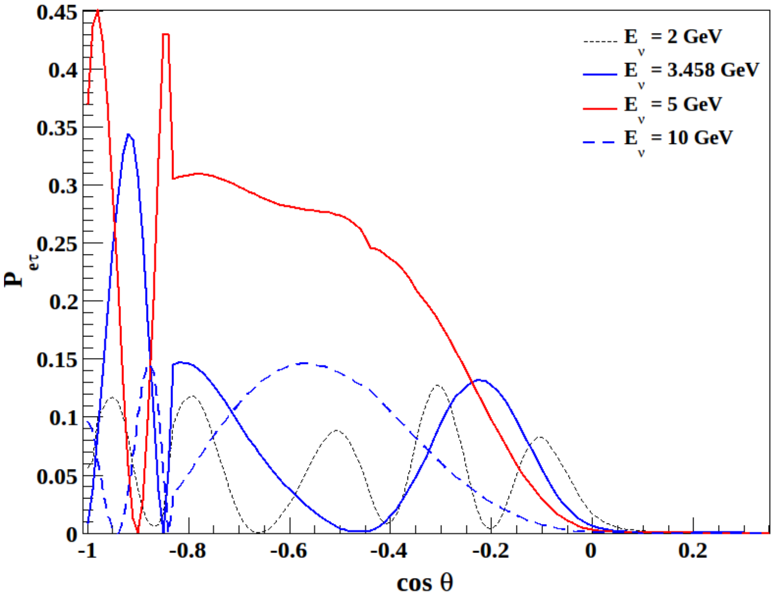

(b)

Figure 6.2. 6.2a shows oscillation probability, $P_{\mu\tau}$ and 6.2b shows $P_{e\tau}$. Notice the effect of core crossing at around $\cos\theta = -0.84$ which is especially visible when $E_\nu = 5$ GeV.

where X and X' are hadrons. The branching fraction of $D_s \rightarrow \tau + \nu_\tau$ is about 4% [147]. The flux of atmospheric tau neutrinos is estimated to be about 10^6 times lower than that of muon neutrinos and electron neutrinos [148], and is negligible for the atmospheric neutrino oscillations and the tau neutrino appearance analyses. That is, tau neutrinos, if they were to be observed by an atmospheric neutrino experiment, would come from atmospheric neutrino oscillations alone.

6.3 Chapter summary

A brief summary of unoscillated atmospheric neutrino fluxes is discussed in this chapter. SuperK flux is used so far by the INO collaboration for various analysis. Beyond $E_\nu \sim 3$ GeV relevant for the tau neutrino analysis, no significant difference between SuperK and preliminary INO flux is seen; furthermore, the fluxes are symmetric about $\cos\theta$.

A brief summary of neutrino oscillations is discussed here. Recent global fit results on the neutrino oscillation parameters are used here. PREM profile is used to consider Earth's matter profile. Instead of any analytic expression, numerical based analysis is adopted here to calculate neutrino oscillation probabilities by propagating neutrinos from the source point to the detector. The oscillations probabilities $P_{\mu\tau}$ and $P_{e\tau}$ (and analogous expressions for the anti-neutrino oscillations probabilities) are relevant in this analysis. Matter effect and recent results on θ_{13} enhances $P_{e\tau}$ channel as well. Sample oscillation probabilities for different neutrino energies are shown for the best-fit values of oscillation parameters as a function of zenith angle in Figure 6.2.

7 Neutrino-nucleon cross sections

Super-Kamiokande (SK) collaboration confirmed, from the study of the atmospheric neutrino flux, that oscillations from ν_μ into ν_τ [149] are nearly maximal, that is, $\theta_{23} \sim 45^\circ$. This has been confirmed by several beam-based neutrino oscillation experiments, such as ICARUS[150], MINOS[151], and OPERA[152] which are proposed and currently operating.

In all experiments, τ appearance is through CC tau-neutrino interactions off a nucleon target :

$$\nu_\tau(\bar{\nu}_\tau) \; + \; N \rightarrow \tau^-(\tau^+) \; + \; X, \tag{7.0.1}$$

with $N = p, \, n$.

Several authors have calculated the τ production cross section for nucleon targets [153–155]. In this thesis, cross section is taken from ref. [156]. Authors in ref. [156] have studied the spin polarisation of τ produced by ν_τ scattering off a nucleon target. Here, spin averaged double differential cross sections in the laboratory frame are considered. The quasi-elastic (QE) scattering, Δ resonance (RES) production and deep inelastic scattering (DIS) processes, which are known to give dominant contributions in the medium and high neutrino energy region [154], are considered in this analysis.

Firstly, we define the four-momenta in the laboratory frame for the process, $\nu_\tau(k) + N(p) \; \rightarrow \; \tau^-(k') \; + \; X(p')$, as k for incoming neutrino, p for target nucleon, k' for produced τ and p' for the net final state hadrons.

$$\begin{aligned} k^\mu &= (E_\nu, 0, 0, E_\nu), \\ p^\mu &= (M, 0, 0, 0), \\ k'^\mu &= (E_\tau, p_\tau \sin\theta, 0, p_\tau \cos\theta). \end{aligned} \tag{7.0.2}$$

Here, E_ν and E_τ are the incoming neutrino and outgoing τ energies, respectively, in the laboratory frame, M is the nucleon mass, and $p_\tau = \sqrt{E_\tau^2 - m_\tau^2}$ with the τ lepton mass $m_\tau = 1.78$ GeV. Since the only relevant angle for the cross-section is the charged-lepton–neutrino opening angle, the initial neutrino direction is chosen along the Z-axis for convenience and is suitably rotated later into the actual atmospheric neutrino direction. The other Lorentz invariant variables are,

$$\begin{aligned} Q^2 &= -q^2\,, \quad q^\mu = k^\mu - k'^\mu, \\ W_X^2 &= (p+q)^2. \end{aligned} \tag{7.0.3}$$

Q^2 is the magnitude of the momentum transfer and W_X is the hadronic invariant mass. The physical regions of these variables are given by,

$$\begin{aligned} M &\leqslant W \leqslant \sqrt{s} - m_\tau, \\ Q_-^2(W) &\leqslant Q^2 \leqslant Q_+^2(W), \end{aligned} \tag{7.0.4}$$

where $s = (k+p)^2$ and

$$Q_\pm^2(W) = \frac{s - M^2}{2}(1 \pm \bar{\beta}) - \frac{1}{2}\left[W^2 + m_\tau^2 - \frac{M^2}{s}(W^2 - m_\tau^2)\right] \tag{7.0.5}$$

with $\bar{\beta} = \lambda^{\frac{1}{2}}(1, m_\tau^2/s, W^2/s)$ and $\lambda(a,b,c) = a^2 + b^2 + c^2 - 2(ab + bc + ca)$. The scaling variables are defined as usual:

$$\begin{aligned} x &= \frac{Q^2}{2p \cdot q}\,, \\ y &= \frac{p \cdot q}{p \cdot k} = 1 - \frac{E_\tau}{E_\nu}. \end{aligned} \tag{7.0.6}$$

Here x is the Bjorken variable and y is the inelasticity. The physical regions for x and y are obtained by Albright and Jarlskog [157].

The relevant sub-processes are defined by using the hadronic invariant mass W_X and the momentum transfer Q^2.

$$\begin{aligned} \text{QE} &: W_X = M, \\ \text{RES} &: M + m_\pi < W < W_\text{cut}, \\ \text{IS} &: W_\text{cut} \leqslant W < \sqrt{s} - m_\pi. \end{aligned} \tag{7.0.7}$$

W_cut is an artificial boundary between RES and IS (inelastic scattering) processes, to avoid double counting. The W_cut is taken here as 1.4 GeV. Within the IS region, the region where $Q^2 \geqslant 1\ \text{GeV}^2$ may be labelled as DIS, where the use of the parton model can be justified.

Tensor at the lepton vertex for eq. 7.0.1 is defined as $L^{\mu\nu}$ and at the hadron vertex it is $W_{\mu\nu}$. The spin averaged amplitude square gives

$$L^{\mu\nu} = \text{Tr}\left[\gamma^\mu(1-\gamma^5)\not{k}\gamma^\nu(1-\gamma^5)\not{k}'\right] \tag{7.0.8}$$

and the hadronic tensor is expressed in general as

$$\begin{aligned} W_{\mu\nu}(p,q) = &-g_{\mu\nu}W_1(p\cdot q, Q^2) + \frac{p_\mu p_\nu}{M^2}W_2(p\cdot q, Q^2) - i\epsilon_{\mu\nu\alpha\beta}\frac{p^\alpha q^\beta}{2M^2}W_3(p\cdot q, Q^2) \\ &+ \frac{q_\mu q_\nu}{M^2}W_4(p\cdot q, Q^2) + \frac{p_\mu q_\nu + q_\mu p_\nu}{2M^2}W_5(p\cdot q, Q^2), \end{aligned} \tag{7.0.9}$$

where the totally anti-symmetric tensor $\epsilon_{\mu\nu\alpha\beta}$ is defined as $\epsilon_{0123} = 1$, and the structure functions $W_{i=1,\cdots,5}(p\cdot q, Q^2)$ can be estimated for each sub-processes. The structure functions W_4 and W_5 appear only in the heavy lepton production case [157]. The contraction of eq. 7.0.8 with eq. 7.0.9 and using eq. 7.0.2, the expression for the double differential cross section appears as

$$\begin{aligned} \frac{d\sigma}{dE_\tau\, d\cos\theta_\tau} = &\frac{G_F^2\kappa^2}{2\pi}\frac{p_\tau}{m_N}\Bigg[\left(2W_1 + \frac{m_\tau^2}{m_N^2}W_4\right)(E_\tau - p_\tau\cos\theta_\tau) + W_2(E_\tau + p_\tau\cos\theta_\tau) \\ &\pm\frac{W_3}{m_N}\left(E_\nu E_\tau + p_\tau^2 - (E_\nu + E_\tau)p_\tau\cos\theta_\tau\right) - \frac{m_\tau^2}{m_N}W_5\Bigg], \end{aligned} \tag{7.0.10}$$

where G_F is the Fermi constant, $\kappa = m_W^2/(Q^2 + m_W^2)$ is the propagator factor with the W-boson mass (m_W) and p_τ is the magnitude of the three-momentum of the charged lepton. The detailed expressions for $W_{\mu\nu}$ are taken from ref. [156] where specific structure functions are listed for QE ($W^{\rm QE}_{\mu\nu}$), Res ($W^{\rm RES}_{\mu\nu}$) and DIS ($W^{\rm DIS}_{\mu\nu}$) processes. Individual interaction processes are discussed in the following sections.

7.1 QE scattering

The CC QE scattering processes are,

$$\begin{aligned} \nu_\tau \ + n &\rightarrow \tau^- \ + p, \\ \bar{\nu}_\tau \ + p &\rightarrow \tau^+ \ + n\,. \end{aligned}$$

The hadronic tensor for these processes are written by using the weak transition current $J^\pm_\mu$ [158] as follows:

$$W^{\rm QE}_{\mu\nu} = \frac{cos^2\theta_c}{4}\sum_{\rm spins} J^\pm_\mu J^{\pm *}_\nu \delta(W^2_X - M^2), \tag{7.1.1}$$

where, θ_c is the Cabibbo angle. The weak transition currents J^+_μ and J^-_μ for the ν_τ and $\bar{\nu}_\tau$ scattering, respectively, are defined as

$$\begin{aligned} J^+_\mu &= \bar{u}_p(p')\Gamma_\mu(p',p)u_n(p), \\ J^-_\mu &= \bar{u}_n(p')\bar{\Gamma}_\mu(p',p)u_p(p)\,, \end{aligned} \tag{7.1.2}$$

where Γ_μ in written[1] in terms of six weak form factors of the nucleon, $F^V_{1,2,3}$, F_A, F^A_3 and F_p as,

$$\Gamma_\mu(p',p) = \gamma_\mu F^V_1(q^2) + \frac{i\sigma_{\mu\alpha}q^\alpha\xi}{2M}F^V_2(q^2) + \left[\gamma_\mu F_A(q^2) + \frac{q_\mu}{M}F_p(q^2)\right]\gamma_5\,. \tag{7.1.3}$$

The terms F^V_3 and F^A_3 are dropped due to time reversal invariance and isospin symmetry. Moreover, the vector form factor F^V_1 and F^V_2 are related to the electromagnetic

---

[1] $\bar{\Gamma}_\mu(p',p) = \gamma_0\Gamma^\dagger_\mu(p',p)\gamma_0$

form factors of nucleons under the conserved vector current hypothesis:

$$\begin{aligned} F_1^V(q^2) &= \frac{G_E^V(q^2) - \frac{q^2}{4M^2} G_M^V(q^2)}{1 - \frac{q^2}{4M^2}}, \\ \xi F_2^V(q^2) &= \frac{G_M^V(q^2) - G_E^V(q^2)}{1 - \frac{q^2}{4M^2}}, \end{aligned} \tag{7.1.4}$$

where,

$$G_E^V(q^2) = \frac{1}{\left(1 - \frac{q^2}{M_V^2}\right)^2}, \quad G_M^V(q^2) = \frac{1+\xi}{\left(1 - \frac{q^2}{M_V^2}\right)^2}, \tag{7.1.5}$$

with a vector mass $M_V = 0.84$ GeV and $\xi = \mu_p - \mu_n = 3.706$, where μ_p and μ_n are the anomalous magnetic moments of proton and neutron, respectively. For the axial vector form factor F_A, the following parametrisation is adopted:

$$F_A(q^2) = \frac{F_A(0)}{\left(1 - \frac{q^2}{M_A^2}\right)^2} \tag{7.1.6}$$

with an axial-vector mass $M_A = 1.0$ GeV and $F_A(0) = -1.23$ [158]. While the value of M_A has been extensively debated in the recent literature with reference to low energy results from KamLAND and MINOS, it is not important for tau production. Parametrisation for the pseudo-scalar form factor F_p [158] is

$$F_p(q^2) = 2M^2 \frac{F_A(q^2)}{m_\pi^2 - q^2} \tag{7.1.7}$$

with the pion mass $m_\pi = 0.14$ GeV. The normalisation of $F_p(0)$ is fixed by the partially conserved axial vector current (PCAC) hypothesis. The production cross-section and the polarisation of τ are sensitive to $F_p(q^2)$ because of the large τ mass and the spin-flip nature of the form factor.

The eq. 7.1.1 is transformed to the initial neutrino energy (E_ν) and tau energy (E_τ) variables:

$$\begin{aligned} W_{\mu\nu}^{\mathrm{QE}} &= \frac{\cos^2\theta_c}{2J_1}(p \cdot q) \sum_{\text{spins}} J_\mu^\pm J_\nu^{\pm *} \delta(E_\nu - E_\tau)\,. \\ &\equiv \Theta \sum_{\text{spins}} J_\mu^\pm J_\nu^{\pm *} \delta(E_\nu - E_\tau)\,. \end{aligned} \tag{7.1.8}$$

where the Jacobian factor (J_1) is

$$J_1 = 2\left|\frac{E_\nu E_\tau \cos\theta_\tau}{p_\tau} - (E_\nu + M)\right| . \tag{7.1.9}$$

Using eqs. 7.1.2, 7.1.3 and 7.1.8, the final forms of W_i^{QE} are obtained.

$$\begin{aligned}
W_1^{QE} &= \Theta\left((F_1^V + \xi F_2^V)^2 + F_A^2(1 + 2\frac{M^2}{p\cdot q})\right) , \\
W_2^{QE} &= \Theta\Big(2(F_1^V + \xi F_2^V)^2 + 2F_A^2 + 2(-\xi F_2^V)^2(1 + \frac{p\cdot q}{2M^2}) + 4(F_1^V + \xi F_2^V)(-\xi F_2^V)\Big)\frac{M^2}{p\cdot q} , \\
W_3^{QE} &= \Theta\left(-4(F_1^V + \xi F_2^V)F_A\right)\frac{M^2}{p\cdot q} , \\
W_4^{QE} &= \Theta\Big(\frac{1}{2}(-\xi F_2^V)^2(1 + \frac{p\cdot q}{2M^2}) + (F_1^V + \xi F_2^V)(-\xi F_2^V) + F_p^2(\frac{p\cdot q}{M^2}) - 2F_AF_p\Big)\frac{M^2}{p\cdot q} , \\
W_5^{QE} &= W_2^{QE}.
\end{aligned} \tag{7.1.10}$$

7.2 Resonance production

Resonance processes for the CC Δ production are

$$\begin{aligned}
\nu_\tau + n(p) &\to \tau^- + \Delta^+(\Delta^{++}), \\
\bar{\nu}_\tau + p(n) &\to \tau^+ + \Delta^0(\Delta^-) .
\end{aligned}$$

The N^* and the other higher resonance states are neglected due to their small contributions [154, 159, 160]. Detailed discussion about the calculation of $W_{\mu\nu}^{\mathrm{RES}}$ and its long expressions are given in ref. [156].

7.3 Deep Inelastic scattering

The CC DIS processes are given by,

$$\begin{aligned}
\nu_\tau + N &\to \tau^- + X, \\
\bar{\nu}_\tau + N &\to \tau^+ + X .
\end{aligned}$$

In the DIS region, the hadronic tensor is estimated by using the quark-parton model,

$$W_{\mu\nu}^{\mathrm{DIS}}(p,q) = \sum_{q,\bar{q}} \int \frac{d\xi}{\xi} f_{q,\bar{q}}(\xi,\, Q^2)\, K_{\mu\nu}^{(q,\bar{q})}(p_q, q). \tag{7.3.1}$$

Here, $p_q^\mu = \xi p^\mu$ is the four-momentum of the scattering quark, ξ is its momentum fraction, and f_q and $f_{\bar{q}}$ are the parton distribution function (PDF) inside a nucleon. The CTEQ6 LO set of parton distribution functions (leading order in the α_S) through the LHAPDF [161] (version 5.8.7) interface are used in the DIS process. The quark tensor is given in ref. [156] considering the spin average of initial quark and by summing over the final quark spins,

$$\begin{aligned} K_{\mu\nu}^{(q,\bar{q})}(p_q, q) &= \delta(2p_q \cdot q - Q^2 - m_{q'}^2) \\ &\times 2\left[-g_{\mu\nu}(p_q \cdot q) + 2p_{q\mu}p_{q\nu} \mp i\epsilon_{\mu\nu\alpha\beta}p_q^\alpha q^\beta + (p_{q\mu}q_\nu + q_\mu p_{q\nu})\right]. \end{aligned} \tag{7.3.2}$$

The upper sign should be taken for quarks and the lower for anti-quarks. The final quark mass ($m_{q'}$) is retained for the charm quark as $m_c = 1.5$ GeV, but otherwise it is set $m_{q'} = 0$. The charm and heavier-quark distributions in the nucleon are neglected, as well as bottom and top production cross-sections.

By neglecting the nucleon and initial quark masses consistently, the following relations are obtained,

$$W_1(p\cdot q, Q^2) = F_1(x, Q^2),\ W_{i=2,\cdots,5}(p\cdot q, Q^2) = \frac{M^2}{p\cdot q}F_{i=2,\cdots,5}(x, Q^2). \tag{7.3.3}$$

Here,

$$\begin{aligned} F_1 &= \sum_{q,\bar{q}} f_{q,\bar{q}}(\xi,\, Q^2), \\ F_2 &= 2\sum_{q,\bar{q}} \xi f_{q,\bar{q}}(\xi,\, Q^2), \\ F_3 &= 2(\sum_{q} f_q(\xi,\, Q^2) - \sum_{\bar{q}} f_{\bar{q}}(\xi,\, Q^2)), \\ F_4 &= 0, \\ F_5 &= 2\sum_{q,\bar{q}} f_{q,\bar{q}}(\xi,\, Q^2), \end{aligned} \tag{7.3.4}$$

where the momentum fraction is $\xi = x$ for massless final quarks ($m_{q'} = 0$), and $\xi = x/\lambda$ with $\lambda = Q^2/(Q^2 + m_{q'}^2)$ for $q' = c$. In the $m_c \to 0$ limit, the Callan-Gross relation $F_2 = 2xF_1$ and the Albright-Jarlskog relations $F_4 = 0$, $2xF_5 = F_2$ hold. To ensure the positivity constraints of eq. 7.0.10, the following modification of the W_1 structure function is done ([156]):

$$W_1 = \left(1 + \frac{\xi M^2}{p \cdot q}\right) F_1, \tag{7.3.5}$$

and it is mentioned in ref. [156] that the positivity is maintained when the charm quark mass is introduced by using the rescaling variable $\xi = x/\lambda$.

7.4 Kinematics of the process

The threshold for the interaction, eq. 7.0.1, is given by

$$E_\nu^{min} = m_\tau \left(1 + \frac{m_\tau}{2M}\right) = 3.458\text{GeV}\,. \tag{7.4.1}$$

In this interaction (eq. 7.0.1, 7.0.2), the available phase space is restricted for the tau production due to the constraint on the available energy for the lepton (E_l): $E_{\min} < E_l < E_{\max}$. The kinematic condition, $(p + q)^2 > M^2$, leads to a quadratic equation in E_τ, $(aE_\tau^2 + bE_\tau + c > 0)$ which sets bound on the E_l and the opening angle, θ_τ with respect to the initial neutrino (ν_τ) direction.

$$(p + q)^2 > M^2 \Rightarrow q^2 + 2p \cdot q > 0 \tag{7.4.2}$$

And this results in,

$$\begin{aligned} E_\tau^2 \Big(\cos\theta_\tau^2 - 1 - (M/E_\nu)^2 - 2(M/E_\nu) \Big) + E_\tau \Big(2M + M(m_\tau/E_\nu)^2 + 2M^2/E_\nu + m_\tau^2/E_\nu \Big) \\ + \Big(- m_\tau^2 \cos\theta_\tau^2 - M^2 - (m_\tau^2/4E_\nu)^2 - M m_\tau^2/E_\nu \Big) > 0 \end{aligned} \tag{7.4.3}$$

The real solution thus gives bound on θ_τ and the two roots of this equation sets limits on E_τ.

$$\cos\theta_\tau\big|_{\min} = \sqrt{1 + \frac{M^2}{E_\nu^2} + \frac{M}{E_\nu} - \frac{M^2}{m_\tau^2} - \frac{m_\tau^2}{4E_\nu^2}}\,,$$

$$E_{\tau\,(max,\,min)} = \frac{1}{2a}\left(b \pm \sqrt{b^2 - 4ac}\right)\,, \tag{7.4.4}$$

where,

$$\begin{aligned} a &= (E_\nu + m_N)^2 - (E_\nu\cos\theta_\tau)^2\,, \\ b &= (E_\nu + m_N)\left(2m_N E_\nu + m_\tau^2\right)\,, \\ c &= (m_\tau E_\nu\cos\theta_\tau)^2 + \left(m_N E_\nu + \frac{m_\tau^2}{2}\right)^2\,. \end{aligned} \tag{7.4.5}$$

Moreover, tau production is very much in the forward directions with respect to the incoming neutrinos and available phase space is also restricted by the kinematics. In the Figure 7.1, distribution of the final hadronic mass W_X, ($W_X^2 = (p+q)^2$), is plotted as a function of E_τ for a fixed energy of $E_\nu = 10$ GeV. It is visible from Figure 7.1 that the allowed tau energy limits for a given $\cos\theta_\tau$ correspond to the end points of the parabola in the W_X–E_τ plane. At minimum and maximum energy points, quasi-elastic behaviour of the interaction is also visible in Figure 7.1 as the lower limit of the W_X

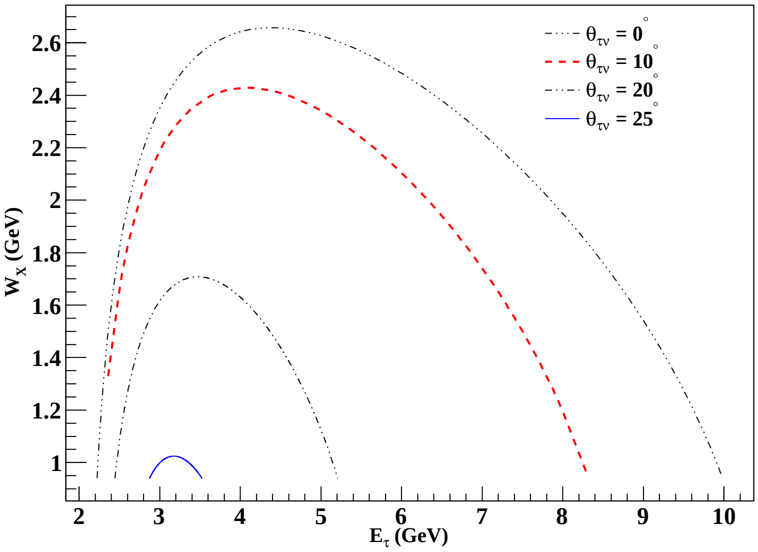

Figure 7.1. The invariant mass distributions for various opening angles for a fixed value of $E_\nu = 10$ GeV. Note that physically $W_X \geqslant m_N$, the nucleon mass.

corresponds to the nucleon mass.

7.5 Total cross section

The integrated cross-sections over the lepton energy and opening angle (eq. 7.0.10) with respect to the initial neutrino energy for the DIS and Res processes along with the QE case are shown in the Figure 7.2. It is found that at medium neutrino energies, the QE contribution dominates the total cross section near the threshold, and the sum of the QE and RES cross sections are significant throughout the neutrino energy range and thus important in any neutrino oscillation experiments. Significance of the QE and RES contribution is more pronounced for the $\bar{\nu}_\tau + N \to \tau^+ + X$ reaction as shown in the right panel of Figure 7.2, where the DIS contribution starts dominating the total cross section only above $E_\nu = 10$ GeV. Anti-neutrino nucleon cross-sections is one-third of the neutrino nucleon cross-sections (neglecting nucleon mass) as $(V - A)$ form of the current in the weak interaction distinguishes left handed and right handed particles. This deficit in cross-sections for anti-neutrinos is also visible in Figure 7.2.

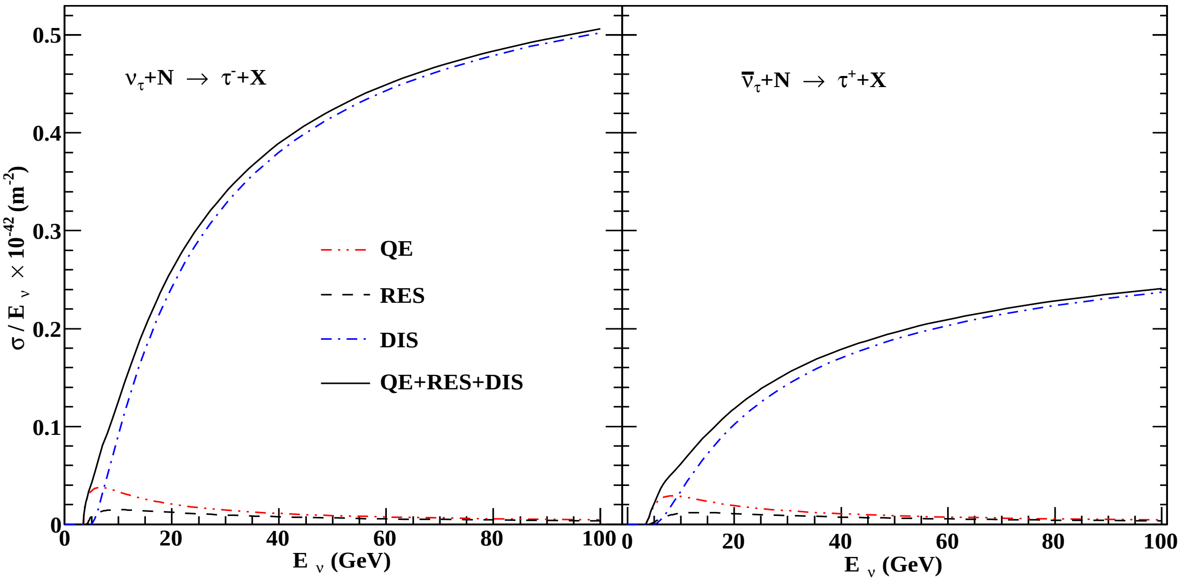

Figure 7.2. Total cross-sections for the individual processes (QE, Res and DIS) and all together are shown for neutrino (left panel) and anti-neutrino (right panel) interactions.

7.6 Chapter summary

The general formulation of the neutrino-nucleon cross-sections is discussed in this chapter. The general form of hadronic tensor is discussed where structure functions are taken from ref. [156]. DIS process contribution is the major part here.

8

The estimation of number of tau events in the ICAL detector

We are concerned here with CC tau interactions with the detector material. In the case of beam experiments, the direction of incoming neutrinos is chosen along the Z-axis, whereas atmospheric neutrinos are coming from all possible directions in the detector (while the initial flux is more or less isotropic at these energies, the tau neutrinos are produced through neutrino oscillations that are not so). In general, four-momenta of incoming neutrinos, target nucleon and outgoing tau-leptons in the laboratory frame are

$$\begin{aligned} k &= E_\nu(1,\, \sin\theta_\nu \cos\phi_\nu,\, \sin\theta_\nu \sin\phi_\nu,\, \cos\theta_\nu), \\ p &= (M,\, 0,\, 0,\, 0), \\ k' &= (E_\tau,\, |\vec{k}'| \sin\theta_\tau \cos\phi_\tau,\, |\vec{k}'| \sin\theta_\tau \sin\phi_\tau,\, |\vec{k}'| \cos\theta_\tau)\,. \end{aligned} \tag{8.0.1}$$

In this interaction, the recoil nucleus cannot be identified experimentally and is considered along with the hadronic debris. Hence, the interaction is simplified as one particle is coming in and two particles are going out (Figure 8.1), where the kinematics are confined in a plane. Now, as the initial neutrino does not have any transverse momentum, the transverse component of the final state momenta should also vanish. To rotate the lab frame in to the frame where the neutrino is along the Z-axis, first, the $\vec{k}$ is rotated by an angle ϕ_ν about the Z-axis and then by an angle $(-)\theta_\nu$ about the Y-axis:

$$\begin{pmatrix} \cos(-\theta_\nu) & 0 & \sin(-\theta_\nu) \\ 0 & 1 & 0 \\ -\sin(-\theta_\nu) & 0 & \cos(-\theta_\nu) \end{pmatrix} \begin{pmatrix} \cos\phi_\nu & \sin\phi_\nu & 0 \\ -\sin\phi_\nu & \cos\phi_\nu & 0 \\ 0 & 0 & 1 \end{pmatrix} \begin{pmatrix} \sin\theta_\nu \cos\phi_\nu \\ \sin\theta_\nu \sin\phi_\nu \\ \cos\theta_\nu \end{pmatrix} = \begin{pmatrix} 0 \\ 0 \\ 1 \end{pmatrix} \tag{8.0.2}$$

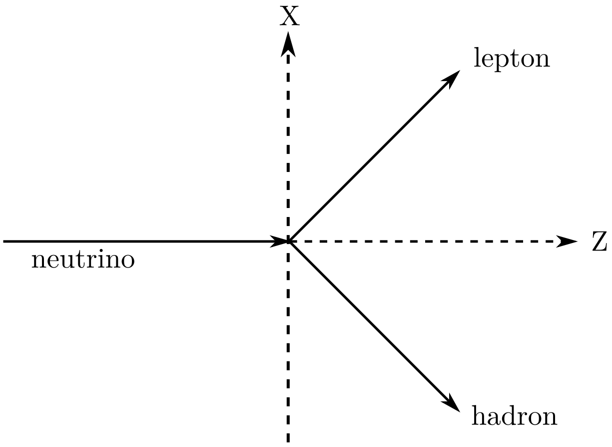

Figure 8.1. Schematic of the neutrino interaction in the laboratory frame.

Similar rotations are also applied to $\vec{k}'$ and it is labelled as $\vec{k}'_{rotated}$. In the $\nu - \tau$ frame, the $\vec{k}'$ is defined as

$$\vec{k}'_{\tau\nu} = |k'_{\tau\nu}| \,(\sin\theta_{\tau\nu}\cos\phi_{\tau\nu},\ \sin\theta_{\tau\nu}\sin\phi_{\tau\nu},\ \cos\theta_{\tau\nu}),$$

which is basically equivalent of $\vec{k}'_{rotated}$. The $\vec{k}'_{rotated} \equiv \vec{k}'_{\tau\nu}$ gives the following relations between the laboratory frame and the ν–τ frame.

$$\begin{aligned} \cos\theta_{\tau\nu} &= \sin\theta_\nu \sin\theta_\tau \cos(\phi_\tau - \phi_\nu) \ + \ \cos\theta_\nu\cos\theta_\tau \\ \tan\phi_{\tau\nu} &= \frac{\sin\theta_\tau \sin(\phi_\tau - \phi_\nu)}{\cos\theta_\nu \sin\theta_\tau \cos(\phi_\tau - \phi_\nu) - \sin\theta_\nu\cos\theta_\tau} \ . \end{aligned} \tag{8.0.3}$$

The Jacobian factor from $(\cos\theta_\tau,\ \phi_\tau)$ to $(\cos\theta_{\tau\nu},\ \phi_{\tau\nu})$ is given by J which turns out to be equal to one.

$$J = \begin{vmatrix} \dfrac{\partial\cos\theta_{T\nu}}{\partial\cos\theta_T} & \dfrac{\partial\cos\theta_{T\nu}}{\partial\phi_T} \\ \dfrac{\partial\phi_{T\nu}}{\partial\cos\theta_T} & \dfrac{\partial\phi_{T\nu}}{\partial\phi_T} \end{vmatrix} = 1 \ . \tag{8.0.4}$$

This simplifies the transition from the laboratory frame to the $\nu - \tau$ frame for the cross section determination.

The expected number of tau-leptons (N_τ) in the ICAL detector (50 kton) in 5 years exposure are obtained by integrating[1] eq. 8.0.5 below. Initial neutrino energy is chosen from the threshold value ($E_\nu^{\rm thre.}$) up to 100 GeV. The angle $\cos\theta_\nu = -1$ defines up-going

---

[1] kVegas Monte-Carlo multidimensional integrator is used through the ROOT interface.

events through the detector. The 3-D differential atmospheric neutrino flux is taken from [137]. The neutrino oscillations probability determines the fraction of the initial flux that is getting converted to tau neutrino flux. The $\phi_{\tau\nu}$ integration is trivial since the cross section is independent of it. Initial neutrino energy and angle actually defines the minimum value for the $\cos\theta_{\tau\nu}$. It is seen that for the used energy range of the incoming neutrinos and their angles, the minimum value of $\cos\theta_{\tau\nu}$ does not fall below 0.85. To speed up the computation, this minimum value is thus kept fixed. The expression for the events N_τ in five years is

$$\begin{aligned} N_\tau &= N_T \times T \times \int_{E_\nu^{\text{thre.}}}^{\text{max}} dE_\nu \int_{\cos\theta_\nu=-1}^{+1} d\cos\theta_\nu \int_{\phi_\nu=0}^{2\pi} d\phi_\nu \\ &\left(\frac{d^3\Phi_{\nu_\mu}}{dE_{\nu_\mu} d\cos\theta_{\nu_\mu}\, d\phi_{\nu_\mu}} P_{\mu\tau}(E_\nu,\, \cos\theta_\nu) + \frac{d^3\Phi_{\nu_e}}{dE_{\nu_e} d\cos\theta_{\nu_e}\, d\phi_{\nu_e}} P_{e\tau}(E_\nu,\, \cos\theta_\nu) \right) \\ &\times \int_{E_\tau^{min}}^{E_\tau^{max}} dE_\tau \int_{\cos\theta_{\tau\nu}=0.85}^{1} d\cos\theta_{\tau\nu} \int_{\phi_{\tau\nu}=0}^{2\pi} d\phi_{\tau\nu}\, \frac{d\sigma_{\nu T}}{dE_\tau\, d\cos\theta_{\tau\nu}\, d\phi_{\tau\nu}}\,, \end{aligned} \tag{8.0.5}$$

where $d\Phi/dEd\cos\theta d\phi$ is the differential neutrino flux (in $m^{-2}s^{-1}sr^{-1}$GeV^{-1}), $P_{\alpha\tau}$ is the oscillation probability from flavour $\alpha\,(e,\mu)$ to τ, N_T is the total number of target nuclei and T is the exposure time (5 years)[1].

Table 8.1. The constant parameters used to determine the N_τ.

Material details	Dimensions (m^3)	Density (kton-m^{-3})	No. of layers	No. of modules
Iron slab	16×16×0.056	7.87×10^{-3}	151	3
Glass plate	16×16×0.003	2.65×10^{-3}	150	3
Detector mass of the 3 modules (M) (kton)			~52.94	
Avogadro's No. (N_A) (kton)			6.022142×10^{32}	
Total no. of target nuclei (N_T)			$M \times N_A$	
Exposure time (T) (s)			$\sim 5 \times (3.16 \times 10^7)$	

Numerical details : The flow of integration algorithm is shown in Figure 8.2. Range for various parameters are set in the *Main function*. *Multi-dimensional integrator function* generates random numbers for each set of parameters throughout the available

---

[1] Cross section is in m^2; 1 GeV^{-1} = 0.197 fm = 197×10^{-18} m

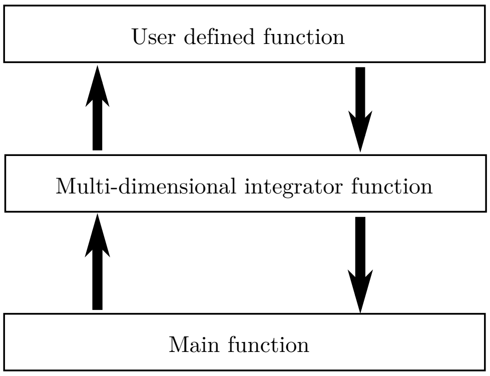

Figure 8.2. Flow chart for the integration.

phase space. Using these random numbers, *User defined function* calculates the integrand value and returns which ultimately come along to the *Main function*. First (Method I), random numbers were directly generated within the specified range inside the *Multi-dimensional integrator function*. But in this way overall convergence of the integration is very much slow and poor as seen in Table 8.2. Therefore, in the second method (Method II) range for all the parameters are once set in the *Main function* and they are also accessible by the *User defined function*. The *Multi-dimensional integrator function* then generates random numbers for each parameter within 0 – 1. Using these random numbers, inside the *User defined function* each parameter are then scaled within their specified range to calculate the integrand. This second method converges well as shown in Table 8.2.

Table 8.2. Convergence in the total number of tau events.

Method	No. of trials	N_{τ^-}	N_{τ^+}
I	10^5	96.5 ± 49.9	21.2 ± 12.9
	10^6	84.9 ± 31.6	19.9 ± 11.8
	10^7	74.8 ± 21.3	22.3 ± 7.8
II	10^5	116.8 ± 4.0	45.1 ± 1.4
	10^6	117.1 ± 1.7	45.0 ± 0.7
	10^7	117.3 ± 0.8	45.1 ± 0.3
	10^8	117.3 ± 0.5	45.1 ± 0.2

The calculation gives a total of 117 τ^- and 45 τ^+ events upward-going directions $(-1 \leqslant \cos\theta \leqslant 0)$, whereas in the downward-going directions chance of getting tau-lepton events is very much negligible as oscillation effect is almost absent. The distribution of tau-lepton events, as obtained in the ICAL detector (3 modules), is given in Table 8.3.

Table 8.3. Variation of N_τ with incident neutrino angle.

θ_ν	N_{τ^-}	N_{τ^+}	$\cos\theta_\nu$	N_{τ^-}	N_{τ^+}
$0^\circ - 90^\circ$	~0	~0	$1.0 - 0.0$	~0	~0
$90^\circ - 105^\circ$	19	8	$0.0 - -0.25$	18	8
$105^\circ - 130^\circ$	53	21	$-0.25 - -0.5$	34	14
$130^\circ - 155^\circ$	34	12	$-0.5 - -0.75$	34	12
$155^\circ - 180^\circ$	11	4	$-0.75 - -1.0$	31	11

8.1 Tau decay

Direct detection of tau-leptons in the ICAL detector is not possible due to thick iron absorbers. Lifetime of tau-leptons is about 0.3 ps in its rest frame and hence, it decays very fast to other lighter leptons (e or μ) or hadrons after it is produced. Many dedicated experiments, like OPERA experiment [152] which will look for tau appearance from tau neutrino, are planned. Tau leptons decay through leptonic process 17% of the time, separately for electrons and muons, whereas, branching fraction for hadronic decay is 66%. There are many decay modes of tau to hadrons associated with neutrino as given in ref. [164].

In the leptonic decay mode, tau decays as

$$\tau^-(k') \rightarrow l^-(q_1)\,\bar{\nu}_l(q_2)\,\nu_\tau(q_2) \tag{8.1.1}$$

where, ($l \equiv e$ or μ) and E_l is the energy of the lepton. E_l can be measured but neutrinos will not be detected. The four-momentum of all the particles are mentioned within the parentheses in eq. 8.1.1 and same for the lepton in the laboratory frame is

$$q_1 = (E_l,\, p_l \sin\theta_l \cos\phi_l,\, p_l \sin\theta_l \sin\phi_l,\, p_l \cos\theta_l)\,. \tag{8.1.2}$$

The general decay width for this decay (initial tau leptons are unpolarised) in the laboratory frame of the original neutrino-nucleon interactions [162] is given by,

$$\frac{d\,\Gamma(E_\tau,\, E_l,\, \theta_\tau,\, \theta_l,\, \phi_l)}{dE_l\, d\cos\theta_l\, d\phi_l} = \frac{G_F^2\, p_l}{48\pi^4\, E_\tau}\left[3(m_\tau^2+m_l^2)(k'\cdot q_1)-4(k'\cdot q_1)^2-2(m_\tau+m_l)^2\right]. \quad (8.1.3)$$

Compared to Figure 8.1, this decay need not be confined in the same plane with respect to the original initial neutrino and tau lepton plane and may happen in any other planes. Therefore, the kinematic condition, $(k'-q_1)^2 > 0$, imposes a constraint on the azimuthal angle ϕ_l as:

$$\cos\phi_l > \frac{2\Big(E_l\, E_\tau - p_l\, p_\tau \cos\theta_\tau \cos\theta_l\Big) - \Big(m_\tau^2 + m_l^2\Big)}{2p_l\, p_\tau\ \sin\theta_\tau\ \sin\theta_l}\,. \quad (8.1.4)$$

The typical decay rate for a tau with energy $E_\tau = 10$ GeV is shown as function of the lepton energy in Figure 8.3 [163]. It can be noticed that the lepton is emitted mostly in the direction of the tau (which was itself forwardly peaked) while its energy is typically highly degraded compared to its parent. Hence, leptons produced in ν_τ interactions mostly contribute to the forward event rate at low energy. The branching fraction of this leptonic decay is 17% and the total number of tau events are expected to be at the order of hundred (Table 8.3); therefore, the number of muons produced from tau decay is also very few and they are also expected to be peaked at the lower energy with

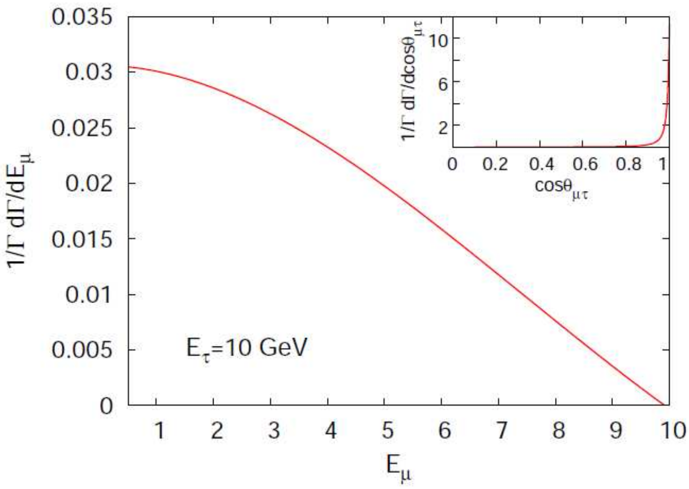

Figure 8.3. Tau decay rate as a function of the final muon energy E_μ and direction (inset) for tau with energy $E_\tau = 10$ GeV. Here $\theta_{\mu\tau}$ is the opening angle between the muon and its parent tau.

respect to the parent tau energy. So, these muons cannot be identified separately from direct muons coming from ν_μ interactions with the iron target of the ICAL detector. Electrons coming out of the tau decay are expected to produce shower like events in the ICAL detector which also cannot be distinguished (at this stage) from normal shower produced due to hadrons. In general, these leptons coming out from tau decay cannot be identified as a signature of tau decay in the ICAL detector but their contribution as a background has to be accounted for the oscillation analysis. This is beyond the scope of the present study. Instead, we focus on indirect tau observation through modification of the neutral current NC rate through its decay into hadrons.

The NC interaction rate is independent of oscillations (as long as there are no sterile neutrino flavours). Hence we have used the NUANCE neutrino generator package in order to generate these events.

The threshold energy of the incoming neutrino for the tau production is itself high (~3.5 GeV) and, so these hadrons coming from taus are also considered as hard (i.e., energy of these hadrons do not degrade compared to its parent) hadrons. Due to many decay modes of tau to hadrons $d\Gamma_{\tau\to\sum h}/dE_h$ for these decays is not trivial to calculate from the kinematics. A specially developed package for tau decay, called TAUOLA [165], is available; TAUOLA package through NUANCE interface is used to get branching ratio for tau decay to hadrons.

All categories of decay modes are obtained when tau decays but we choose only those decays where at the final state no lepton (i.e., $e\,\text{or}\,\mu$) is present. Doing so, we reject leptonic decay modes of tau and accept only the hadronic decay channels.

In these decays ($\tau \to \nu_\tau \sum h$), hadrons carry major fraction of tau energy compared to the final ν_τ. An example plot is shown in Figure 8.4, where initially 16 GeV ν_τ was chosen which gives τ and then their decay to hadrons are selected to plot tau energy (E_τ), final ν_τ energy and net energy of hadrons. The net energy of hadrons (E_h) is defined as the difference between the initial tau energy and the outgoing neutrino energy ($E_h = E_\tau - E_{\nu_\tau}$). Figure 8.4 clearly shows mean energy of hadrons are almost half of the initial tau energy.

As direct tau is not available to start with in TAUOLA, different set of energies for initial ν_τ ($E_{\nu_\tau}\,(\text{GeV}) > \text{E}_\tau^{\text{required}}\,(\text{GeV}) + 1\ \text{GeV}$) are chosen with a large sample ($\sim 10^4$). Tau events are selected near the peak energy, having peak value at 4, 5, 6, 7, 8, 9 and

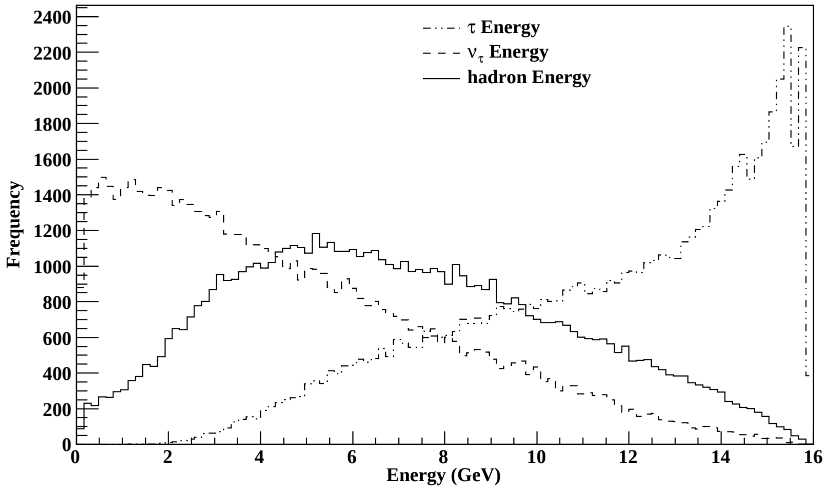

Figure 8.4. $\tau \to \nu_\tau h$: Energy of τ, ν_τ and net hadrons. Now, this τ is coming from ν_τ, where ν_τ energy is fixed in TAUOLA.

10 GeV. By 4 GeV it is meant that E_τ of that sample is within 3.5 – 4.5 GeV and similarly for others. Scaling behaviour of E_h/E_τ implies that the distribution is independent of E_τ within statistical fluctuations as shown in Figure 8.5. A polynomial fitting of order 3

$$y = p_0 + p_1 \times x + p_2 \times x^2 + p_3 \times x^3, \tag{8.1.5}$$

is done to the E_h/E_τ distribution in Figure 8.5b where $x = E_h/E_\tau$ and the results of the fitting are listed in eq. 8.1.6. This is used to generate the final energy of hadrons produced in tau decay.

$$\begin{aligned} p_0 &= 0.0 \text{ (fixed)} \\ p_1 &= 0.0558 \pm 0.0014 \\ p_2 &= -0.0009 \pm 0.0049 \\ p_3 &= -0.0317 \pm 0.0040 \\ \chi^2/ndf &= 177.64/30 \end{aligned} \tag{8.1.6}$$

Note that there are two sets of hadrons in the final state of these interactions. Hadrons are produced in the primary tau neutrino CC interactions along with the charged taus. Additional hadrons are produced during tau decay. Since the tau lifetime is very short, these interactions are simply characterised by hadrons in the final state, and the energy measured is the total of the energy of the two sets of hadrons. They will therefore appear to mimic energetic neutral current events. This is discussed in the next chapter (Chapter 9.

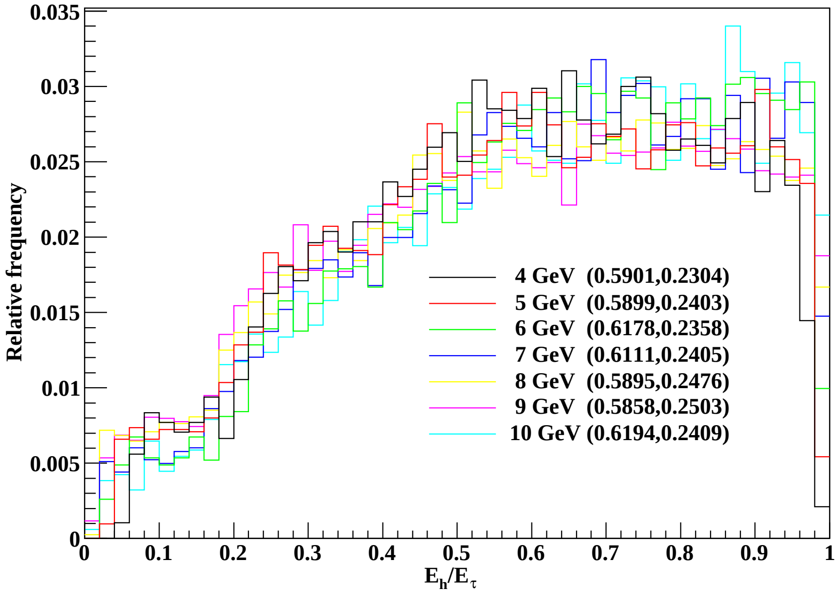

(a) All spectra

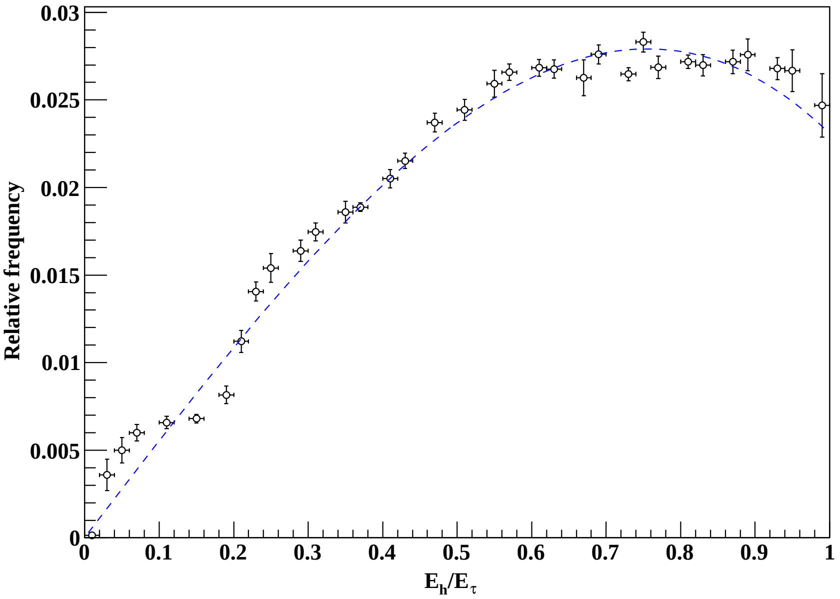

(b) Profile spectrum

Figure 8.5. 8.5a shows overlay plot for all the sets where Mean and RMS for each histogram are given in the legend. 8.5b shows profile histogram for all these sets with a polynomial fit of degree 3.

8.2 Chapter summary

In this Chapter we calculate the total number of tau events as estimated in the ICAL detector considering three modules and 5 years exposure time. Relevant kinematics and brief explanation about the procedure of the multidimensional Monte-Carlo integrator is also presented. Leptonic decay of tau leptons is discussed here. Hadronic mode of decay of tau leptons through the use of TAUOLA event generator is used here and results show that ratio of the net hadron energy to the initial tau lepton energy is independent of the initial tau lepton energy within the statistical fluctuations. While the semi-leptonic decay modes are unlikely to be measured they will add as a small background to CC μ events. The hadronic decay of tau are large and measurable and are characterised by large hadronic energy in the final state. Hence they appear similar to energetic NC events.

9

Tau event generation through Monte-Carlo method

A Monte-Carlo based event generator is used to generate the kinematics of each of the tau events. This kinematics reflects the $(E_\nu,\ \cos\theta,\ \phi)$ dependence of the neutrino fluxes and the $(E_\nu,\ E_\tau,\ \cos\theta_\tau,\ \phi_\tau)$ dependence of the neutrino cross sections. The code is very fast compared to the NUANCE generator [166] since only the kinematics of the leptons is generated, not that of the hadrons.

9.1 Normalisation due to cross-sections

Our code so far does not include the NC cross sections; hence NC events from NUANCE are considered in this study. Apart from QE and DIS, more number of processes are included in the resonance scattering inside NUANCE, whereas only the Δ resonance is considered in the present analysis. This change in the cross-sections will not make much difference as the main contribution arises from DIS events. Still, an overall normalisation is adopted to scale the total number of events. Using same cross-section code, total number of $\mu^\mp$ are estimated (as in the case for taus). Afterwards, CC events due to ν_μ (and anti-particle) interaction with the iron target which gives μ^- (and anti-particle) are looked for. With respect to these total number of muons, an overall normalisation is obtained as NUANCE/ present code of about 1.16. So, total number of hadron events from the NC event sample from NUANCE are then scaled while comparing with the hadron events arising from tau interactions in our calculation.

9.2 Description of the Monte-Carlo event generator

The basic algorithm used here is to generate distributions at each stage of eq. 8.0.5 which are converted into probability distributions and then inverse function methodology is used through random number to extract the information. The sequence of the algorithm is listed below:

- Generate neutrino flux table,
- Generate neutrino-nucleon cross section table,
- Generate flux times cross section table,
- Generate tau kinematics,
- Generate tau decays to hadrons.

9.2.1 Neutrino flux table

Neutrino flux is available from 0.1 GeV to 10 TeV, whereas here we consider only from 3.1623 GeV (as given in Honda flux table) to 100 GeV in this analysis. The bin width of energy in this flux table is ~ 0.115205 GeV if it is considered as $(lnE_2 - lnE_1)$. First, relevant flux values for the specified energy range is saved as,

$$\frac{d\Phi}{(dE_\nu)_i\,(d\cos\theta_\nu)_j\,(d\phi_\nu)_k}\,, \tag{9.2.1}$$

$$\frac{d\Phi}{(dE_\nu)_i\,(d\cos\theta_\nu)_j} = \sum_k \frac{d\Phi}{(dE_\nu)_i\,(d\cos\theta_\nu)_j\,(d\phi_\nu)_k}\,(d\phi_\nu)_k\,, \tag{9.2.2}$$

$$\frac{d\Phi}{(dE_\nu)_i} = \sum_j \frac{d\Phi}{(dE_\nu)_i\,(d\cos\theta_\nu)_j}, \tag{9.2.3}$$

where i, j, k are respectively the index for energy, zenith angle and azimuthal angle of the incoming neutrino. The distribution for $\frac{d\Phi}{(dE_\nu)_i}$ is shown in Figure 9.1a (blue line). This distribution is then converted to a probability distribution (Figure 9.1b). Random numbers are generated following this probability distribution to generate the spectrum of the neutrino flux which is overlaid with the initial distribution and scaled due to the total number of entries as shown in Figure 9.1a (red line). The initial flux distribution and the distribution obtained from the random number generation matches well with each other.

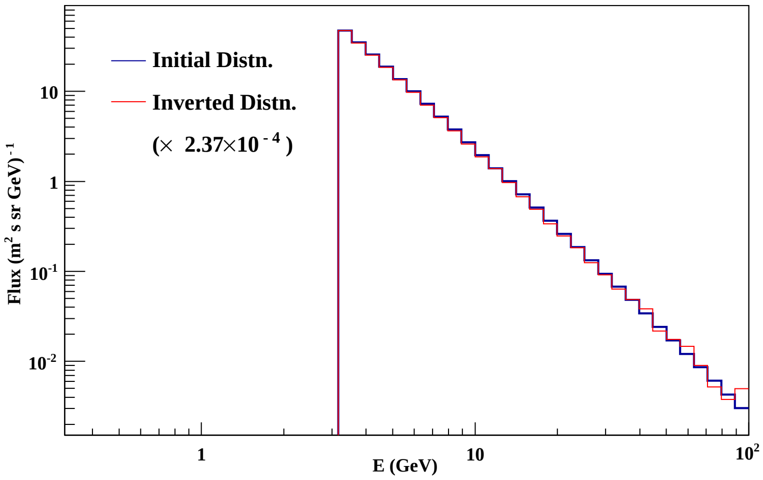

(a)

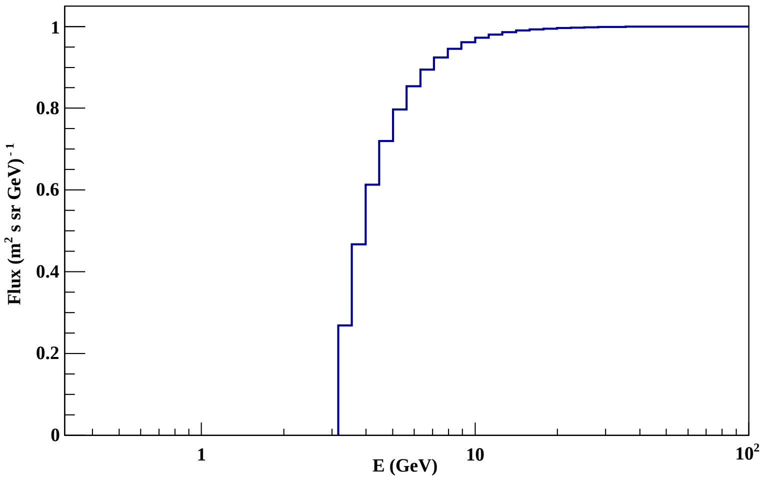

(b)

Figure 9.1. 9.1a shows initial distribution in blue line for the $\frac{d\Phi}{(dE_\nu)_i}$. 9.1b is its probability distribution. The red line in 9.1a shows the inverted distribution which is scaled by a factor of 2.37×10^{-4} for overlay plotting.

9.2.2 Neutrino-nucleon cross section table

Neutrino-nucleon cross sections as obtained from eq. 7.0.10 is saved in similar way like flux table in the following format.

$$\frac{d\sigma}{(dE_\nu)_i\,(d\cos\theta_{\tau\nu})_l\,(dE_\tau)_m}, \tag{9.2.4}$$

$$\frac{d\sigma}{(dE_\nu)_i\,(d\cos\theta_{\tau\nu})_l} = \sum_m \frac{d\sigma}{(dE_\nu)_i\,(d\cos\theta_{\tau\nu})_l\,(dE_\tau)_m}(dE_\tau)_m\,, \tag{9.2.5}$$

$$\frac{d\sigma}{(dE_\nu)_i} = \sum_l \frac{d\sigma}{(dE_\nu)_i\,(d\cos\theta_{\tau\nu})_l} \tag{9.2.6}$$

9.2.3 Flux times cross section table

First, $\frac{d\Phi}{(dE_\nu)_i\,(d\cos\theta_\nu)_j}$ is multiplied with the neutrino oscillations probability to get tau neutrino flux;

$$\frac{d\Phi'}{(dE_\nu)_i\,(d\cos\theta_\nu)_j} = \frac{d\Phi}{(dE_\nu)_i\,(d\cos\theta_\nu)_j} \times P_{l\tau}\Big((E_\nu)_i\,(\cos\theta_\nu)_j\Big), \quad [l:e,\,\mu]. \tag{9.2.7}$$

This modified flux table is then averaged over $\cos\theta_\nu$ and then multiplied with the cross section table as given below:

$$\frac{d\Phi'}{(dE_\nu)_i} = \sum_j \frac{d\Phi'}{(dE_\nu)_i\,(d\cos\theta_\nu)_j}, \tag{9.2.8}$$

$$\frac{d(\Phi'\sigma)}{(dE_\nu)_i} = \frac{d\Phi'}{(dE_\nu)_i} \times \frac{d\sigma}{(dE_\nu)_i} \tag{9.2.9}$$

Total number of tau leptons are then simply obtained as,

$$N_{\tau^-} = N_T \times T \times \sum_i \left(\frac{d(\Phi'\sigma)}{(dE_{\nu_\mu})_i} + \frac{d(\Phi'\sigma)}{(dE_{\nu_e})_i} \right), \tag{9.2.10}$$

$$N_{\tau^+} = N_T \times T \times \sum_i \left(\frac{d(\Phi'\sigma)}{(dE_{\bar\nu_\mu})_i} + \frac{d(\Phi'\sigma)}{(dE_{\bar\nu_e})_i} \right). \tag{9.2.11}$$

9.2.4 Generation of tau kinematics

Each of the distributions mentioned above are converted into probability distributions. Initial neutrino energy depends on $\frac{d(\Phi'\sigma)}{(dE_\nu)_i}$ distribution and E_ν is generated following the shape of this distribution using random number.

A ν_τ event is first generated with energy, E_{ν_τ}, from the $\frac{d(\Phi'\sigma)}{(dE_{\nu_\mu})_i}$ distribution. The $\cos\theta_{\nu_\tau}$ is generated using the $\frac{d\Phi}{(dE_{\nu_\mu})_i\,(d\cos\theta_{\nu_\mu})_j}$ distribution for the corresponding E_{ν_τ}. Having E_{ν_τ} and $\cos\theta_{\nu_\tau}$, the azimuthal angle, ϕ_{ν_τ}, is generated from the distribution of $\frac{d\Phi}{(dE_{\nu_\mu})_i\,(d\cos\theta_{\nu_\mu})_j\,(d\phi_{\nu_\mu})_k}$. In a similar way, electron neutrino flux is used to generate ν_τ events where energy, zenith angle and azimuthal angle of the tau leptons are labelled as E'_{ν_τ}, $\cos\theta'_{\nu_\tau}$, ϕ'_{ν_τ} respectively.

Now, tau leptons kinematics are generated using ν_τ's energy and angle information separately for muon-neutrino flux and electron-neutrino flux. Using E_{ν_τ} and $\frac{d\sigma}{(dE_{\nu_\tau})_i\,(d\cos\theta_{\tau\nu})_l}$, $\cos\theta_{\tau\nu}$ is generated. The $\phi_{\tau\nu}$ is generated uniformly between $0-2\pi$. Then tau lepton energy, E_τ is generated for the E_{ν_τ} and $\cos\theta_{\tau\nu}$, using the distribution

$\frac{d\sigma}{(dE_\nu)_i\,(d\cos\theta_{\tau\nu})_l\,(dE_\tau)_m}$. Difference between E_{ν_τ} and E_τ, E_{h1}, is defined as the hadron energy in this process.

Lepton angles in the laboratory frame are generated as,

$$\cos\theta_\tau = \cos\theta_{\nu_\tau}\cos\theta_{\tau\nu} - \sin\theta_{\nu_\tau}\sin\theta_{\tau\nu}\cos\phi_{\tau\nu}\,, \tag{9.2.12}$$

$$\begin{aligned}
\sin(\phi_\tau - \phi_\nu) &= \frac{\sin\theta_{\tau\nu}\sin\phi_{\tau\nu}}{\sin\theta_\tau}\,,\\
\cos(\phi_\tau - \phi_\nu) &= \frac{\cos\theta_{\tau\nu} - \cos\theta_\nu\cos\theta_\tau}{\sin\theta_\tau\sin\theta_\nu}\,,\\
\phi_\tau &= \phi_\nu + \tan^{-1}(\phi_\tau - \phi_\nu)\,.
\end{aligned} \tag{9.2.13}$$

In this $\nu_\tau + N \rightarrow \tau^- + X$ process, angle between input neutrino and net hadrons and, also between the input neutrino and outgoing lepton is given by following equations.

$$\begin{aligned}
p_{\nu_\tau x} &= E_{\nu_\tau}\sin\theta_{\nu_\tau}\cos\phi_{\nu_\tau}\,,\\
p_{\nu_\tau y} &= E_{\nu_\tau}\sin\theta_{\nu_\tau}\sin\phi_{\nu_\tau}\,,\\
p_{\nu_\tau z} &= E_{\nu_\tau}\cos\theta_{\nu_\tau}\,.
\end{aligned} \tag{9.2.14}$$

$$\begin{aligned}
p_\tau &= \sqrt{E_\tau^2 - m_\tau^2}\,,\\
p_{\tau x} &= p_\tau\sin\theta_\tau\cos\phi_\tau\,,\\
p_{\tau y} &= p_\tau\sin\theta_\tau\sin\phi_\tau\,,\\
p_{\tau z} &= p_\tau\cos\theta_\tau\,.
\end{aligned} \tag{9.2.15}$$

$$p_h = \sqrt{(p_{\nu_\tau x} - p_{\tau x})^2 + (p_{\nu_\tau y} - p_{\tau y})^2 + (p_{\nu_\tau z} - p_{\tau z})^2} \tag{9.2.16}$$

Angle between input neutrino and the net hadrons ($\theta_{h\nu_\tau}$) is given by,

$$\begin{aligned}
\cos\theta_{h\nu_\tau} &= \frac{p_{\nu_\tau}^2 - p_{\nu_\tau}\cdot p_\tau}{p_{\nu_\tau}\cdot p_h}\,,\\
\cos\theta_{h\nu_\tau} &= \frac{E_{\nu_\tau}^2 - p_{\nu_\tau}\cdot p_\tau}{E_{\nu_\tau}|p_h|}\,.
\end{aligned} \tag{9.2.17}$$

The $\theta_{h\nu_\tau}$ distribution is shown in Figure 9.2a. In case of tau decays, $\tau^- \rightarrow \nu_\tau \sum h$, it is easier to estimate angle between the tau lepton momentum vector and the net hadron momentum vector ($\theta_{h\tau}$) from TAUOLA outputs as 3-momenta of incoming and outgoing particles are given.

$$\begin{aligned} \vec{p_\tau} &= \vec{p}_{\nu_\tau} + \vec{p}_h \, , \\ \vec{p_\tau} \cdot \vec{p}_h &= |\vec{p_\tau}|^2 - \vec{p}_{\nu_\tau} \cdot \vec{p_\tau} \, , \\ \cos\theta_{h\nu_\tau} &= \frac{|\vec{p_\tau}|^2 - \vec{p}_{\nu_\tau} \cdot \vec{p_\tau}}{|\vec{p_\tau}||p_h|} \, . \end{aligned} \tag{9.2.18}$$

The $\theta_{h\tau}$ distribution is shown in Figure 9.2b. It is visible from these figures that produced hadrons in both the cases are quite forward peaked with respect to the initial tau neutrinos.

Hadrons coming from tau decay are estimated using eq. 8.1.5, eq. 8.1.6 and the Figure 8.5b. Hadron energy obtained from this process is labelled as E_{h2}. The total energy is the sum of E_{h1} and E_{h2}.

Initially, τ^- events are generated when muon-neutrino and electron-neutrino fluxes are used. Later on τ^+ events are generated taking anti-neutrino fluxes.

9.3 Comparison of hadron events: tau induced hadrons and NC background

In this study, events are very much in the forward directions with respect to the initial neutrino direction; in other words, the up-going tau neutrinos give rise to visible signals in the detector that also correspond to “up-going” events. In the case of NC events, the up-going and down-coming samples are separated. In each case, an angle cut near horizontal direction (5° in either direction from horizon) is applied to filter out those events which may be identified with wrong direction due to large angle scattering. Tau induced hadrons events, as obtained, are plotted with hadron events from NC event sample in the same hadron energy bin in Figure 9.3.

The significance of the tau contribution can be determined through a χ^2 analysis. When the “data” consisting of NC (up and down) and tau induced signal together are fitted to NC alone, the $\Delta\chi^2$ obtained is 59.6 so the indirect observation of tau through

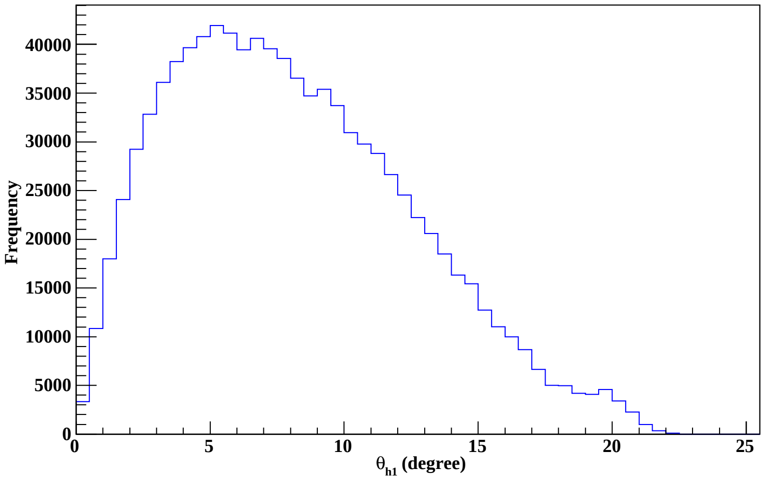

(a)

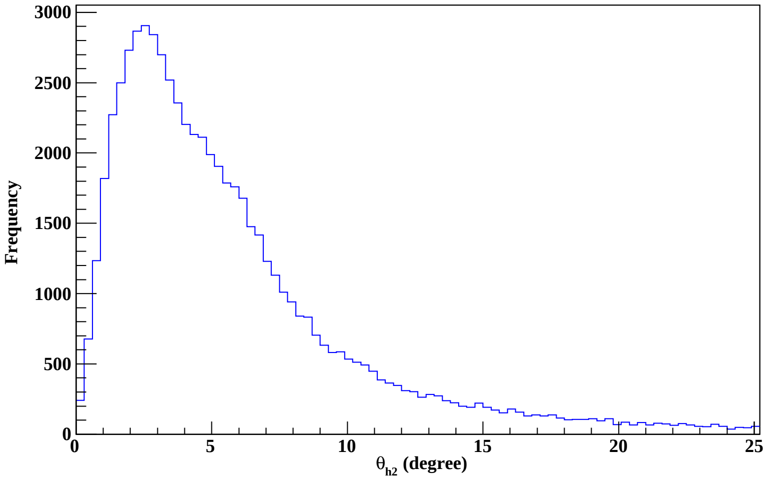

(b)

Figure 9.2. 9.2a shows angle between 3-momenta of incident neutrino and outgoing hadrons for the $\nu_\tau + N \to \tau^- + X$ process. 9.2b shows angle between 3-momenta of incident tau and outgoing net hadrons for the $\tau^- \to \nu_\tau \sum h$ process. Incident neutrinos are taken from $E_{\rm th}$ to 100 GeV in both the cases.

this channel is at more than 7σ confidence level. Hence our simulations indicate that there is an excellent possibility to detect τ events from oscillations of atmospheric neutrinos in the ICAL detector by studying the modifications of the NC signals. A more detailed analysis is required in order to obtain constraints on the neutrino oscillation parameters themselves from this channel. This is a future possible direction of study.

9.4 Chapter summary

A Monte-Carlo based event generator is developed and discussed in this chapter, considering only charged current interactions for neutrinos with the target nucleon. The

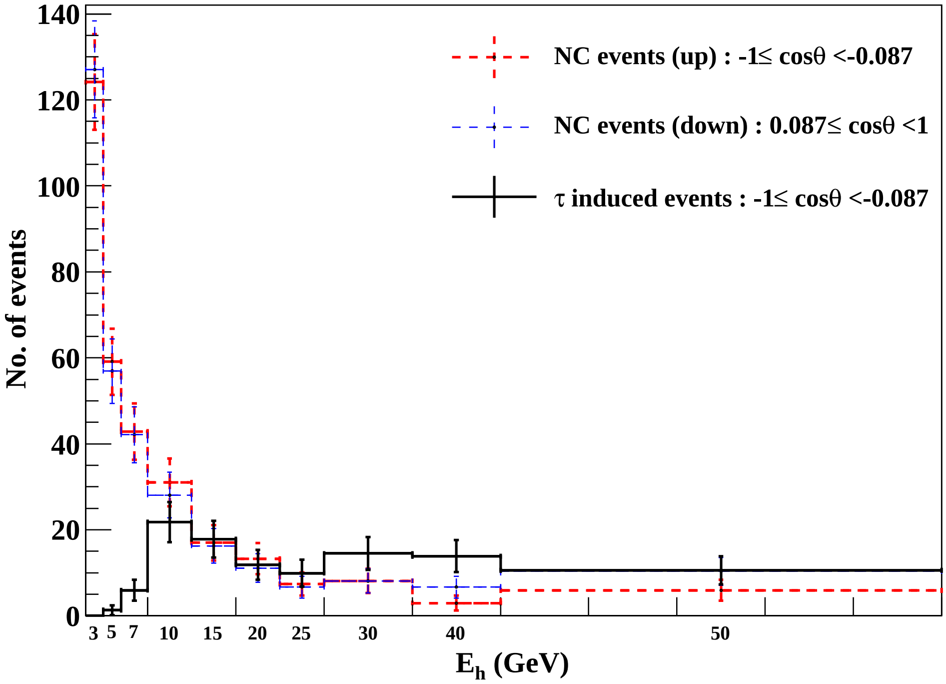

Figure 9.3. Number of hadron events due to NC sample and from tau induced hadrons. Here, 3 GeV bin corresponds to 3 – 5 GeV and so on, whereas the last bin corresponds to 50 – 100 GeV.

algorithm is discussed in detail in this chapter. Neutral current interactions is taken from NUANCE, as the current work is beyond that scope. Final energy distributions of hadrons coming from nu-tau signal is compared with NUANCE neutral current data and it is at more than 7σ confidence level. Hence the NC channel measurement will give excellent information on tau neutrinos arising from oscillations.

Part III

Summary and future outlook

10 Summary and future outlook

Analysis of cosmic ray muon data from the RPC prototype detector stack provides understanding of detector tracking efficiencies and position resolutions. This study is now carried out regularly to monitor the detector performance towards better understanding of muon flux monitoring over long period. It is proposed to stagger the RPCs in the prototype stack to confirm that the observed RPC inefficiencies are not due to solid angular acceptance issues. Simulation studies of the gas flow inside the RPCs are underway to confirm that the gas flow is uniform over the entire active volume of the RPC. Results of these studies will also be fed back into the Monte Carlo code and will be fine tuned.

Time resolution of the RPCs are studied in this analysis. The observed value is well within the requirements of the ICAL detector. Measurement of time delays of the RPC signal paths has been done and the method established can be used for the main ICAL detector as well. The background muon rates in the underground are very low compared to those at the surface. The planned readout electronics for ICAL detector is different from that being used with the RPC prototype detector stack and in principle, time calibration can be performed at the surface for each RPC detector of the ICAL. Directionality study of cosmic ray muons will be useful in the main ICAL detector to monitor the underground muon background. This is because muons are expected to reach the detector from other side of the earth, as high energy muons can penetrate only few km of rock overburden to reach the detector. A negligible fraction of muons may be observed in the upward going direction which are mainly produced by some neutrino induced processes.

Simulations study of tau events in the ICAL detector provides promising results indicating that indirect observation of tau events through its hadronic decay channel is possible at more than 7σ significance over the neutral current background. In fact, proper inclusion of the tau-induced hadron events is very important for studying other exotic possibilities such as the presence of sterile neutrinos, which also affects the NC signal. The question of whether this channel is sufficiently sensitive to help determine the oscillation parameters themselves through the tau contribution is still an open one and is currently being pursued. In fact, many more extensions and refinements of this study are possible and will be part of future work in this direction.

Bibliography

[1] Letter to the participants of workshop at Tübingen, Germany, (1930).

[2] W. Pauli, *Cambridge Monogr. Part. Phys. Nucl. Phys. Cosmol.*, **14**, 1–22, 2000.

[3] J. Chadwick, *Nature*, **129**, 312, 1932.

[4] E. Fermi, *Z. Phys.*, **88**, 161–177, 1934.

[5] E. Fermi, *Nuovo Cimento*, **11**, 1–19, 1934.

[6] G. Gamow and E. Teller, *Phys. Rev.*, **49**, 895–899, 1936.

[7] J. C. Street and E. C. Stevenson, *Phys. Rev.*, **52**, 1003–1004, 1937.

[8] S. H. Neddermeyer and C. D. Anderson, *Phys. Rev.*, **51**, 884–886, 1937.

[9] B. Pontecorvo, *Phys. Rev.*, **72**, 246, 1947.

[10] H. A. Bethe and R. E. Peierls, *Nature*, **133**, 532, (1934).

[11] Frederick Reines and Clyde L. Cowan, Jr., *Nature*, **178**, 446, (1956).

[12] F. Reines, *Rev. Mod. Phys.*, **68**, 317–327, 1996.

[13] F. Reines, C. L. Cowan, F. B. Harrison, A. D. McGuire and H. W. Kruse, *Phys. Rev.*, **117**, 159–173, 1960.

[14] T. D. Lee and C. N. Yang, *Phys. Rev.*, **104**, 254–258, 1956.

[15] C. S. Wu, E. Ambler, R. W. Hayward, D. D. Hoppes and R. P. Hudson, *Phys. Rev.*, **105**, 1413–1414, 1957.

[16] R. P.Feynman and M. Gell-Mann, *Phys. Rev.*, **109**, 193–198, 1958.

[17] E. C. Sudarshan and R. E. Marshak, *Phys. Rev.*, **109**, 1860–1862, 1958.

[18] J. J.Sakurai, *Nuovo Cimento*, **7**, 649, 1958.

[19] L. Landau, *Nucl. Phys.*, **3**, 127, 1957.

[20] T. D. Lee and C. N. Yang, *Phys. Rev.*, **105**, 1671, 1957.

[21] A. Salam, *Nuovo Cimento*, **5**, 299, 1957.

[22] M. Goldhaber, L. Grodzins and A. W. Sunyar, *Phys. Rev.*, **109**, 1015–1017, 1958.

[23] E. J. Konopinski and H. M. Mahmoud, *Phys. Rev.* **92**, 1045 (1953).

[24] B. Pontecorvo, *Sov. Phys. JETP*, **10**, 1236–1240, 1960.

[25] G. Danby et al., *Phys. Rev. Lett.*, **9**, 36–44, 1962.

[26] S. L. Glashow, *Nucl. Phys.*, **22**, 579–588, 1961.

[27] A. Salam, 1969, *Proc. of the 8^{th} Nobel Symposium on 'Elementary Particle Theory, Relativistic Groups and Analyticity', Stockholm, Sweden, 1968, edited by N. Svartholm, p. 367–377.*

[28] S. Weinberg, *Phys. Rev. Lett.*, **19**, 1264–1266, 1967.

[29] P. W. Higgs, *Phys. Lett.* **12**, 132, 1964; *Phys. Rev. Lett.* **13**, 508–509, 1964; *Phys. Rev.* **145**, 1156–1163, 1966.

[30] F. Englert and R. Brout , *Phys. Rev. Lett.* **13**, 321–322, 1964.

[31] G. S. Guralnik, C. R. Hagen and T. W. B. Kibble, *Phys. Rev. Lett.* **13**, 585–587, 1964; T. W. B. Kibble, *Phys. Rev.* **155**, 1554–1561, 1967.

[32] G. 't Hooft, *Nucl. Phys.*, **B35**, 167–188, 1971; *Nucl. Phys.*, **B33**, 173–199, 1971; G. 't Hooft and M. J. G. Veltman, *Nucl. Phys.*, **B44**, 189–213, 1972.

[33] F. J. Hasert et al., *Phys. Lett.* **B46**, 121–124, 1973; *Phys. Lett.* **B46**, 138–140, 1973; *Nucl. Phys.*, **B73**, 1, 1974.

[34] A. C. Benvenuti et al., *Phys. Rev. Lett.* **32**, 800–803, 1974.

[35] J. J. Aubert et al., *Phys. Rev. Lett.* **33**, 1404–1406, 1974.

[36] J. E. Augustin et al., *Phys. Rev. Lett.* **33**, 1406–1408, 1974.

[37] G. Arnison et al., *Phys. Lett.*, **B122**, 103–116, 1983; M. Banner et al., *Phys. Lett.*, **B122**, 476–485, 1983.

[38] G. Arnison et al., *Phys. Lett.*, **B126**, 398–410, 1983; P. Bagnaia et al., *Phys. Lett.*, **B129**, 130–140, 1983.

[39] S. L. Glashow, J. Iliopoulos, and L. Maiani, *Phys. Rev.* **D2**, 1285–1292, 1970.

[40] M. L. Perl et al., *Phys. Rev. Lett.* **35**, 1489–1492, 1975.

[41] Kodama et al., DONuT collaboration, *Phys. Lett.* **B, 504**, 218–224, 2001.

[42] S. W. Herb et al., *Phys. Rev. Lett.* **39**, 252–255, 1977.

[43] F. Abe et al., *Phys. Rev. Lett.* **74**, 2626–2631, 1995; S. Abachi et al., *Phys. Rev. Lett.* **74**, 2632–2637, 1995.

[44] S. Chatrchyan et al., (CMS collaboration), *Phys. Lett.* **B716**, 30–61, 2012.

[45] G. Aad et al., (ATLAS collaboration), *Phys. Lett.* **B716**, 1–29, 2012.

[46] B. Adeva et al., *Phys. Lett.*, **B231**, 509, 1989; D. Decamp et al., *Phys. Lett.*, **B231**, 519, 1989; M. Z. Akrawy et al., *Phys. Lett.*, **B231**, 530, 1989; P. A. Aarnio et al., *Phys. Lett.*, **B231**, 539, 1989.

[47] J. H. Christenson, J. W. Cronin, V. L. Fitch and R. Turlay, *Phys. Rev. Lett.* **13**, 138–140, 1964.

[48] M. Kobayashi and T. Masakawa, *Prog. Theor. Phys.*, **49**, 652–657, 1973.

[49] N. Cabibbo, *Phys. Rev. Lett.* **10**, 531–532, 1963.

[50] B. Pontecorvo, *Sov. Phys. JETP*, **6**, 429, 1957; B. Pontecorvo, *Sov. Phys. JETP*, **7**, 172–173, 1958.

[51] M. Gell-Mann and A. Pais, *Phys. Rev.* **97**, 1387–1389, 1955.

[52] Z. Maki, M. Nakagawa and S. Sakata, Prog. Theor. Phys., 28, 870, 1962.

[53] V. N. Gribov and B. Pontecorvo, *Phys. Lett.*, **B28**, 493, 1969.

[54] S. Eliezer and A. R. Swift, *Nucl. Phys.*, **B105**, 45, 1976.

[55] H. Fritzsch and P. Minkowski, *Phys. Lett.*, **B62**, 72, 1976.

[56] S. M. Bilenky and B. Pontecorvo, *Sov. J. Nucl. Phys.*, **24**, 316–319, 1976; *Nuovo Cim. Lett.*, **17**, 569, 1976.

[57] S. M. Bilenky and B. Pontecorvo, *Phys. Rep.*, **41**, 225, 1978.

[58] http://www.nu.to.infn.it/exp/all/imb/

[59] Y. Fukuda et al., *Phys. Rev. Lett.* **81**, 1562–1567, 1998.

[60] The Super-Kamiokande Collaboration, *Phys. Rev. Lett.* **85** 3999–4003, (2000).

[61] W. W. M. Allison et al., *Phys. Lett.* **B391**, 491–500, 1997.

[62] W. W. M. Allison et al., *Phys. Lett.* **B449**, 137–144, 1999.

[63] W. W. M. Allison et al., *Phys. Rev.* **D72**, 052005, 2005.

[64] M. Sanchez et al., *Phys. Rev.* **D68**, 113004, 2003.

[65] S. P.Ahlen et al., *Phys. Lett.* **B357**, 481–486, 1995.

[66] M. Ambrosio et al., *Phys. Lett.* **B434**, 451–457, 1998.

[67] M. Ambrosio et al., *Phys. Lett.* **B478**, 5–13, 2000.

[68] M. Ambrosio et al., *Phys. Lett.* **B517**, 59–66, 2001.

[69] M. H. Ahn et al., *Phys. Rev. Lett.* **90**, 041801, 2003.

[70] M. H. Ahn et al., *Phys. Rev. Lett.* **93**, 051801, 2004.

[71] S. H. Ahn et al., *Phys. Lett.* **B511**, 178–184, 2001.

[72] E. Aliu et al., *Phys. Rev. Lett.* **94**, 081802, 2005.

[73] B. T. Cleveland, T. Daily, J. Davis, Raymond, J. R. Distel, K. Lande, et al., *Astrophys. J.*, **496**, 505–526, 1998.

[74] Q. R. Ahmad et al., *Phys. Rev. Lett.* **89**, 011301, 2002.

[75] T. Araki et al., *Phys. Rev. Lett.* **94**, 081801, 2005.

[76] K. Eguchi et al., *Phys. Rev. Lett.* **90**, 021802, 2003.

[77] Björn Wonsak for the OPERA Collaboration, *Journal of Physics: Conference Series* **335** (2011) 012051.

[78] K. Abe et al., T2K Collaboration, *arXiv:1106.2822*.

[79] P. Adamson et al., *arXiv:1301.4581*.

[80] DAYA-BAY collaboration, F. An et al., *Phys. Rev. Lett.* **108**, 171803, 2012.

[81] RENO collaboration, J. Ahn et al., *Phys. Rev. Lett.* **108**, 191802, 2012.

[82] DOUBLE-CHOOZ collaboration, Y. Abe et al., *Phys. Rev. Lett.* **108**, 131801, 2012.

[83] T2K collaboration, K. Abe et al., *Phys. Rev. Lett.* **107**, 041801, 2011.

[84] MINOS collaboration, P. Adamson et al., *Phys. Rev. Lett.* **107**, 181802, 2011.

[85] SUPER-KAMIOKANDE collaboration, R. Wendell et al., *Phys. Rev.* **D 81** 092004 (2010).

[86] K2K collaboration, M. Ahn et al., *Phys. Rev.* **D 74**, 072003, 2006.

[87] MINOS collaboration, P. Adamson et al., *Phys. Rev. Lett.* **108**, 191801, 2012.

[88] T2K collaboration, K. Abe et al., *Phys. Rev.* **D 85**, 031103, 2012.

[89] CHOOZ collaboration, m. Apollonio et al., *Phys. Lett.* **B 466**, 415, 1999.

[90] PALO VERDE collaboration, A. Piepke, *Prog. Part. Nucl. Phys.* **48** 113, 2002.

[91] DOUBLE-CHOOZ collaboration, Y. Abe et al., *Phys. Rev.* **D 86**, 052008, 2012.

[92] KamLAND collaboration, A. Gando et al., *Phys. Rev.* **D 83**, 052002, 2011.

[93] F. kaether, W. Hampel, G. Heusser, J. Kiko and T. Kirsten, *Phys. Lett.* **B 685**, 47, 2010.

[94] SAGE collaboration, J. Abdurashitov et al., *Phys. Rev.* **C 80**, 015807, 2009.

[95] SUPER-KAMIOKANDE collaboration, J. Hoska et al., *Phys. Rev.* **D 73**, 112001, 2006.

[96] SNO collaboration, B. Aharmim et al., *Phys. Rev.* **C 75**, 045502, 2007.

[97] SNO collaboration, B. Aharmim et al., *Phys. Rev.* **C 72**, 055502, 2005.

[98] SNO collaboration, B. Aharmim et al., *Phys. Rev. Lett.* **101**, 111301, 2008.

[99] SNO collaboration, B. Aharmim et al., arXiv:1109.0763.

[100] G. Bellini, J. Benziger, D. Bick, S. Bonetti, G. Bonfini, et al., *Phys. Rev. Lett.* **107**, 141302, 2011.

[101] G. Bellini, et al., *Phys. Rev.* **D 82**, 033006, 2010.

[102] P. Huber, *Phys. Rev.* **C 84**, 024617, 2011 [*Erratum ibid.* **C 85**, *029901, 2012.*].

[103] C. V. Achar et al., *Phys. Lett.* **18**, 196, 1965.

[104] F. Reines et al., *Phys. Rev. Lett.* **15**, 429 – 433, 1965.

[105] INO Collaboration, Detailed Project Report **I**, (2007).

[106] H. Murayama and T. Yanagida, *Phys. Lett.* **B520**, 263, (2001).

[107] R. P. Kokoulin and A. A. Petrukhin, *Sov. J. Part. Nucl.* **21**, 332, (1990).

[108] G. Charpak et al., *Nucl. Instrum. Methods* **62**, 217, (1968).

[109] G.L.Bruno, Ph.D. Thesis, (2000-2001).

[110] J. Keuffel, *Phys. Rev.* **73**, 531, (1948).

[111] Christian Lippmann, Ph.D. Thesis, (2003).

[112] V. Parchomchuk et al., *Nucl. Instrum. Methods* **93**, 269, (1971).

[113] Y. Pestov, *Nucl. Instrum. Methods* **196**, 45, (1982).

[114] Y. Pestov, Proc. Intl. Winter Meeting on Nucl. Phys., Bormio, Italy, (1998).

[115] A. Arefiev et al., *Nucl. Instrum. Methods* **A 348**, 318, (1994).

[116] R. Santonico and R. Cardarelli, *Nucl. Instrum. Methods* **187**, 377, (1981).

[117] W.R.Leo, Techniques for Nuclear and Particle Physics Experiments, 2nd Ed., Narosa Publ. House, (1995).

[118] B. Satyanarayana, **Ph.D. Thesis**, *Design and Characterisation Studies of Resistive Plate Chambers*, IIT Bombay, 2009.

[119] INO Collaboration, INO Project Report **INO/2006/01**, (2006) and references therein; V.M.Datar, Proc. Nucl. Phys. Symposium, Vadodara, (2006); India-based Neutrino Observatory (INO) web pages: http://www.ino.tifr.res.in and http://www.imsc.res.in/ ino

[120] INO Collaboration, Detailed Project Report on INO-ICAL Detector Structure **II**, (2008)

[121] Magnet6.0 Code, Infolytica Corporation, USA

[122]

[123] S. Ramo, *PROC. IRE* **27** 584, 1961.

[124] W. Reiegler, *Nucl. Instr. and Meth.*, **A 491**, 258–271, 2002.

[125] *Geant4 Material Database*, tech. rep., 2007.

[126] P. K. F. Grieder, *Cosmic Rays at Earth, Researcher's Reference Manual and Data BookCosmic Rays at Earth, Researcher's Reference Manual and Data Book.* Elsevier, 2001.

[127] W. D. D. O. C. Allkofer, R. D. Andresen, *The muon spectra near the geomagnetic equator*, *Canadian Journal of Physics* **46** (1968), no. 10 S301 – S305.

[128] N. Karmakar, A. Paul, and N. Chaudhuri, *Measurements of absolute intensities of cosmic-ray muons in the vertical and greatly inclined directions at geomagnetic latitudes 16°N*, *Il Nuovo Cimento B (1971-1996)* **17** (1973) 173–186. 10.1007/BF02906438.

[129] M. S. Sinha and N. Basu *Indian Journal of Physics* **33** (1959), no. 0 335.

[130] G. S. Gokhale *Private communication (1953) (after Allkofer et al. 1968)* (1953), no. 0.

[131] S. Fukui, T. Kitamura, and Y. Murata, *On the Range Spectrum of μ-Mesons at Sea-Level at Geomagnetic Latitude 24°N*, *Journal of the Physical Society of Japan* **12** (1957), no. 8 854–863.

[132] B. Rossi, *Interpretation of cosmic-ray phenomena*, *Rev. Mod. Phys.* **20** (Jul, 1948) 537–583.

[133] K. Greisen, *The intensities of the hard and soft components of cosmic rays as functions of altitude and zenith angle*, *Phys. Rev.* **61** (Mar, 1942) 212–221.

[134] K. Greisen, *Intensity of cosmic rays at low altitude and the origin of the soft component*, *Phys. Rev.* **63** (May, 1943) 323–333.

[135] K. Greisen and N. Nereson, *Inefficiency and other sources of error in cosmic-ray measurements with self-quenching counters*, *Phys. Rev.* **62** (Oct, 1942) 316–329.

[136] J. Crookes and B. Rastin, *An investigation of the absolute intensity of muons at sea-level*, *Nuclear Physics B* **39** (1972), no. 0 493 – 508.

[137] http://www.icrr.u-tokyo.ac.jp/ mhonda/

[138] Honda et al., *Improvement of low energy atmospheric neutrino flux calculation using the JAM nuclear interaction model*, *Phys. Rev. D* **vol 83, issue 12** (June, 2011), doi : 10.1103/PhysRevD.83.123001.

[139] Honda et al., *Phys. Rev. D* **75**, 043006 (2007).

[140] Honda et al., *Phys. Rev. D* **70**, 043008 (2004).

[141] K. Niita et al., Radiat. Meas. **41**, 1080 (2006).

[142] S. Roesler, R. Engel and J. Ranft (2000), hep-ph/0012252.

[143] H. Collaboration, Astropart. Phys. **29**, 257 (2008), Astropart. Phys. **30**, 124 (2008).

[144] A. M. Dziewonski and D. L. Anderson, *Phys. Earth Plan. Int.*, **25**, 297 (1981).

[145] D. Indumathi, M. V. N. Murthy, G. Rajasekaran and Nita Sinha, *Phys. Rev. D* **74**, 053004 (2006).

[146] M. C. Gonzalez-Garcia, M. Maltoni, J. Salvado and T. Schwetz, *JHEP 12*, (2012) 123, (arXiv:1209.3023 [hep-ph]).

[147] M. C. Conzalez-Garcia et al., *Phys. Rev. D* **55**, 1297 (1997).

[148] L. Pasquali et al., *Phys. Rev. D* **59**, 093003 (1999).

[149] K. Abe et al., *PRL* **97**, 171801 (2006).

[150] The ICARUS collaboration, arXiv:hep-ex0103008; http://www.aquila.infn.it/icarus.

[151] The MINOS collaboration, http://www-numi.fnal.gov:8875/.

[152] A. Rubbia, *Nucl. Phys. Proc. Suppl.* **91** (2000)223, http://operaweb.web.cern.ch/operaweb/index.shtml.

[153] L J. Hall and H. Murayama, *Phys. Lett. B* **463** (1999)241.

[154] E. A. Paschos and J. Y. Yu, *Phys. Rev. D* **65** (2002) 033002.

[155] S. Kretzer and M. H. Reno, *Phys. Rev. D* **66** (2002) 113007.

[156] K. Hagiwara et al., *Nuclear Physics B* **668** (2003) 364-384. arXiv:hep-ph/0305324, arXiv:hep-ph/0503050, http://ntweb.sc.niigata-u.ac.jp/ yokoya/taupol/index.html.

[157] C. H. Albright and C. Jarlskog, *Nucl. Phys. B* **84** (1975) 467.

[158] C. H. Llewellyn Smith, *Phys. Rep.* **3** (1972) 261.

[159] D. Rein and L. M. Sehgal, *Ann. Phys.* **133** (1981)79.

[160] E. A. Paschos, L. Pasquali and J. y. Yu, *Nucl. Phys.* **B 588** (2000) 263.

[161] https://lhapdf.hepforge.org/ .

[162] QFT book, Pal Lahiri.

[163] D. Indumathi and Nita Sinha, arXiv:0910.2020v2.

[164] Lepton summary table, http://pdg.lbl.gov/

[165] Stanislaw Jadach, Johann H. Kühn and Zbigniew Was, *Computer Physics Communications* **64**, 2, p:275 –299, 1991.

[166] D. Casper, http://arxiv.org/abs/hep-ph/0208030.